# I Rigid Body Penetration into Brittle Materials

# II Phase Change Effect on Shock Wave Propagation

Thesis by

Cangli Liu

In Partial Fulfillment of the Requirements
for the Degree of
Doctor of Philosophy

California Institute of Technology
Pasadena, California

1999
(Submitted May 17, 1999)

# ACKNOWLEDGMENTS

In the past years, I really learned a great deal from all the faculty at the Seismological Laboratory. I am especially grateful to my thesis advisor, Thomas J. Ahrens, for his generous advice and support that he has given to me. I thank my academic advisor Joann Stock for her continuous suggestions and help. I have benefited a lot from the discussions with Guruswaminaidu Ravichandran. I thank Epaprodito Gelle, Michael Long, Carl McCaughey and Sue Yamada for their help in conducting the pretty-heavy duty experiments. I also am thankful for help from Bill Anderson, Guangqing Chen, Kathleen Holland, and Wenbo Yang for their help when they were here. I appreciate the collaboration with Nachhatter S. Brar from the Dayton Research Institute on conducting the experiments on $GeO_2$. I also thank Demirkan Coker for his help with English.

I dedicate my thesis to my parents for their constant support and for their undersanding forgiveness when they needed help from me but I was far away from them. I thank my sisters and brother for their support when I was in the university and for taking care of our parents.

Without the help, support and companionship from my lovely wife Ling, it would have been impossible for me to finish my studies at Caltech. I hope that I will have more time to spend with her after we are back in China. I also thank my bosses in China for their support and suggestions in the past years.

And lastly, I would like to acknowledge the support of the Army Research Office, the Air Force Research Office and NASA.

# Contents

# II Phase Change Effect on Shock Wave Propagation in Vitreous $GeO_2$ 135

# List of Figures

# List of Tables

# Part I

# Rigid Body Penetration into Brittle Materials: Experimental and Theoretical Study

# Abstract

We have developed a technique for measuring the depth time history of rigid body penetration into brittle materials (hard rocks and concretes) under a deceleration of $\sim 10^5$ g. The technique includes bar-coded projectile, sabot-projectile separation, detection and recording systems. Because the technique can give very dense data on penetration depth time history, penetration velocity can be deduced. Error analysis shows that the technique has a small intrinsic error of $\sim$ 3 - 4 % in time during penetration, and 0.3 to 0.7 mm in penetration depth. A series of 4140 steel projectile penetration into G-mixture mortar targets have been conducted using the Caltech 40 mm gas/powder gun in the velocity range of 100 to 500 m/s.

We report, for the first time, the whole depth-time history of rigid body penetration into brittle materials (the G-mixture mortar) under $10^5$ g deceleration. Based on the experimental results, including penetration depth time history, damage of recovered target and projectile materials and theoretical analysis, we find:

1. Target materials are damaged via compacting in the region in front of a projectile and via brittle radial and lateral crack propagation in the region surrounding the penetration path. The results suggest that expected cracks in front of penetrators may be stopped by a comminuted region that is induced by wave propagation. Aggregate erosion on the projectile lateral surface is $< 20$ % of the final penetration depth. This result suggests that the effect of lateral friction on the penetration process can be ignored.

2. Final penetration depth, $P_{max}$, is linearly scaled with initial projectile energy per unit cross-section area, $e_s$, when targets are intact after impact. Based on the experimental data on the mortar targets, the relation is $P_{max}(\text{mm}) = 1.15e_s(\text{J/mm}^2) + 16.39$.

3. Estimation of the energy needed to create an unit penetration volume suggests that the average pressure acting on the target material during penetration is $\sim$ 10 to 20 times higher than the unconfined strength of target materials under quasi-static loading, and 3 to 4 times higher than the possible highest pressure due to friction and material strength and its rate dependence. In addition, the experimental data show that the interaction between cracks and the target free surface significantly affects the penetration process.

4. Based on the fact that the penetration duration, $t_{max}$, increases slowly with $e_s$ and does not depend on projectile radius approximately, the dependence of $t_{max}$ on projectile length is suggested to be described by $t_{max}(\mu\mathrm{s}) = 2.08e_s(\mathrm{J/mm}^2 + 349.0 \times m/(\pi R^2)$, in which $m$ is the projectile mass in grams and $R$ is the projectile radius in mm. The prediction from this relation is in reasonable agreement with the experimental data for different projectile lengths.

5. Deduced penetration velocity time histories suggest that whole penetration history is divided into three stages: (1) An initial stage in which the projectile velocity change is small due to very small contact area between the projectile and target materials; (2) A steady penetration stage in which projectile velocity continues to decrease smoothly; (3) A penetration stop stage in which projectile deceleration jumps up when velocities are close to a critical value of $\sim$ 35 m/s.

6. Deduced averaged deceleration, $\overline{a}$, in the steady penetration stage for projectiles with same dimensions is found to be $\overline{a}(\mathrm{g}) = 192.4v + 1.89 \times 10^4$, where $v$ is initial projectile velocity in m/s. The average pressure acting on target materials during penetration is estimated to be very comparable to shock wave pressure.

7. A similarity of penetration process is found to be described by a relation between normalized penetration depth, $P/P_{max}$, and normalized penetration time, $t/t_{max}$, as $P/P_{max} = f(t/t_{max})$, where $f$ is a function of $t/t_{max}$. After $f(t/t_{max})$ is determined using experimental data for projectiles with 150 mm length, the penetration depth time history for projectiles with 100 mm length predicted by

this relation is in good agreement with experimental data. This similarity also predicts that average deceleration increases with decreasing projectile length, that is verified by the experimental data.

8. Based on the penetration process analysis and the present data, a first principle model for rigid body penetration is suggested. The model incorporates the models for contact area between projectile and target materials, friction coefficient, penetration stop criterion, and normal stress on the projectile surface. The most important assumptions used in the model are: (1) The penetration process can be treated as a series of impact events, therefore, pressure normal to projectile surface is estimated using the Hugoniot relation of target material; (2) The necessary condition for penetration is that the pressure acting on target materials is not lower than the Hugoniot elastic limit; (3) The friction force on projectile lateral surface can be ignored due to cavitation during penetration. All the parameters involved in the model are determined based on independent experimental data. The penetration depth time histories predicted from the model are in good agreement with the experimental data.

9. Based on planar impact and previous quasi-static experimental data, the strain rate dependence of the mortar compressive strength is described by $\sigma_f/\sigma_f^0 = \exp(0.0905(\log(\frac{\dot{\varepsilon}}{\dot{\varepsilon}_0}))^{1.14})$, in the strain rate range of $10^{-7}$/s to $10^3$/s ($\sigma_f^0$ and $\dot{\varepsilon}$ are reference compressive strength and strain rate, respectively). The non-dispersive Hugoniot elastic wave in the G-mixture has an amplitude of $\sim 0.14$ GPa and a velocity of $\sim 4.3$ km/s.

# Chapter 1 Introduction

Penetration is defined as the entry of an object (projectile) into any region of a target (*Backman and Goldsmith* [1978]). Penetration is classified into different regimes based on the following parameters: target dimensions (semi-infinite, thick and thin targets), initial impact velocity (hyper-, high-, ballistic- and low-velocity), and deformation of projectile materials (rigid and plastic) (*Backman and Goldsmith* [1978] and *Zukas and Walters* [1990]). For each regime, the diagnostic measurement method and theory are very different. Although research on penetration dynamics has taken place for more than a century, the penetration process is not understood well since it involves impact-induced shock propagation, crack initiation and propagation and large plastic deformation that are still the subject of much study. Therefore, experimental methods development, and analytic and numerical modeling of the penetration process are still very active topics of research. In this research, I am concerned with the simplest problem in penetration dynamics, i.e., a rigid body penetration into a semi-infinite brittle target. Here, the rigid body penetration is defined as the penetration process in which the penetrator material does not undergo plastic deformation. The semi-infinite target is defined as the target whose dimensions are much larger than the penetration depth (*Backman and Goldsmith* [1978]).

Rigid body penetration has many applications. Besides power station safety and military applications (*Backman and Goldsmith* [1978], *Corbett et al.* [1996], and *Goldsmith* [1999]), the use of rigid penetrators in space exploration missions is likely to begin in the next several years (*Ahrens* [1995],*Mizutani* [1995] and *Gavit and Powell* [1996]). Proposed applications of rigid penetrators in planetary exploration missions include

1. To anchor a lander on a small planet on which gravitational force is not strong enough to hold a lander steadily. The Champollion mission, which will be

launched in the year 2003 (*Ahrens* [1995]), will deploy a 3-meter long harpoon explosively to anchor the lander to a comet surface so that other activities may proceed in this low gravitation environment.

2. To deploy probes under planet surfaces. The Deep Space 2 mission, which is presently on the way to the Mars (*Gavit and Powell* [1996]), will use two penetrators to emplace thermal probes into the soil on Mars in order to determine the soil conductivity using the heat generated during penetration in the year 2000. The Champollion mission (*Ahrens* [1995]) will emplace several thermal probes that are used to determine thermal conductivity and temperature variation with depth inside a comet. The Lunar-A mission, which is presently being rescheduled (*Mizutani* [1995]), will carry three surface penetrators to the Moon. The three penetrators will emplace seismometers and heat flow probes at 1-3 meters depth below lunar surface at different locations in the near future.

3. To determine structures and properties of rocks, soils, or low temperature ice on a planetary surface. For example, penetrator deceleration time history can be used to determine the structure, density and strength of rocks, soils, or low temperature ice along the penetration path. The Deep Space 2 mission (*Gavit and Powell* [1996]) uses several on-board accelerometers to measure the force history during penetration into soils. The Champollion mission (*Ahrens* [1995]) is also going to measure penetration depth-time history using the method developed in this work. The Lunar-A mission (*Mizutani* [1995]) will use the data collected during penetration to study the properties of the soils on the lunar surface.

In space exploration mission applications, one special feature that is different from other applications is that knowledge of the properties of penetration target is very limited, and there is no chance to redo it. Therefore, knowledge of penetration dynamics into various target materials is very important for both mission success and data interpretation. In the past 50 years, understanding of rigid penetration into various soft materials (soils, clays, sands and soft rocks like tuff) has been improved using on-board instrument measurements combined with numerical simulation (*Young* [1969], *Backman and Goldsmith* [1978], and *Heuze* [1990]) because of low resistance force and no crack generation during penetration. However, for high-strength brittle materials such as hard rocks and various concretes, a knowledge of rigid penetration dynamics is still deficient because of lack of proper methods to measure penetration depth and/or velocity and/or deceleration time history due to very high decelerations. Therefore, it is important and also has practical applications to develop measurement methods that can provide the time history of penetration into brittle materials and to understand the relations among material properties and the time histories. In the next two sections, I give a short review and make some general comments regarding previous work on rigid body penetration into brittle materials.

## 1.1 Experimental method

The basic experimental problem for penetration dynamics is the measurement of the time histories of various variables, such as penetration depth, projectile velocity, projectile deceleration, as well as the stress field, in target materials during penetration. Previous penetration studies employed different combinations of projectile and target materials in different velocity ranges (*Backman and Goldsmith* [1978], *Zukas* [1990], *Hohler and Stilp* [1990], *Zukas and Walters* [1990], *Recht* [1990], and *Stilp and Hohler* [1990]). Most of these experiments that simply recovered targets were designed to investigate the relations between initial projectile velocity/energy and penetration depth/crater volume. In order to study penetration dynamics, a number of researchers (*Masket* [1949], *Persson* [1976], *Levy and Goldsmith* [1984], *Virostek et al.* [1987], *Forrestal and Luk* [1992], and *Zhu et al.* [1992]) have attempted to measure penetration depth, velocity, and deceleration time history during penetration. The measurement methods employed include: (1) High-speed photography to measure penetration depth-time history (*Masket* [1949], *Persson* [1976] and *Zhu et al.* [1992]); (2) Laser Doppler anemometry to determine projectile velocity-time history

(*Wu et al.* [1994]); (3) On-board accelerometers to record deceleration time history (*Levy and Goldsmith* [1984], *Virostek et al.* [1987], and *Forrestal and Luk* [1992]); (4) Reversed experiments to measure strain, stress and particle velocity in projectile materials (*Bless et al.* [1978]). The typical advantages and draw backs of these methods are summarized as follows:

1. High-speed photography:

   This obvious technique was first used to monitor projectile position during penetration by *Masket* [1949]. Most recently it was adopted by *Zhu et al.* [1992]. Although it is simple to use, the draw backs of this method are: (1) Few data are obtained from each experiment; (2) Impact-induced fine ejecta and smoke from projectile launchers can interfere with illumination; (3) Spatial resolution is very low because of light scattering and very large ratio of object (projectile) to image (projectile projection on film).

2. Laser Doppler anemometry:

   This method involves measurement of the frequency shift of laser light reflected by the lateral surface of the projectile. The frequency shift is related to the velocity of a projectile that is moving through a coherent light-interfered black/white stripe field (*Durst et al.* [1981], *Birch and Jones* [1990], and *Wu et al.* [1994]). This method can measure the velocity-time history directly and continuously. The disadvantages are: (1) Data reduction can be difficult because of a very high inherent noise level that needs to be determined arbitrarily as a cut-off level for the velocity calculation; (2) The method is sensitive to dust motion and air flow changes in the path of the laser beam; (3) Because the measured projectile velocity is related to the width and sharpness of coherent light-interfered black/white stripes, the distance between the projectile surface and the laser probe must be very accurate.

3. On-board instruments:

   In this method, accelerometers are installed inside a projectile body to record projectile deceleration time history during penetration. The advantage of this method is that the resistance force acting on the projectile can be measured directly and continuously if certain requirements, such as a rigid connection between the accelerometers and the projectile body, and sufficient bandwidth of accelerometers, are satisfied. For soft target materials like foam and soils, deceleration on the order of 10 - $10^3$ g was already measured with commercial accelerometers when initial projectile velocity was around 200 m/s (*Forrestal et al.* [1990], and *Heuze* [1990]) although the recorded deceleration time history was very noisy due to shock loading and structure response.

The major disadvantages of this method are: (1) Commercial accelerometers (Togami et al. [1996]) are not able to respond to very high accelerations properly ( e.g., $> 10^4$ g, which can result from impacts onto hard brittle materials like concrete with velocity 200 m/s); (2) The screws that are used to mount the accelerometers to the projectile body yield upon high deceleration; (3) It is difficult to protect on-board circuitry and chips that are used to record data during penetration from disturbance and damage under high deceleration.

4. Reversed experimental method:

   Reversed experiments mean that a projectile is fixed and a target medium is launched at the projectile. Particle velocity and/or strain is measured in the projectile material using strain gauges and/or a VISAR (*Bless et al.* [1978] and *Forrestal* [1984]). It is obvious that reversed experiments yield different results than forward penetration experiments. This occurs because, given the small size of the target, cracks (radial and lateral cracks) formed during penetration propagate to the target free surfaces at a velocity that is much higher than the rigid body penetration velocity, result in target splitting, and cause the penetration to be greater in reversed tests than in forward tests (limitations of launching the target at high speed prevent a large enough target from being used). Thus, the results from reversed experiments cannot be used to describe forward penetration.

## 1.2 Theoretical background

### 1.2.1 Phenomenological/empirical method

From two-end-point experimental data (initial impact velocity/energy and final penetration depth/volume), many different relations between penetration depth/volume and impact velocity/energy have been proposed to describe rigid body penetration into soils, rocks and concretes (*Backman and Goldsmith* [1978], *Forrestal* [1986], *Heuze* [1990], *Zukas* [1990], *Hohler and Stilp* [1990], and *Zukas and Walters* [1990]). I summarize here a number of relations between final penetration depth, $P_{max}$, and initial projectile velocity, $v$. In the following, $m$ and $A$ are projectile mass and cross-sectional area, respectively. All parameters used in the following relations are in SI unit. Typical expressions are

1. *Backman and Goldsmith* [1978] listed several previous relations as

$$P_{max} = \frac{m}{2a_2}\ln(1 + \frac{a_2}{a_0}v^2), \tag{1.1}$$

$$P_{max} = \frac{m}{a_2}\ln(1 + \frac{a_2 v}{a_1}), \tag{1.2}$$

$$P_{max} = \frac{mk}{A}\log(1 + \frac{v^2}{20000}), \tag{1.3}$$

   Eqs. (1.1), (1.2) and (1.3) were suggested by *Poncelet* [1830], *Resal* [1895] and *Petry* [1910], respectively. $a_0$, $a_1$, $a_2$ and $k$ are empirical constants that are determined from penetration experimental data. Table 2 in *Backman and Goldsmith* [1978] lists the values of the empirical constants for several soft soils.

2. From the experimental data of rigid body penetration into soils, *Young* [1969] suggested

$$P_{max} = 0.16S \times N(\frac{m}{A})^{0.5}\ln(1 + \frac{v^2}{4645}), \qquad v < 61 \text{ m/s},$$

$$P_{max} = 9.4 \times 10^{-4} S \times N(\frac{m}{A})^{0.5}(v - 30.5), \quad v > 61 \text{ m/s}, \tag{1.4}$$

where $v$ is in the range of 30 to 370 m/s. $S$ is defined as a soil constant that is determined using penetration data, and varies from 2.5 to 50 for different soils (see Table 3 in *Young* [1969]). $N$ is defined as a projectile nose-performance coefficient that is determined using penetration data for different nose shapes, and varies from 1 for an ogive head to 0.56 for a flat head (see Table 2 in *Young* [1969]).

3. Based on the experimental data of rigid body penetration into rock and concrete targets, Sandia National Laboratories (*Heuze* [1990]) suggested

$$P_{max} = 1.14 \times 10^{-6} S \times N\frac{m}{A}(v - 100), \tag{1.5}$$

where $S$ and $N$ are defined as the target penetrability number (a measure of rock resistance) and the projectile nose performance coefficient.

4. *Forrestal* [1986] suggested that the final penetration depth of a projectile with an ogive head (Figure 1.1) is

$$P_{max} = \frac{m}{2A\rho z}\ln(1 + \frac{\rho v_1^2 z}{B}) + 4R, \quad P_{max} > 4R, \tag{1.6}$$

where $R$ is projectile radius, and $B$ is a empirical constant. $v_1$ and $z$ are defined as

$$\begin{aligned} v_1^2 &= v^2 - \frac{4\pi R^3 B}{m}, \\ z &= \frac{4R_o R - R^2}{6R_o}, \end{aligned}$$

where $R_o$ is the ogive head radius (Figure 1.1).

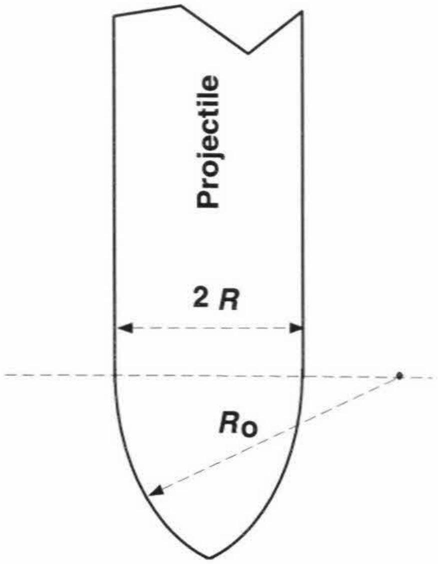

Figure 1.1: Sketch of a projectile with ogive head.

5. Based on the experimental data of penetration into rock and concrete targets in the velocity range of 200 to 1000 m/s, Army's Waterways Experiment Station (*Heuze* [1990]) proposed

$$P_{max} = \frac{m}{A}\frac{N_{rc}}{\rho}[\frac{v}{3}(\frac{\rho}{\sigma_{cr}})^{0.5} - \frac{4}{9}\ln(1 + \frac{3v}{4}(\frac{\rho}{\sigma_{cr}})^{0.5})], \tag{1.7}$$

where $\rho$ is target material density, and

$$\begin{aligned} N_{rc} &= 0.863(\frac{4(\mathrm{CRH})^2}{4\mathrm{CRH}-1})^{0.25}, \quad \text{for an ogive head projectile ,} \\ N_{rc} &= 0.805\sin^{-0.5}(\theta), \quad \text{for a cone head projectile,} \\ \sigma_{rc} &= \sigma_f(\frac{\mathrm{RQD}}{100})^{0.2}, \end{aligned}$$

where $\sigma_f$ is the unconfined compressive strength of target materials and RQD is defined as the quality designation of rock targets, and is determined using penetration experimental data. $\theta$ is the half-angle of the projectile cone head. CRH is defined to be $R_o/(2R)$ as shown in Figure 1.1 (*Forrestal et al.* [1992]).

The advantage of empirical relations is that they can be used to predict penetration depth with high reliability under conditions similar to the experimental conditions. The disadvantages are: (1) They give very limited information about the dynamics during penetration. For a single set of experimental data, many different formulae can be used to fit the set (*Heuze* [1990]). Therefore, it is difficult to determine which relation is more reasonable than the others. (2) How to scale empirical relations under experimental conditions to different conditions is still an unsolved problem because of the complexity of penetration processes.

### 1.2.2 First principle method

Because of their applicability to rigid body penetration dynamics, analytic and numerical first principle models have received a great deal of attention during the past few decades (*Hopkins* [1960], *Backman and Goldsmith* [1978], *Zukas* [1990], *Corbett et al.* [1996], *Forrestal and Tzou* [1998], and *Goldsmith* [1999]). The following is a very brief summary of previous work on analytic and numerical models for penetration.

#### Analytical models

For rigid body penetration processes, a simple analytical model would include:

1. Penetration equation:

   Because projectiles are assumed to be rigid during penetration, the equation for projectile motion is the Newton's second law:

$$m\frac{dv(t)}{dt} = F(t), \tag{1.8}$$

where $t$ is time, $v(t)$ is projectile velocity and $F(t)$ is resistance force acting on the projectile during penetration. The core problem is to determine what is $F(t)$ during penetration.

2. Force models:

   Only two groups of analytical models have been used to estimate the resistance force during rigid body penetration: the cavity expansion model (*Hill* [1950] and *Hopkins* [1960]) and the modified Bernoulli equation (*Anderson et al.* [1996]).

   (a) Cavity expansion model:

   The cavity expansion model includes spherical and cylindrical geometries. They were first used to describe indenter problems by *Bishop et al.* [1945]. *Hill* [1950] suggested that the pressure acting on the cavity surface during cavity expansion is the energy needed to create a unit volume cavity if friction can be neglected. Then, many solutions for dynamic sphere cavity expansion were derived to describe resistance force during rigid body penetration into ductile and brittle materials (*Hill* [1950]; *Hopkins* [1960]; *Hunter and Crozier* [1968]; *Hanagud and Ross* [1971]; *Forrestal and Longcope* [1982], *Forrestal* [1984], *Forrestal et al.* [1990], *Forrestal et al.* [1992] , *Forrestal and Luk* [1992], *Xu et al.* [1997], and *Forrestal and Tzou* [1998]). Due to the length and complexity of mathematical derivation of each solution, I just list several final solutions derived from spherical cavity expansion models.

   i. Based on the assumptions that (1) all parameters (stress, particle velocity, strain) along the radial direction are chosen to be continuous across the elastic-plastic boundary and (2) energy transferring velocity is infinite, *Hill* (*Hunter and Crozier* [1968]) gave the spherical cavity expansion pressure for an incompressible ideal plastic ductile material as

$$\sigma = \frac{2}{3}Y(1 + \ln(\frac{2G}{Y})) + \rho(R_c\frac{dv_c}{dt} + \frac{3}{2}v_c^2) \qquad (1.9)$$

where $G$ and $Y$ are material shear modulus and yield strength, respectively. $R_c$ and $v_c$ are cavity radius and cavity expansion velocity, respectively. This solution is only applicable when cavity expansion velocity is much smaller than finite plastic deformation wave velocity (*Hunter and Crozier* [1968]). The important conclusion from this solution is that the expansion pressure of a spherical cavity depends on initial cavity radius, cavity expansion velocity and the acceleration of cavity expansion.

ii. Assuming that (1) target material response to impact is locked-elastic-locked-plastic with linear compressible strain-hardening (locked-elastic and locked-plastic means that material density in elastic and plastic regions is constant), (2) the penetration depth is much larger than the projectile diameter, (3) the resistance pressure acting on projectiles is equal to cavity expansion pressure, (4) the particle velocity in the elastic deformation region is zero and (5) the symmetric spatial variation of dynamic pressure around the frontal surface of a spherical projectile follows a cosine variation, *Hanagud and Ross* [1971] derived a solution as

$$\sigma = \sigma_s + \frac{2\pi\rho}{3}(B_1 R_c \frac{dv_c}{dt} + B_2 v_c^2), \tag{1.10}$$

$$P_{max} = 2R + \frac{3}{4}\frac{\frac{m}{A} + B_1 \frac{2R}{3}\rho_l}{B_2\rho_l}\ln(\frac{\sigma_s + \frac{2}{3}B_2\rho_l v^2}{\sigma_s}), \tag{1.11}$$

where

$$\sigma_s = \frac{4}{9}E(1 - \exp(-3\beta)) - \frac{2}{3}Y\ln(\delta) + \frac{2}{27}\pi^2 E_t - \frac{4}{9}E_t\eta, \tag{1.12}$$

$$\begin{aligned} B_1 &= 1 - \delta^{1/3}, \\ B_2 &= \frac{3}{2} - (1+\delta)\delta^{1/3} + \frac{1}{2}\delta^{4/3}, \end{aligned}$$

$$\begin{aligned}\delta &= 1-\exp(-3\beta)\frac{\rho}{\rho_l},\\ \beta &= \frac{Y}{2E},\\ \eta &= \sum_{n=1}^{\infty}\frac{(1-\frac{\exp(-3\beta)\rho}{\rho_l})^n}{n^2},\end{aligned} \tag{1.13}$$

where $\rho_l$ is the density in locked-plastic deformation region, $E_t$ is the tangent modulus for linear strain-hardening, and $2R$ is the projectile diameter. Once again, this solution shows that spherical cavity expansion pressure depends on cavity radius, cavity expansion velocity and cavity expansion acceleration. However, the interesting thing is that although the solution is true only for deep penetration defined as $P_{max}/2R > 4$ in *Hanagud and Ross* [1971], they compared it with the experimental data in the range of $1 < P_{max}/(2R) < 3$, and the prediction from the model is in good agreement with the experimental data. In addition, although they claimed that the solution is for elastic-plastic materials, it is really just for plastic materials because the particle velocity after passage of the elastic wave is assumed to be zero.

iii. Based on the assumptions that (1) the cavity expansion velocity is constant, and (2) cavity expansion is self similar, *Hunter and Crozier* [1968] derived a solution for elastic-plastic compressible materials under very low cavity expansion velocity as

$$\sigma = \rho C_p^2[\exp(\frac{2Y}{3\rho C_p^2}(1+\ln(\frac{2\mu}{Y}))) + (\frac{v}{C_p})^2 Z(\frac{v}{C_p},\nu,\frac{Y}{\rho C_p^2}) - 1], \tag{1.14}$$

where $\nu$ is the Poisson's ratio of the target material, $C_p$ is the velocity of a small amplitude plastic deformation wave and $Z$ is a very complicated function. The most important conclusion from the solution is that the cavity expansion pressure depends only on the cavity expansion velocity. For higher expansion velocity (say $v \sim C_p$ ), *Hunter and Crozier* [1968] predicted that the plastic-elastic boundary propagates as a shock wave.

iv. Under the assumptions that are (1) cavity expansion velocity is constant, (2) all boundaries (plastic-cracked, cracked-elastic) propagate at constant velocity, (3) particle velocity, stress and displacement are continuous across the boundaries, (4) the relation between cavity expansion pressure and non-constant cavity expansion velocity can be obtained using superposition of solutions under different constant cavity expansion velocity, *Forrestal and Tzou* [1998] gave several solutions for brittle materials with different models. For brittle materials with an elastic-cracked-plastic response, the solution is

$$\sigma = \tau \frac{3+2\lambda}{\lambda(3-\lambda)} \varpi^{-\alpha\lambda} - \frac{\tau}{\lambda} + \frac{6\rho v^2 + 2\rho v^2(\varpi(\alpha\lambda - 4) - \varpi^4(\alpha\lambda - 1))\varpi^{-\alpha\lambda}}{(\alpha\lambda - 1)(\alpha\lambda - 4)}, \tag{1.15}$$

where

$$\varpi^3 = \frac{1}{2\beta^2} \frac{(\frac{\beta}{\beta_1})^2 \frac{Y}{\tau} - S_3}{\frac{\beta}{\beta_1}(1 - \frac{\beta}{\beta_1})}, \tag{1.16}$$

$$S_3 = \frac{2T(\frac{2E}{3\tau} + 3\beta_1^2)}{\frac{2E}{3\tau} - 6\beta_1^2}, \tag{1.17}$$

$$\beta = \beta_1^3 \frac{\tau}{Y} [\frac{2TY(E + 9\tau\beta_1^2)}{\beta_1^4 \tau(E - 9\tau\beta_1^2)} + [\frac{9T\tau}{2(E - 9\tau\beta_1^2)}]^2]^{\frac{1}{2}} - \frac{9\beta_1^3 \tau^2 T}{2Y(E - 9\tau\beta_1^2)}, \tag{1.18}$$

where $\varpi = v/c$ in which $c$ is the velocity of propagation of the cracked-plastic boundary, $\beta = c/c_y$, $\beta_1 = c_1/c_y$ in which $c_1$ is the velocity of propagation of the elastic-cracked boundary, $c_y^2 = \tau/\rho$, $T = f_0/\tau$ in which $f_0$ is the tensile strength of the target material and $\tau = (3 - \lambda)Y/3$ in which $\lambda$ is a material constant. *Forrestal and Tzou* [1998] claimed that all the parameters are determined through an inverse procedure. The inverse procedure is (1) first to give an arbitrary value to $\beta_1$, (2) to calculate $\beta$ using Eq. (1.18), (3) to determine $\varpi$ using Eqs. (1.16) and (1.17), and (4) finally to calculate $\sigma$ under constant expansion velocity $v$ using Eq. (1.15). Basically, what they claimed is that the four parameters ($\sigma$, $\beta$, $\beta_1$ and $\varpi$) can be determined uniquely using three equations (Eqs. (1.15), (1.16) and (1.18)). And the predictions from the solution are in very good agreement with the experimental data. Here, one undetermined thing is what constrains the value of $\beta_1$. $\beta_1$ determines the velocity of the boundary between the elastic region and the cracked region. This velocity should be controlled by crack propagation and is not an arbitrary number. Eqs. (1.15), (1.16) and (1.18) mean that $\sigma$ is a function of $v$, $c_1$ and $c$. If $v$ is given, the relation is $\sigma(c_1, c) = 0$, which says that for a constant $\sigma$, $c = c(c_1)$. Therefore, the reverse procedure only picks up one of the infinite solutions determined through $c = c(c_1)$.

In order to see how good cavity model predictions are, Figure 1.2 (*Heuze* [1990]) demonstrates the comparison among experimental data and predictions from empirical relations and cavity expansion models for a rigid body penetration into soft soils. The comparison clearly shows that the predictions from both spherical and cylindrical cavity models do not agree well with from the experimental data even for a very soft target. Based on the above discussion and comparison, several issues related to cavity expansion models need to be clarified in future. They are:

A. Superposition principle:

In the models suggested by *Forrestal and Tzou* [1998], the superposition principle is used, i.e., the solution for a penetration process in which the penetration velocity varies from initial velocity to zero is the superposition of the solutions from a series of constant cavity expansion velocity. However, *Hanagud and Ross* [1971] and

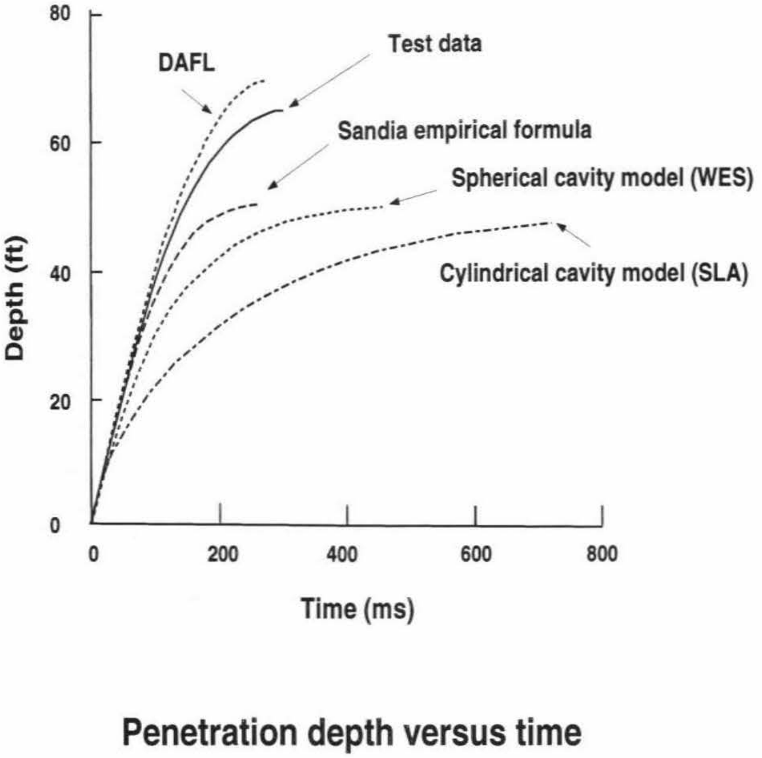

Figure 1.2: Comparison between experimental data and model predictions on penetration into soil after *Heuze* [1990]. Test data was for a 180 kg, 16.2 cm diameter projectile to penetrate into soil (glacial lacustrine deposit composed of alternating thin layers of sands, silts and clays) at the Watching Hill Blast Range, Ralston, Canada at velocity 150 m/s. DAFL is code prediction based on a empirical relation (details on it are not published) (AVCO Corporation). Details on Sandia empirical formula are not available. WES is U.S. Army Waterways Experiments Station, Vicksburg, MS. SLA is Sandia National Laboratories, Albuquerque, NM.

*Hunter and Crozier* [1968] clearly showed that the superposition principle is not applicable in cavity expansion models if the cavity velocity is not assumed to be constant. Therefore, future work is needed to validate the applicability of the superposition principle for non-constant velocity of cavity expansion.

B. Plastic deformation propagation velocity:

In all cavity models, different assumptions were used to avoid dealing with elastic-plastic boundary propagation because the boundary can propagate at any velocity in the velocity range of zero to plastic wave velocity, as discussed in detail by *Hopkins* [1960]. However, the boundary velocity is the most important parameter in cavity expansion models because it controls the whole stress field inside the target material. In order to really solve the cavity expansion problem under the assumptions related to material properties, the boundary propagation velocity needs to be constrained.

C. Friction contributions:

The use of the cavity expansion model for penetration problem is based on the assumption that frictional effects can be ignored during penetration (*Hill* [1950]). Experimental data do show that friction plays an important role in rigid body penetration (*Heuze* [1990]). If the friction effect cannot be ignored during penetration, future research is needed to validate the application of the cavity expansion model to penetration.

(b) Modified Bernoulli equation

The modified Bernoulli equation was first proposed by *Tate* [1967] for moderate impact velocity (1 - 3 km/s). A term is added to the original Bernoulli equation in order to account for the effect of material strength on penetration. The modified Bernoulli equation is

$$\rho_p L \frac{dv}{dt} = -(\frac{1}{2}\rho v^2 + \sigma_d), \tag{1.19}$$

where $\rho_p$ is projectile material density, $L$ is projectile length, and $\sigma_d$ is an empirical parameter that reflects the effect of target material strength on penetration resistance. Recently, *Walker and Anderson* [1995] combined *Tate*'s model with the cavity expansion model, and gave an expression for rigid body penetration into elastic-plastic materials

$$\frac{dv}{dt}(\rho_p L + \rho R_c \frac{\alpha - 1}{\alpha + 1}) + \rho \frac{d\alpha}{dt} \frac{2R_c v}{(\alpha + 1)^2} = -(\frac{\rho v^2}{2} + \frac{7}{3}\ln(\alpha) Y), \tag{1.20}$$

$$(1 + \frac{\rho_t v^2}{Y})\sqrt{K - \rho\alpha^2 v^2} = (1 + \frac{\rho\alpha v^2}{2G})\sqrt{K - \rho v^2}, \tag{1.21}$$

where $\alpha$ is the ratio of the plastic deformation region radius to the cavity radius. $K$ is the bulk moduli of the target material. Assumptions used to derive the two expressions above include (1) the radial particle velocity in the target material follows $v((\alpha R_c/r)^2 - 1)/(2\alpha^2 - 1)$, which means that the radial velocity of particles in the target material is negative in the elastic deformation region ($r > R\alpha$), and (2) $d\alpha/dt = 0$ (Eq. (1.21) is derived under the assumption of $d\alpha/dt = 0$, but it is used in Eq. (1.20) in which $d\alpha/dt \neq 0$).

*Anderson et al.* [1996] suggested a force model for porous rocks assuming that failed target materials behave like fluid and there is no wave generation from penetration after impact. The force acting on a projectile is

$$F = \int_{ca} (\sigma_p + \sigma_d)(\cos\theta + \mu_f \sin\theta) ds, \tag{1.22}$$

where $\sigma_p$ and $\sigma_d$ are the resistance pressure due to projectile motion in fluid-like target materials and due to the strength of the target material, respectively.

$$\begin{aligned}\sigma_p &= \frac{1}{2}\rho\cos^2\theta v^2, \\ \sigma_d &= \sigma_f(1 - H(v - v_m)) + \sigma_f(\frac{v}{v_m})^n H(v - v_m),\end{aligned} \tag{1.23}$$

where $v_m$ and $n$ are material constants that are determined using penetration data. $H$ is Heaviside function, $\theta$ is the angle between the normal to projectile surface and the direction of projectile motion, $ca$ is the contact area between the projectile and the target materials, and $\mu_f$ is frictional coefficient. After $v_m$ and $n$ were determined using penetration data, the model predictions are in reasonable agreement with experimental data for several soft rocks with different porosity.

As summarized above, all the solutions derived under different assumptions were claimed to be in good agreement with experimental data on final penetration depth. I believe that in order to validate force models, one must compare the model prediction on penetration time history with experimental data. This has only been done by one author so far, *Forrestal* [1986], who compared the measured deceleration time history on soft rocks (tuff) with the prediction from cavity expansion models. The prediction was claimed to be in reasonably good agreement with the experimental data. But, Figure 1.2 shows that the penetration depth-time history predicted from both spherical and cylindrical cavity expansion models do not agree well with the experimental data. Because the predictions shown in Figure 1.2 were done before the penetration test, Figure 1.2 may demonstrate the real situation on cavity expansion model. In addition, all these comparisons and time-history measurements are only for soft target materials (deceleration <4000 g). No experimental data and comparisons have been published for hard targets (deceleration > $10^4$ g). Therefore, the time-history of penetration into hard targets is very important and necessary for developing analytic models.

### Numerical simulations

During the last 40 years, many numerical codes have been developed to simulate penetration into various materials (*Zukas* [1990] and *Corbett et al.* [1996]). When penetration velocity is higher than the maximum crack propagation velocity in brittle materials, numerical code predictions are generally in a reasonable agreement with experimental data (*Zukas* [1990] and *Corbett et al.* [1996]). However, when penetration velocity is below the maximum crack propagation velocity, predictions from numerical codes do not agree with experimental data if experimental data are not used to adjust numerical simulations. The first reason for this disagreement is that crack propagation plays a very important role in low velocity penetration into brittle materials but numerical methods still lack the sophisticated constitutive relations needed to properly characterize material behaviors with crack initiation and propagation. The second reason is that the friction coefficient on the contact area between projectile and target materials is very poorly constraint from experimental data because of the lack of a proper method to measure it. However, if a penetration time history is available, numerical method can be used to construct effective models that reflect the effects of friction coefficient and crack initiation and propagation on penetration at least.

## 1.3 Motivation

Based on the above brief review, it is obvious that the difficulty to develop or verify a first principle model results from a lack of experimental data on the time history of the variables involved in rigid body penetration into brittle materials. Experimental data on penetration time history are necessary to aid understanding penetration process and validate first principle methods. Although much more work needs to be done to fully include crack initiation and propagation during penetration into brittle materials in numerical codes, it is possible at present that a phenomenological model that includes the effect from cracking can be developed using the combination of numerical simulation with time-history experimental data on rigid body penetration into brittle materials. In order to obtain time-history data on rigid body penetration into brittle materials, the measurement method must have the following characteristics: (1) high resolution of both time and parameter value, (2) tolerance of a dusty environment and some of the uncertainty of projectile trajectory, (3) ability to work properly under $10^5$ g accelerations, and also (4) potential application in space missions. The first, third and fourth requirements rule out the high-speed photography method and the on-board instrument methods. The Doppler anemometry cannot satisfy the second and third requirements. Therefore, it is worth developing an experimental method that can be used to measure the depth time history of penetration into brittle materials.

The motivations for this research are: (1) to develop a method that can be used to measure penetration depth-time history, for potential application in space exploration missions, (2) to obtain an empirical model for time-dependent variables based on time-dependent data under different conditions, (3) to develop an analytic first-principle model that can approximately describe major penetration parameters, such as penetration duration, penetration depth-time history, and velocity/acceleration time-histories.

In the next three chapters, I describe the details of the experimental method, experimental results and a first principle penetration model.

# Chapter 2 Penetration depth time history measurement method

The requirements for a measurement method that has the ability to measure the depth time history of projectile penetration into hard brittle materials under velocity $10^2$ m/s are (1) to work properly under very high deceleration ( up to $10^5$ g), (2) to have enough spatial and time resolution to ensure that the experimental data is meaningful for shallow penetration depths (several centimeters), (3) to tolerate dust in the environment, projectile misalignment and changes in the projectile surface conditions, and (4) to have potential applications in space missions. As discussed in Chapter 1, the existing methods do not satisfy the requirements because of various reasons. In this work, a method is developed to measure the depth time history of rigid body penetration into brittle materials. The basic principle of the present method is that if the projectile body is assumed to be rigid during penetration, the time history of the projectile position relative to any point that is stationary relative to the target is identical to the projectile penetration depth-time history into the target. If the penetration depth-time history is measured with very dense points, the projectile penetration velocity can be deduced by differentiating the time history. The present method includes three crucial elements: (1) Projectile and sabot; (2) Sabot-projectile separator; (3) Detection and recording system. Figure 2.1 gives the experimental arrangement inside the 40 mm gun tank at Caltech. Figure 2.2 shows the optical system. The following is the detailed discussion of the three elements.

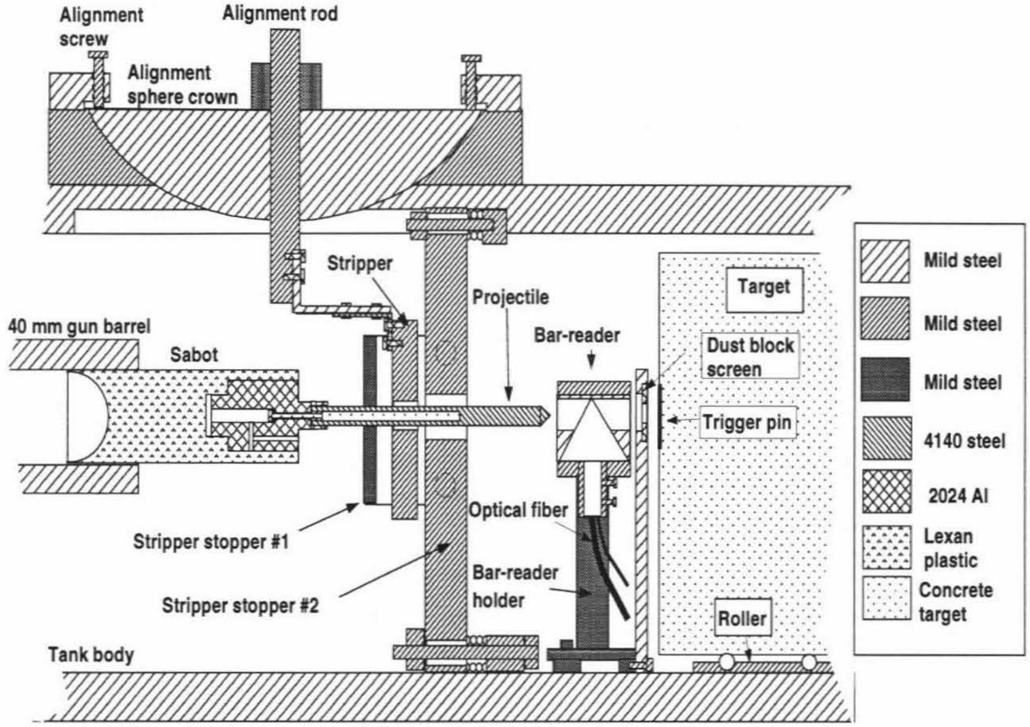

Figure 2.1: Experiment set-up. Stripper and bar-reader are aligned with the axis of 40 mm gun barrel using a laser beam that is along the gun barrel axis. Stripper stopper #1 is used to protect the barrel from the impact of stripper that bounces back after it strikes stripper stopper #2. Stripper stopper #2 is designed to prevent the stripper and sabots from following the projectile and also gun dust from interfering with the bar-reader during measurement. Recording system is triggered by a pin attached to impact surface. The trigger pin consists of two copper foils (0.1 mm thickness) that are insulated using a layer of mylar film (0.1 mm). Target (0.5 m diameter and 0.4 - 0.6 m long) sits on a roller and is fixed to tank body after it is aligned with the gun. Typical distance between the bar-code reader and target surface is ~ 2 cm. The distance between the bar-reader and the stripper is longer than projectile length.

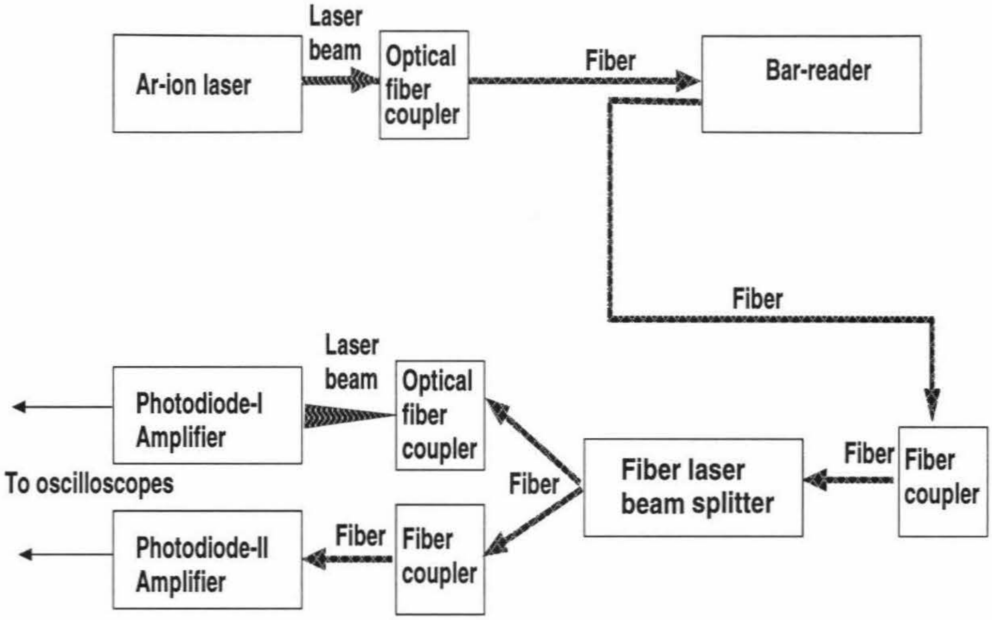

Figure 2.2: Schematic of optical and recording system. Ar-ion laser is Model 95 (Lexel Laser, Inc.) with maximum output 3 W. Laser power used in present experiments is about 0.7 W. Laser energy is coupled into a 50 $\mu$m core diameter optical fiber using a microlens(F915T, Newport). Fiber from bar-code reader to photodiodes is plastic fiber with a core diameter of 2 mm (DuPont). A one-to-two fiber beam splitter is used to distribute laser energy to two photodiodes. Photodiode-I with 20 mm$^2$ sensitive area is C30833(RCA). The bandwidth of Photodiode-I and amplifier is from 0.004 to 5 MHz. Because it has a very large sensitive area, an optical lens is used to enlarge the diameter of the laser beam from the fiber to fill the entire sensitive area. Photodiode-II with 0.8 mm$^2$ sensitive area is C5331-11(Hamamatsu). The bandwidth of Photodiode-II and its amplifier(APD module, Hamamatsu) is from 0.01 to 80 MHz. Laser energy from the fiber is directly coupled into Photodiode-II.

## 2.1 Projectile and sabot design

### 2.1.1 Rigid body assumption

The rigid body assumption is crucial for the validity of the technique to measure penetration depth time history. Therefore, it is necessary to explore the velocity range which supports the assumption. As an example, the projectile material is chosen to be 4140 steel and the target material is G-mixture mortar (the material properties are discussed in detail in Chapter 3). Based on the Hugoniot relations of the two materials (*Read and Maiden* [1971] and *Marsh* [1980]), peak shock wave pressure in the projectile and target materials is below 1.3 GPa when initial impact velocity is below 400 m/s. Because the Hugoniot elastic limit of 4140 steel is about 1.5 GPa, projectile body is subject to only elastic deformation for penetrations with initial impact velocity below 400 m/s.

### 2.1.2 Projectile and sabot design

In this method, a projectile body is basically used as a ruler to measure penetration depth. Black and white stripes are put on the projectile surface as labels. In order for the label method to work accurately, two issues are critical: the stripe width and integrity during launch.

#### Optimal stripe width

Stripe widths are very important because they affect both temporal and spatial measurement accuracy. However, there are some limitations imposed by the machining and by the detection system. In order to determine the optimal stripe width under various limitations, we first discuss the relationship between stripe width and reflected laser energy. Total laser energy reflected from projectile surface depends on the reflectivity of the projectile surface, the ratio of stripe width to laser beam width and also the intensity profile of incident laser beam energy. When a projectile with

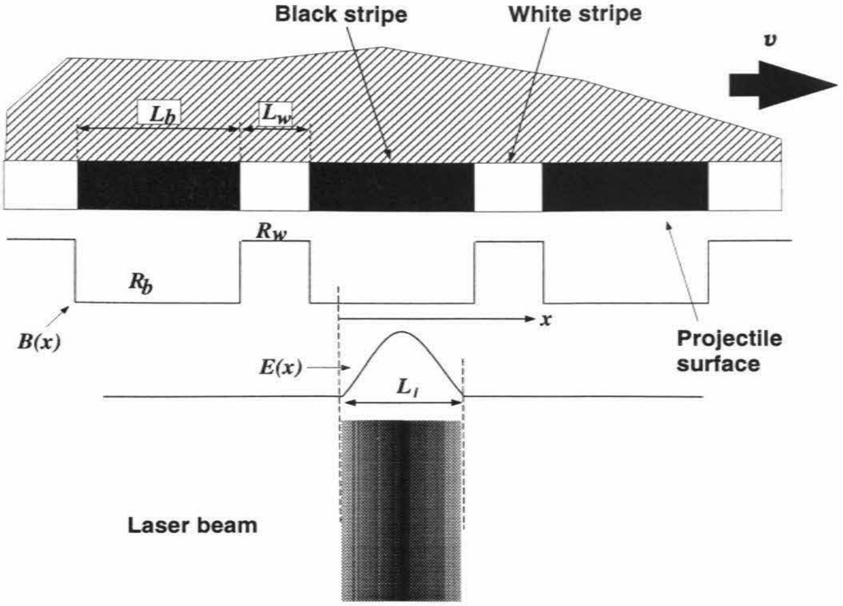

Figure 2.3: Convolution between laser energy and reflection function.

black and white stripe surface moves across a laser beam, laser energy reflected from the surface is a convolution integral between incident laser beam intensity profile and projectile surface reflectivity function as illustrated in Figure 2.3. We approximate the incident laser beam's intensity profile, $E(x)$, using a parabolic function as

$$E(x) = E_0 x(L_l - x), \qquad 0 \le x \le L_l, \tag{2.1}$$

$$E(x) = 0, \qquad x \le 0; x \ge L_l, \tag{2.2}$$

where $x$ is defined in Figure 2.3, $L_l$ is the diameter of the incident laser beam and $E_0$ is a constant. The surface reflectivity function, $B(x)$, is

$$B(x) = R_b, \qquad \text{for black stripes}, \tag{2.3}$$

$$B(x) = R_w, \qquad \text{for white stripes}, \tag{2.4}$$

where $R_b$ and $R_w$ are two constants. Therefore, the total reflected laser energy, $E_r$, at a given time is

$$E_r = B(x) * E(x), \tag{2.5}$$

where * specifies the convolution of two functions. This will vary with time due to the velocity of the projectile surface containing the stripes.

Figure 2.4 shows three possible scenarios with three different stripe width configurations. From Figure 2.4 it is seen that time-resolution is the highest when $L_l = L_w = L_b$. However due to deviation in assumed projectile distance from the laser beam focal surface and difficulties in consistently machining accurate stripe width, it is more practical to choose $L_w < L_l < L_b$. Under this condition, all peaks in reflected laser energy time series correspond to the moments at which the center of the incident laser beam hits the center of a white stripe. Therefore, stripe width is basically determined based on incident laser beam diameter. Since the VISAR probe (FOP-1000, Valyn International) that is used to focus the incident laser beam on the projectile surface has a focus diameter of $< 0.6$ mm, the actual widths used in experiments are $0.3 \pm 0.05$ mm for white stripes and $0.7 \pm 0.05$ mm for black stripes.

### Sabot design

Previous methods used to launch projectiles with a large length-to-diameter ratio were either to encapsulate a projectile inside plastic sabots (*Hohler and Stilp* [1990]) or to attach two separated sabots to a projectile by engaging screw threads that cut into the front-most and rear-most portion of the projectile (*Anderson et al.* [1996]). These methods damage stripes during launch and sabot-projectile separations. In order to launch projectiles without any damage to the stripes, the projectiles are designed to be held by a combination sabot that consists of aluminum and plastic sabots as shown in Figure 2.5. The aluminum sabot is used to prevent the projectile from penetrating into the plastic sabot during launch. It also prevents the plastic sabot following the projectile during and after sabot-projectile separation. Most importantly upon machining the projectile-sabot assembly, it is crucial to ensure that the projectile

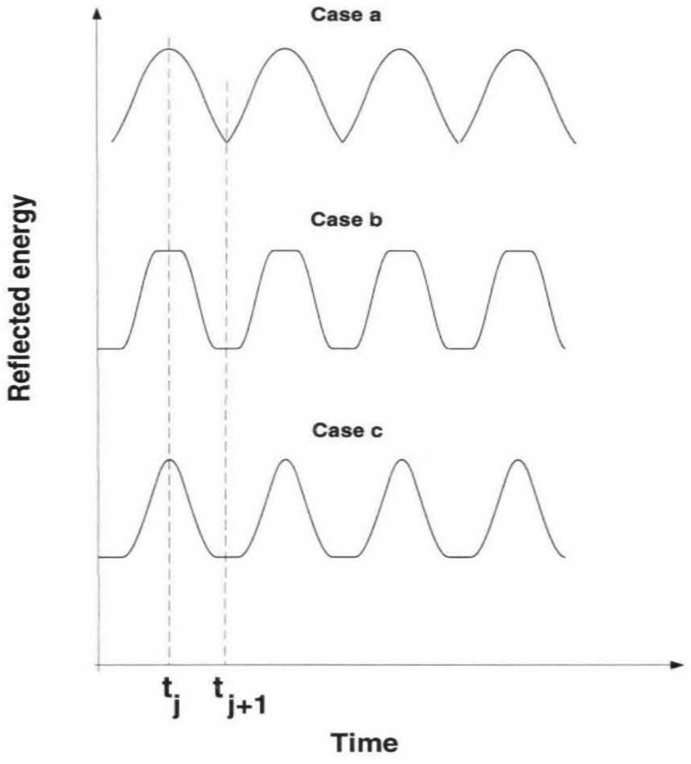

Figure 2.4: Three possible reflected energy variation with time. For Case a, $L_l = L_w = L_b$; For Case b, $L_l < L_w, L_l < L_b$ and $L_l < (L_w + L_b)$; For Case c, $L_w < L_l < L_b$ and $L_l < (L_w + L_b)$. $t_j$ and $t_{j+1}$ indicate the time at which the centers of $j$th white stripe and $(j+1)$th black stripe pass the center of incident laser beam, respectively.

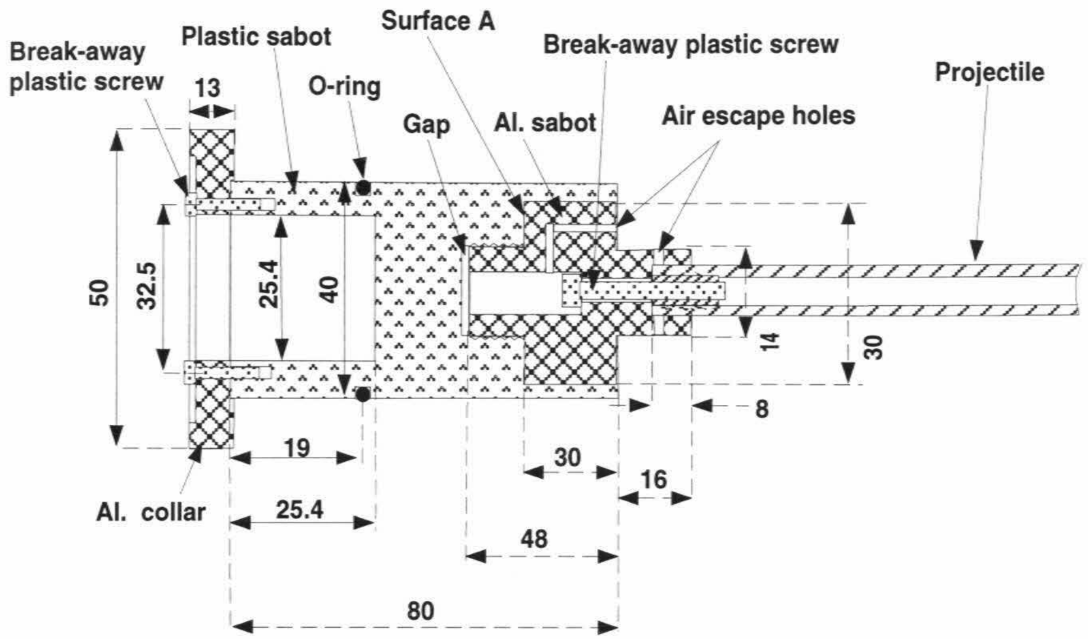

Figure 2.5: Sabot-projectile assembly. All dimensions are in mm. Aluminum sabot is threaded into plastic sabot. The alignment of the aluminum sabot to the plastic sabot is obtained using surface A as a reference surface. Gap between aluminum and plastic sabot is used to minimize direct shock to projectile from waves in plastic sabot. Holes in aluminum sabot are designed to let air escape during assembling and under vacuum.

axis aligns with the sabot axis. A misalignment will result in experiment failure. In order to retain the alignment, an 8 mm long hollow cylinder is used to assure that the projectile axis is aligned with the sabot axis, and a plastic screw is used to tighten them together.

### Procedure to machine stripes

Figure 2.6 gives the dimensions of the bar-coded projectile used in the present experiments. A hollow projectile is used to simulate most of practical applications of rigid body penetration. The hole depth, $Lh$, limited by machining ability is $\sim$ 76 mm for projectiles with length $Lp$ of 100 mm and $\sim$ 118 mm for projectiles with 150 mm length, respectively. The diameter of the hole is 6 mm for 10 mm diameter projectiles, and 10 mm for 15 mm diameter projectiles, respectively. Projectile head length, $H$,

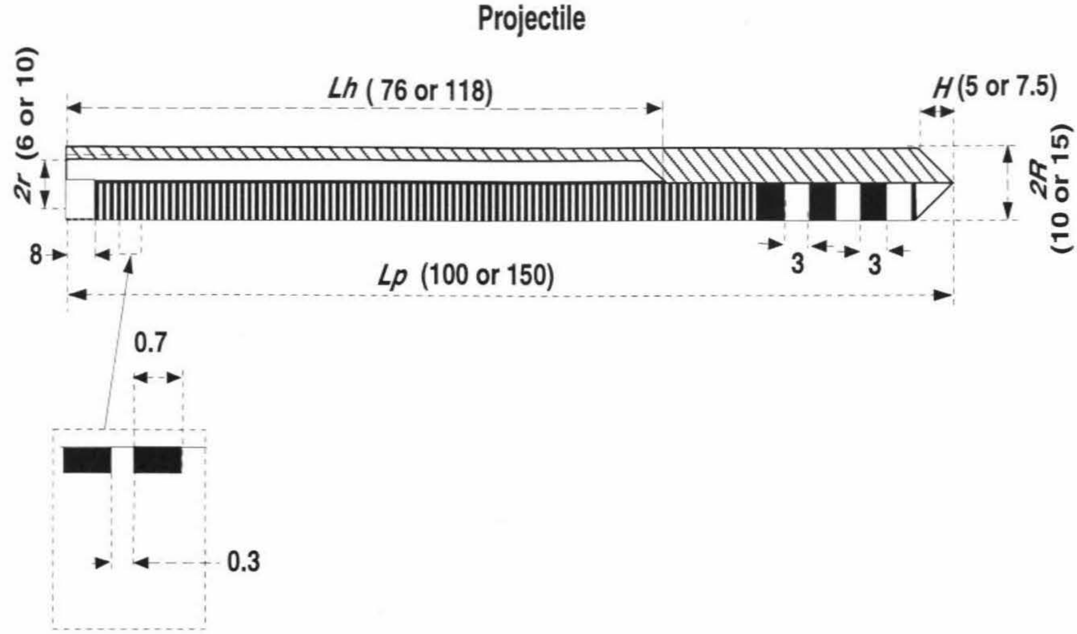

Figure 2.6: Black/white stripe pattern affixed to projectiles in present study. All dimensions are in mm. The stripes near the projectile head are wider to save machining time because this part only provides initial projectile velocity.

is half the projectile diameter. The procedure to machine black and white stripes is (1) To machine the oversized projectile to final dimensions after it is assembled with sabots together in order to align it with the sabots; (2) To polish the projectile surface with #100 sandpaper to increase the diffusivity of the projectile surface; (3) To paint the projectile surface using dark ink; (4) To cut off the paint to form white stripes using a cutting tool with a pre-designed width and sharp edge after the ink dries throughly; (5) To use an optical micrometer to measure stripe width.

## 2.2 Sabot-projectile separation system

In order to conduct penetration measurements free of interference from sabot impact effects, it is necessary to separate the sabots from the projectile immediately after they exit the gun barrel. The key issue in the design of the sabot-projectile separation system is to ensure that the separation process does not disturb the projectile trajectory and has a minimal effect on projectile velocity. This appears to be more important for

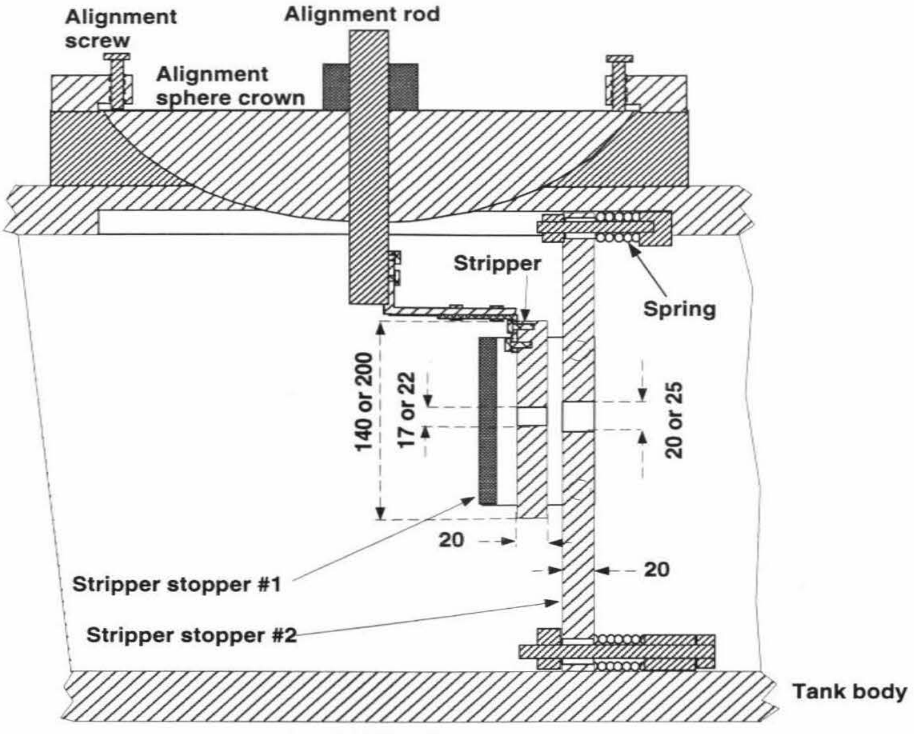

Figure 2.7: Sabot-projectile separation system. All dimensions are in mm. Stripper is designed only to separate sabots from projectile but not to stop sabots. Stopper #2 is used to stop sabots and stripper. Since stripper and sabots have already been separated from projectile when they impact on stopper #2, its dimensions are not crucial. Stopper #1 is used to protect gun barrel from impact by sabots bouncing back from the stripper.

low velocities ($10^2$ m/s). The sabot-projectile separation system used in this work is shown in Figure 2.7. Figure 2.8 schematically shows the separation process. Because projectile velocity is relative low, separation takes a relatively long time, which means that asymmetries in the stripper assembly must be properly considered. Otherwise reflected waves from the stripper edges may influence the projectile trajectory.

### 2.2.1 Stripper design criteria

After stripper material is chosen to be 1020 steel, the stripper plate dimensions (plate thickness and diameter) are determined based on proper consideration of the impact

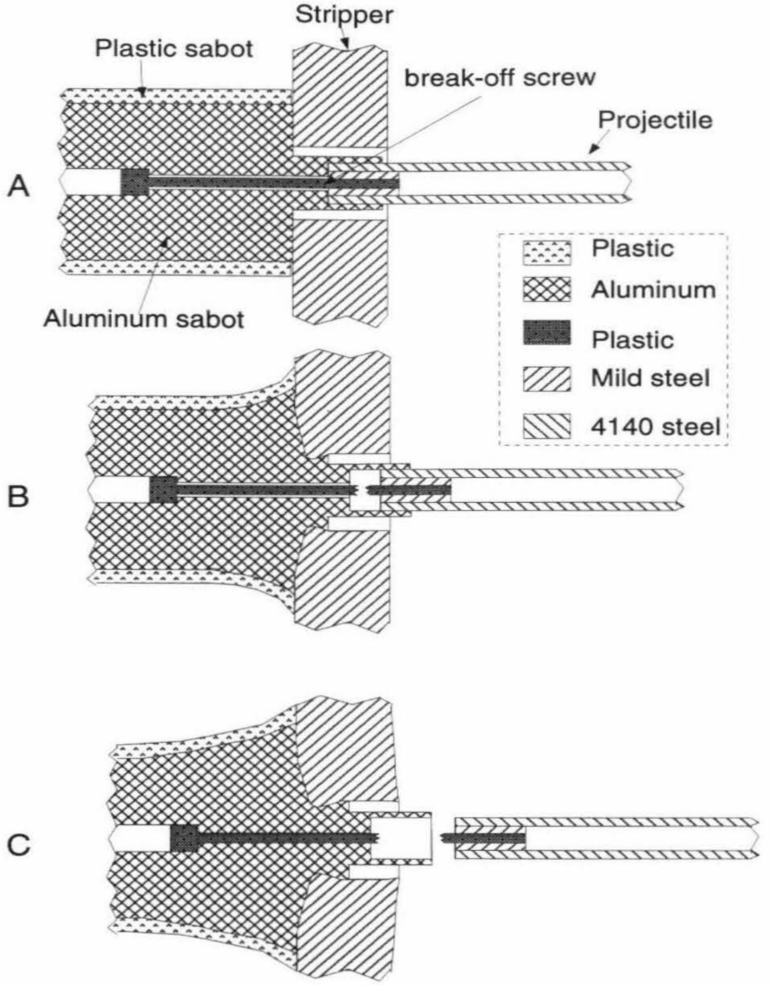

Figure 2.8: Schematic of sabot-projectile separation process. A: Sabots just impact stripper. B: Sabots are slowed down due to stripper resistance. Velocity difference between projectile and sabots is sufficient to break plastic screw that is used to hold projectile and sabots together. C: Sabots are separated from projectile.

process.

The criterion used to determine minimum plate thickness is that sabots should not plug the stripper plate after the sabots impact the stripper. The energy, $W$, needed for a flat-end projectile to plug a plate is estimated using (*Woodward,* [1990])

$$W = \frac{\pi d h^2 \sigma_0}{2\sqrt{3}}, \tag{2.6}$$

where $h$ and $d$ are stripper plate thickness and sabot diameter, respectively, and $\sigma_0$ is stripper plate yield stress. Assuming that all of the initial kinetic energy of sabots is used to plug the stripper plate, we have

$$\frac{1}{2} m_s v_0^2 = \frac{\pi d h^2 \sigma_0}{2\sqrt{3}}, \tag{2.7}$$

where $m_s$ and $v_0$ are sabot weight and initial velocity. The maximum stripper plate thickness that can be plugged by the sabots is therefore

$$h = \left(\frac{\sqrt{3} m_s}{\pi d \sigma_0}\right)^{\frac{1}{2}} v_0. \tag{2.8}$$

For 1020 mild steel, $\sigma_0$ is about 0.5 GPa (*Theodore and Rajendran* [1990]). Then, $h$ is estimated to be $\sim 0.02$ m when $v_0 = 400$ m/s, $m_s = 0.1$ kg and $d = 0.04$ m. In reality, only part of the initial kinetic energy of sabots is available for plugging the stripper plate, therefore, it is safe to choose the stripper plate thickness to be 0.02 m when the sabot velocity is below 400 m/s.

The criterion used to estimate stripper plate diameter is that the diameter must be large enough so that waves reflected back from the plate edge do not interfere with separation process, i.e., that asymmetry on the plate edge will not affect projectile trajectory. Shock waves generated by the impact propagate into both sabot and stripper materials. The shock waves in the stripper plate are converted to compressive, shear and surface waves upon interaction with the stripper plate free-surfaces. The total distance that body waves in the stripper plate propagate depends on both the plate radius and the wave incident angles at the free surfaces. For simplicity, assuming that all incident angles are $45^o$, the total distance is $\sqrt{2}\phi/2$, where $\phi$ is the stripper plate diameter. Although the shock waves from the initial impact decelerate the center part of sabots, the main deceleration of the sabots comes from the velocity difference between the stripper-sabot interface and the sabot interior just behind the projectile. This velocity difference continues to generate shear and surface waves which decelerate the central part until the difference vanishes.

Assuming that sabot materials stay together with stripper plate after impact and conservation of energy is applicable, the final velocity of the sabot and stripper plate, $v_f^0$, is

$$v_f^0 = (\frac{m_s}{m_s + m_{sp}})^{\frac{1}{2}} v_0, \tag{2.9}$$

where $m_s$ and $m_{sp}$ are sabot and stripper plate mass, respectively.

Because the sabot material has lower strength than the stripper plate material, the sabot will penetrate into the hole on the stripper plate after impact. This penetration increases effective separation length that includes the initial contact length between the projectile and the sabot and also the length that is due to the penetration. Because only the energy carried by the part of the sabot inside the hole diameter is available for the penetration, penetration depth, $H_p$, can be estimated (*Woodward,* [1990]) as

$$H_p = (\frac{\sqrt{3}}{\pi d_s \sigma_s} m_c (v_0^2 - (v_f^0)^2))^{\frac{1}{2}}, \tag{2.10}$$

where $m_c$ is the mass of the sabot, and $d_s$ and $\sigma_s$ are hole diameter and yield strength of the sabot material, respectively.

Therefore, the total separation length is $H_0 + H_p$ where $H_0$ is the initial contact length between the aluminum sabot and the projectile. Then, the separation duration, $t_s$ is estimated using

$$H_0 + H_p = \int_0^{t_s} (v_0 - v_f(t)) dt, \tag{2.11}$$

where $v_f(t)$ is the velocity of the central part of the sabot at time $t$ after impact.

In order to solve Eq.(2.11) for $t_s$, we assume that the stripper velocity increases from zero to $v_f^0$ exponentially as

$$v_f(t) = v_f^0(1 - e^{-t/k}), \tag{2.12}$$

where $k$ is a time constant that reflects how fast the stripper accelerates. $k$ is assumed to be the time needed for shear waves generated from the impact to be reflected from the plate edge and propagate back to the impact site, i.e., $k = \sqrt{2}\phi/C_s$, where $C_s$ is shear wave velocity in the stripper plate material.

Substituting Eqs.(2.9), (2.10) and (2.12) into Eq.(2.11), the relation between the separation time and initial velocity is found to be

$$H_0 + \left(\frac{\sqrt{3}}{\pi d \sigma_s} m_c (1 - q^2) v_0^2\right)^{\frac{1}{2}} = (1 - q) v_0 t_s + \frac{\sqrt{2}\phi q v_0}{C_s}\left(1 - \exp\left(-\frac{t_s C_s}{\sqrt{2}\phi}\right)\right), \tag{2.13}$$

where $q = (\frac{m_s}{m_s + m_{sp}})^{\frac{1}{2}}$.

When $t_s$ is equal to $\sqrt{2}\phi/C_s$, Eq.(2.13) gives the relation between impact velocity and the smallest diameter of stripper plate. The relation between $\phi$ and $v_0$ is given in Figure 2.9 in which the curve is calculated under $m_s = 0.1$ kg, $m_c = 0.015$ kg, $C_s = 3.2$ km/s for mild steel, $\sigma_s = 0.4$ GPa for 2024 Al (*Marsh* [1980]), $H_0 = 0.008$ m, and $m_{sp} = 123\ \phi^2$ kg for mild steel (steel density is 7850 kg/m$^3$ and stripper plate thickness is 0.02 m). If stripper plate diameter is below the curve, waves reflected from the stripper plate edge will interfere with the projectile separation. If stripper plate diameter is above the curve, the waves do not interfere with the separation. From Figure 2.9, the stripper plate diameter is chosen to be 0.14 m when initial velocity is higher than 200 m/s and 0.2 m for initial velocities below 200 m/s.

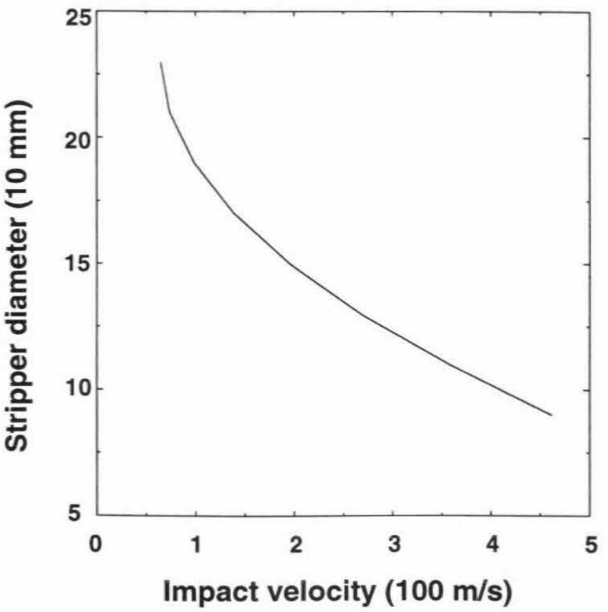

Figure 2.9: Stripper plate versus impact velocity.

## 2.3 Detection and recording system

The last issue related to the measurement method is how to detect the projectile position during the penetration processes. A stationary laser beam is used to detect the position of a projectile with black and white stripes during penetration into target materials. The system used by *Anderson et al.* [1996] to measure free fall projectile velocity in the range of 0-20 m/s is not applicable for penetration depth time history measurement because the system has a spatial uncertainty of 5 mm and time resolution of 0-10 kHz. In order to detect all stripes passing over a laser beam with high enough time and spatial resolution, the detection system must collect reflected laser energy very efficiently. Three major factors that affect laser energy collection are (1) since the bar-coded projectile surface is finished by taking a final light cut on the paint, laser energy reflected from the surface is not spatially uniform, (2) because of possible misalignment of projectile trajectory from assumed position, the direction of maximum reflected laser energy may vary with time during penetration, (3) dust particles from impact and burned propellant products may obscure both the incident and reflected laser beams if they enter the bar-reader. Based on the above conditions, a VISAR probe (FOP-1000, Valyn International) was chosen to focus the incident laser beam on the projectile surface and also collect reflected laser energy (Figure 2.10). The VISAR probe has a small focus diameter ($< 0.6$ mm) and long field depth ($\sim 12$ mm), and collects reflected energy from diffusive surfaces efficiently when the probe is well aligned with the target surface. However, in the present experiments, the projectile surface is not a good diffusive surface, and possible misalignment exists. In order to overcome this problem, the designed system includes (1) a well protected and enclosed optical path (Figures 2.2 and 2.10), with the only open optical path ($\sim 5$ mm) between the projectile surface and the surface of a hollow cylinder that the projectiles pass through, (2) laser trap #1 is used to reflect part of the laser energy from misaligned and/or non-diffusive surfaces back to the probe, (3) laser trap #2 is designed to reflect part of the laser energy focused outside laser-out plastic fiber back to the fiber, (4) original 1 mm diameter plastic fiber is replaced with 2 mm diameter plastic fiber (DuPont) to increase laser collection efficiency (in principle, one can replace it with even larger diameter plastic fibers. However, the low flexibility of plastic fibers with diameter larger than 2 mm results in installation difficulties), and (5) a rubber screen at the end of the hollow cylinder near the impact site is used to block dust particles from entering the hollow cylinder (Figure 2.1).

During penetration, projectile velocity varies from the initial impact velocity ($10^2$ m/s) to very low velocity (10 m/s). This large velocity change requires the recording system to have a very wide bandwidth. Assuming that initial projectile velocity ranges from 100 to 400 m/s, the time duration between two adjacent reflected laser energy peaks will vary from 2.5 to 10 $\mu$s during initial penetration. When penetration approaches final depth, projectile velocity is $\sim 30$ m/s, and then the time duration is $\sim 35\ \mu s$. In general, at least 12 sample points per cycle are needed to record the laser energy profile accurately with a digital oscilloscope or a transient recorder. This means that the sampling rate must be at least 20 MHz. At the same time, the penetration process lasts about $10^2$ $\mu$s. Therefore, the detection system must at least have a bandwidth of 10 kHz to 20 MHz. Based on the above estimation, two different

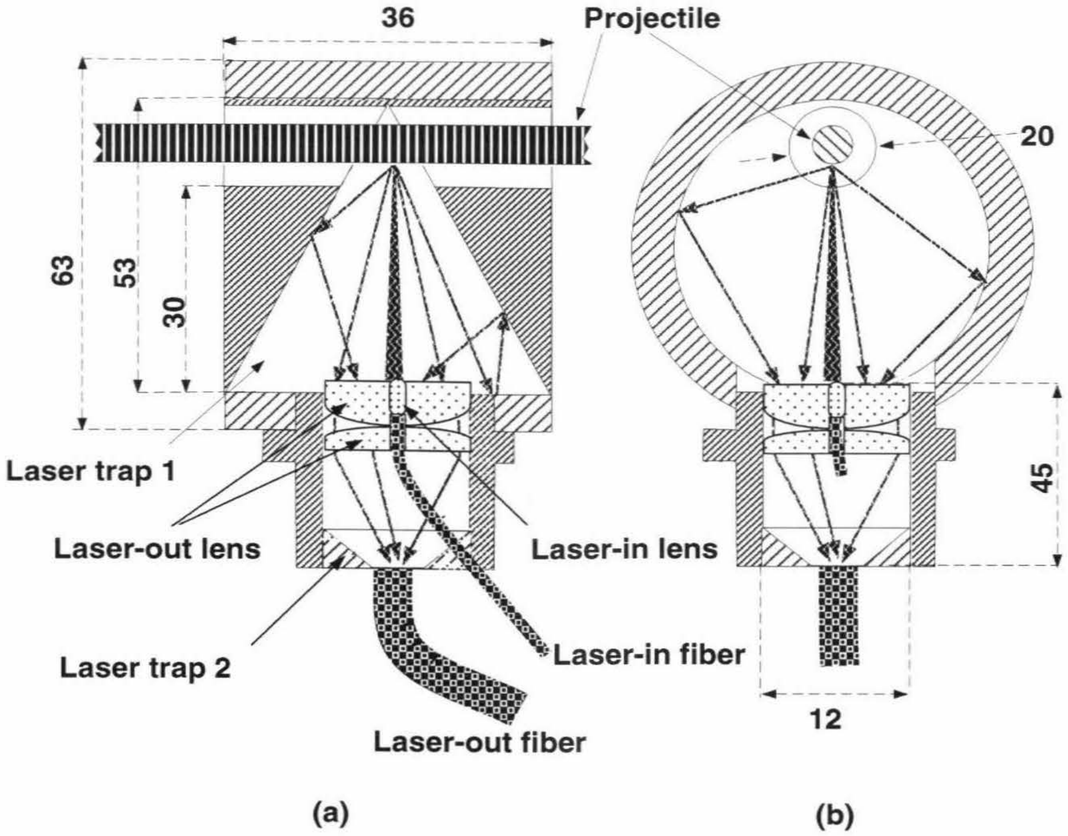

Figure 2.10: Schematic of bar-reader. (a) is side-section view and (b) is end-section view. All dimensions are in mm.

kinds of photodiodes with built-in amplifiers are chosen. One has the bandwidth from 10 kHz to 80 MHz and the other from 4 kHz to 5 MHz. The detail information on the two photodiodes are given in the caption of Figure 2.2.

## 2.4 Error analysis

The intrinsic error of the present method comes from (1) stripe width uncertainty, (2) the rigid body assumption, and (3) the uncertainty of the penetration start and stop positions. The intrinsic errors are further divided into time and spatial error. The intrinsic time error is time uncertainty between the recorded adjacent laser energy peaks during penetration. The spatial error is the uncertainty of penetration depth determined from the present method.

### 2.4.1 Intrinsic time error during penetration

The intrinsic time error comes from stripe width uncertainty and the rigid body assumption. Their contributions are estimated as follows.

1. Error from stripe width uncertainty

   The boundary between black and white stripes does not necessarily have a sharp and straight edge due to the machining method adopted, but instead it could be diffuse and wavy. This results in timing error of

   $$\delta t_1 = \frac{L_{wb}}{v}, \tag{2.14}$$

   where $L_{wb}$ is average boundary width and $v$ is projectile velocity.

2. Error from the rigid body assumption

   Elastic waves generated from the initial impact reverberate in the projectile body. This wave reverberation changes the effective stripe width due to strain associated with elastic waves. Assuming that the average stress amplitude of finite elastic wave is $\sigma_e^a$, the particle velocity, $u_e^a$, related to the elastic wave is

   $$u_e^a = \frac{\sigma_e^a}{\rho_p C_e}, \tag{2.15}$$

   where $\rho_p$ and $C_e$ are projectile material density and longitudinal elastic wave velocity. The maximum width change of one pair of black and white stripes induced by the elastic wave is therefore

   $$\delta L = (L_w + L_b)\frac{u_e^a}{C_e}. \tag{2.16}$$

The time error, $\delta t_2$, related to the width change is

$$\delta t_2 = \frac{\delta L}{v} = \frac{(L_w + L_b)}{v}\frac{u_e^a}{C_e}. \tag{2.17}$$

Therefore, the possible maximum time error during the penetration process is given by a summation of Eqs. (2.14) and (2.17) as

$$\delta t = \delta t_1 + \delta t_2. \tag{2.18}$$

Then, the relative intrinsic time error, $Error$, is

$$Error = \frac{100\delta t}{(L_b + L_w)/v} = 100(\pm\frac{u_e^a}{C_e} \pm \frac{L_{wb}}{L_w + L_b}). \tag{2.19}$$

Using Eq. (2.19), the time error just after impact can be estimated. For the experiments conducted, the typical values of $L_w + L_b$, $L_{wb}$ and $v$ are 1 mm, 0.01 mm and 200 m/s, respectively. $C_e$ is 5.3 km/s for 4140 steel(*Marsh* [1980]). Elastic wave amplitude is taken to be approximately 50% of the peak pressure just after impact, $\sigma_e^a = 0.4$ GPa since the measurement point is far away from the impact site (~20 mm). From Eq. (2.19), the maximum relative error is estimated to be ~ 3 %. Because the effect of elastic waves can be ignored long after impact, the maximum relative error long after impact is calculated to be also ~ 3%.

### 2.4.2 Penetration depth uncertainty

Although a trigger pin is used to give the exact time at which a projectile starts to penetrate into a target, the projectile position is not determined precisely because of the finite stripe width (the same thing is true for penetration stop point). Therefore, the maximum uncertainty of the position at which a projectile starts to penetrate and stops penetrating is half of the stripe width. The width is either black or white stripe width depending on where the laser beam hits at that particular moment. Therefore, the maximum uncertainty of the penetration start and stop point ranges from 0.15 to 0.35 mm.

## 2.5 Experimental validation of present method

Using the designed systems and 40 mm gas/powder gun at Caltech, a series of experiments were conducted on G-mixture mortar targets. Typical reflected laser energy variation recorded is shown in Figure 2.11 (experimental data on penetration depth time history are shown in Figure 3.22). Experimental results demonstrate that the systems operated successfully.

The validity of the experimental results is demonstrated by the following facts:

1. Final penetration depth

   Table 2.1 compares the final penetration depth determined by the penetration depth-time measurement with that measured from the recovered targets. The two depths are in good agreement, clearly demonstrating that the present method gives the whole penetration depth time history.

2. Initial projectile velocity

   The initial projectile velocity was also determined using laser obstruction and X-ray-method (*Ahrens et al.* [1971]). Because projectiles passed through the bar-reader before they started to penetrate into targets, the initial impact velocity after projectile-sabot separation was also measured by the present method. The good agreement among the three measured velocities (Table 2.2) shows that the separation system does not affect projectile velocity.

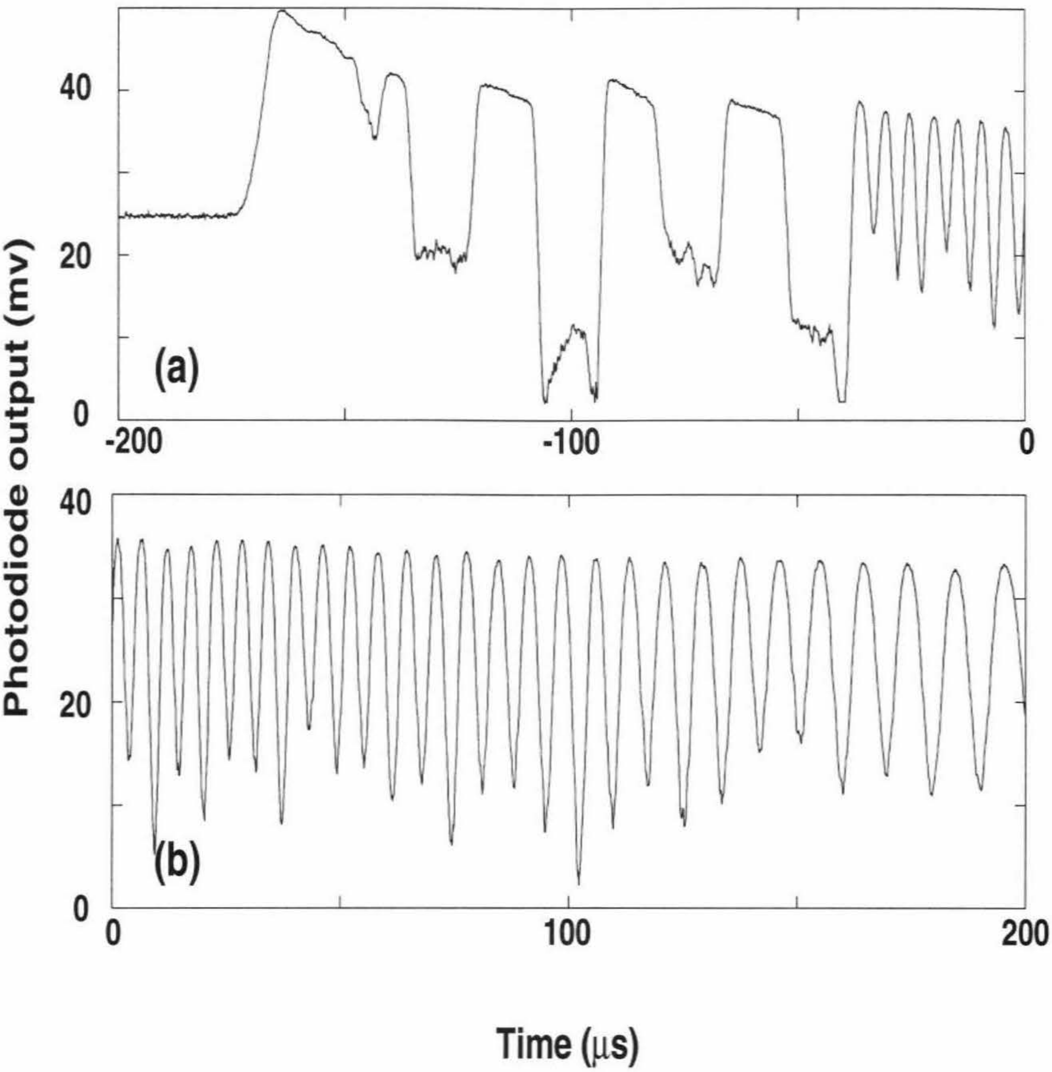
Photodiode output (mv)
Time (μs)
(a)
(b)
0
20
40
-200
-100
0
100
200

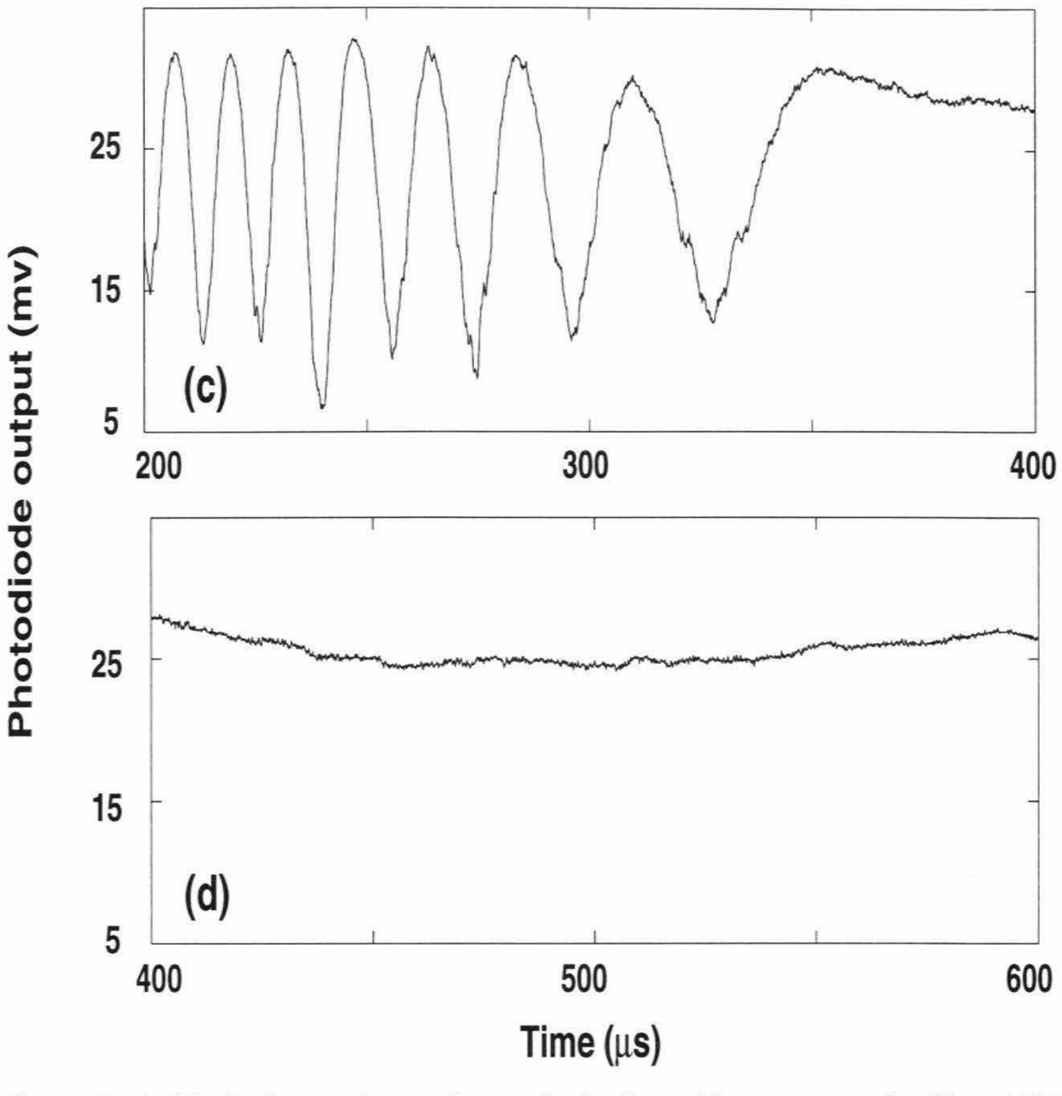

Figure 2.11: Typical experimental record of reflected laser energy for Shot 1033. Time reference point 0 is from trigger pin attached to impact surface and represents the start point of penetration. Figure (a) is photodiode output before projectile impacted target. The several wide fringes in Figure (a) are results of detecting the wider stripes near projectile tip. Figure (b) gives the record in the first 200 $\mu$s after the impact. Figures (c) and (d) show records from 200 to 400, 400 to 600 $\mu$s, respectively after the impact. Starting at $t = 350\mu$s, it appears that the projectile did not move at all.

Table 2.1: Comparison between the final depths from the method and recovered targets.

| Shot # | P38 | 1017 | 1033 | 1034 |
|---|---|---|---|---|
| Depth$^{(1)}$ (mm) | 30.2±0.5 | 41.4 ±1.0 | 40.5 ± 0.6 | 65.7 ± 1.0 |
| Depth$^{(2)}$ (mm) | 30.4±0.3 | 42.2 ± 0.3 | 40.3 ± 0.7 | 65.2 ± 0.7 |

Depth$^{(1)}$ was measured in recovered targets. Error of Depth$^{(1)}$ was determined from smoothness of target surface. Depth$^{(2)}$ was determined from present method.

Table 2.2: Comparison among the three velocities measured.

| Shot # | P38 | 1017 | 1033 | 1034 | 1035 | 1036 |
|---|---|---|---|---|---|---|
| V$^{(1)}$ | 178.0 ±0.1 | 272.5 ± 0.3 | 213.3 ± 0.5 | 321.4 ± 3.0 | 313.1±1.9 | 272.6 ±1.9 |
| V$^{(2)}$ | 172.2±1.0 | 265.7± 2.3 | 215.4 ± 0.7 | 320.5 ± 2.1 | 309 | 271 |
| V$^{(3)}$ | 176.3 | 269.4 | | | | |

V$^{(1)}$ (m/s) is projectile velocity obtained from present method. V$^{(2)}$ (m/s) is projectile velocity given by laser obstruction method. Error is determined from the difference between the two velocities that were given by three laser beams used. Only one velocity was obtained for Shots 1035 and 1036. V$^{(3)}$ (m/s) is projectile velocity given by X-ray method that only provided the velocity for Shots P38 and 1017.

## 2.6 Conclusions

A new method has been developed to measure the penetration depth time history of projectiles into brittle materials under the rigid body assumption. This method includes projectile design, sabot-projectile separation, and detection and recording systems. Error analysis shows that this method has relatively low intrinsic error. The maximum intrinsic time error is ∼ 3%. The penetration depth error varies from 0.3 to 0.7 mm.

This method has been used to measure penetration depth time history of 10 or 15 mm diameter, 100 or 150 mm long 4140 steel projectiles penetrating 20 to 70 mm into mortar targets. The comparisons of the experimental data from this method with the data from other methods validate this method. This method has been adopted by the Champollion Mission to measure the penetration depth time history of the anchor.

# Chapter 3 Experimental results and empirical scaling relations

Using the measurement method described in Chapter 2 and the Caltech 40 mm gas/powder gun, a series of penetration experiments have been conducted. The depth-time histories of rigid body penetration into G-mixture mortar in the velocity range of 150 to 350 m/s were obtained using projectiles with a diameter of 10 or 15 mm and a length of 100 or 150 mm. Damage inside the recovered targets and on the recovered projectile surface was characterized. In the first section of this chapter, the target material response under uniaxial strain impact loading and the compressive strength of the target material are discussed based on present results and previous data (*Read and Maiden* [1971], *Grady* [1995], *Hall et al.* [1997], *Kipp et al.* [1997], *Wahlstrom* [1998], and *Li and Huang* [1998]). In the second section, target and projectile damage observed on recovered targets and projectiles is described and discussed. In the last section, several penetration scaling relations are deduced based on the present penetration data.

## 3.1 Characterization of projectile and target materials

### 3.1.1 Projectile material

The projectile material is heat-treated 4140 steel with $R_c = 45$ (Rockwell C). Physical properties and composition of 4140 steel are listed in Tables 3.1 and 3.2 (*Boyer and Gall* [1985]), respectively.

Table 3.1: AISI 4140 steel physical properties.

| Density ($g/cm^3$) | Tensile Strength (GPa) | Compressive Strength (GPa) |
|---|---|---|
| 7.85 | 0.92 | 1.50 |
| E (GPa) | K (GPa) | G (GPa) |
| 205 | 140 | 80 |

Table 3.2: AISI 4140 steel composition.

| Component | Wt.% | Component | Wt. % |
|---|---|---|---|
| C | 0.38-0.43 | Cr | 0.95 |
| Mn | 0.93 | Mo | 0.2 |
| P | <0.035 | S | <0.04 |
| Si | 0.23 | Fe | 97 |

### 3.1.2 Target material

The target material is G-mixture mortar provided by the U.S. Air Force at Tyndall (AFB), Florida under the direction of Dr. David Jerome (*Wahlstrom* [1998]). The mortar targets were 500 mm in diameter and 400/600 mm in length. All the targets were poured on the 21st and 29th of May, 1997. The present experiments were started on the target seven months later. In order to determine initial properties of the mortar, several cylinders with 150 mm diameter and 300 mm length were also made at the same time. The aggregate size distribution of the mortar was provided by the U.S. Air Force (*Wahlstrom* [1998]) (Table 3.3).

#### Ambient condition properties

The elastic moduli of the mortar were determined by measuring ultrasonic wave velocities using 1 MHz P- and S-wave transducers (Model V153 for S-wave and Model V103 for P-wave, Panametrics, Inc.). The sample preparation procedures are described in detail by *Rubin and Ahrens* [1991]. The wave velocities measured are listed in Table

Table 3.3: Aggregate size distribution in G-mixture mortar (*Wahlstrom* [1998]).

| Sieve | Maximum Diameter (mm) | Weight Percentage (%) |
|---|---|---|
| #8 | 2.4 | 0.0 |
| #16 | 1.19 | 10.1 |
| #30 | 0.59 | 30.4 |
| #50 | 0.30 | 36.1 |
| #100 | 0.15 | 21.7 |

Weight percentage is defined as the ratio of aggregate weight left over on sieve to total aggregate weight. #8 sieve was used first, and then #16 was used for aggregate through #8 sieve, and so on.

3.4. The elastic properties of the mortar are calculated from

$$\nu = \frac{2 - (\frac{C_p}{C_s})^2}{2(1 - (\frac{C_p}{C_s})^2)}, \tag{3.1}$$

$$G = \rho_0 C_s^2, \tag{3.2}$$

$$E = 2(1 + \nu)\rho_0 C_s^2, \tag{3.3}$$

$$K = \frac{2G}{3}\frac{1 + \nu}{1 - \nu}, \tag{3.4}$$

and

$$C_b = \sqrt{\frac{K}{\rho_0}}, \tag{3.5}$$

where $C_p$, $C_s$ and $C_b$ are P-, S- and bulk wave velocities, respectively (*Timoshenko and Goodier* [1970]), $\rho_0$ is initial density, $G$, $E$, $K$ and $\nu$ are shear, Young's and bulk moduli and the Poisson's ratio, respectively.

### Mortar response to impact loading

The behaviors of concrete and mortar (*Read and Maiden* [1971], *Grady* [1995], *Hall et al.* [1997], and *Kipp et al.* [1997]) are very complicated because of multi-phase

Table 3.4: Ultrasonic velocity and elastic moduli of the mortar.

| $\rho_0$ (g/cm$^3$) | $C_p$(km/s) | $C_s$( km/s) | $C_b$ (km/s) | $\nu$ |
|---|---|---|---|---|
| 1.95±0.02 | 3.89±0.05 | 2.22±0.04 | 2.96±0.03 | 0.258±0.004 |
| $E$ (GPa) | $G$ (GPa) | $K$ (GPa) | $\sigma_f$ ( GPa) | |
| 24.4±1.1 | 9.7±0.4 | 16.8±0.5 | 0.044 | |

$\sigma_f$ is unconfined compressive strength at a strain rate of $2.2 \times 10^{-6}$ s$^{-1}$ (*Wahlstrom* [1998]). All samples used for compressive strength and velocity measurements were poured together.

Table 3.5: Summary of shock compression data on concrete and mortar.

| Material | Density (g/cm$^3$) | $C_e$ (km/s) | $\sigma_{hel}$ (GPa) | $C_0$ (km/s) | $C_1$ | $C_2$ (s/km) | Note |
|---|---|---|---|---|---|---|---|
| Concrete$^{(1)}$ | 2.19 | 4.2 | 0.05 | 2.25 | -3.33 | 0.0 | $v$ <0.15 km/s |
| | | | | 0.9 | 5.17 | -2.22 | $0.15 < v < 1.3$ km/s |
| Concrete$^{(2)}$ | 2.26 | 5.0-61.8 $v$ | | | | | $v$<0.12 km/s |
| | | | | 0.551 | 4.52 | 0.0 | $0.12 < v < 0.64$ km/s |
| | | | | 2.235 | 1.745 | 0.0 | $v > 0.64$ km/s |
| MJ-2 grout$^{(3)}$ | 1.97 | | | 2.4 | 1.6 | 0.0 | $0.5 < v < 2$ km/s |
| | | | | 2.4 | 1.36 | 0.0 | $2 < v < 4$ km/s |
| G-mixture mortar$^{(4)}$ | 1.96 | 4.26 | 0.14 | | | | |

$C_e$: Hugoniot elastic wave velocity. $\sigma_{hel}$: Hugoniot elastic limit. $C_0, C_1$ and $C_2$ are constants in the relation between shock wave velocity, $D$, and particle wave velocity, $v$, e.g., $D=C_0+C_1v+C_2v^2$. (1) *Read and Maiden* [1971]. (2) *Grady* [1995]. (3) *Grady* [1998] and (4) this work.

composition and porosity in these materials. The response of concrete and mortar to uniaxial strain shock loading (*Read and Maiden* [1971] and *Grady* [1995]) is charactized by three stages:

1. Elastic stage: Non-dispersive elastic waves arrive first with amplitudes as low as 50 MPa (*Read and Maiden* [1971]). Such elastic waves do not collapse cavities in concrete and mortar. These are followed by dispersive elastic waves which collapse cavities, and as a result, wave velocities decrease rapidly with particle velocity(*Read and Maiden* [1971] and *Grady* [1995]).

2. Shock compacting stage: The slope, $C_1$, in the $D-v$ relation ($D$ and $v$ are shock wave and particle velocities, respectively) is large (e.g., 5.17 and 4.52 in Table 3.5) , which suggests that large deformation takes place (*Hall et al.* [1997]). The value of $C_1 > 2$ indicates an anomalously large value of $(dK/dP)_s$ which is applicable to materials that undergo a phase change or irrversible compaction.

3. Normal shock stage: The slope of the $D - v$ relation is in the range of 1 to 2.

The shock loading data for several concretes and mortars listed in Table 3.5 show that there is no substantial difference in low pressure range (shock wave peak pressure $< 3$ GPa)(*Grady* [1995]). In order to find out which concrete's or mortar's Hugoniot relation can be used to describe approximately the G-mixture mortar, two uniaxial strain shock loading experiments were conducted using embedded manganin gauges to measure shock wave profiles at different locations from impact surface in the stress range of interest. The 40 mm gas/powder gun at Caltech was employed to conduct the present tests (details of the measurement method are described in Part II). The experimental set-up is given in Figure 3.1. Figure 3.2 shows stress profiles from the two experiments. The experimental parameters and results are listed in Table 3.6. Based on the recorded stress wave profiles in the mortar, the response of the mortar under uniaxial strain impact loading is divided into two stages:

1. Elastic deformation statge: The elastic wave has an amplitude of $0.137 \pm 0.004$ (GPa) and a wave velocity of $4.26 \pm 0.06$ km/s. Up to peak shock stress of $\sim$

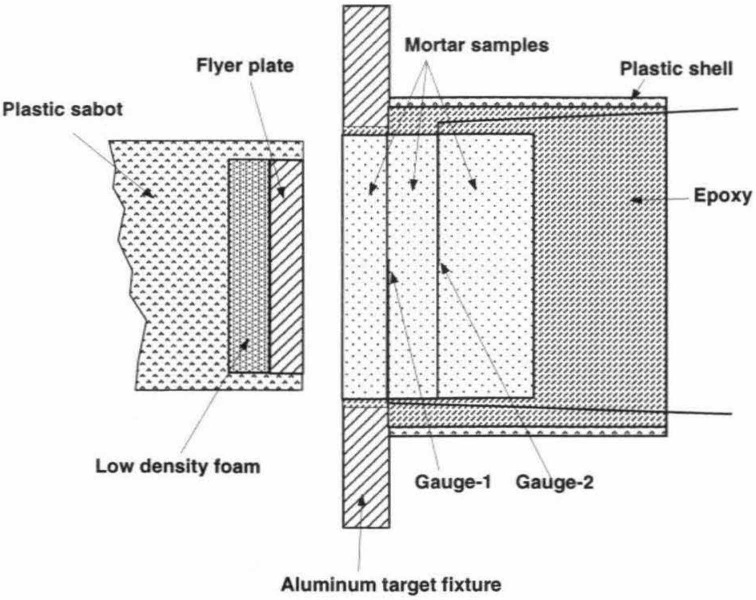

Figure 3.1: Configuration for stress wave profile experiments. Manganin gauge used is Mn4-50-EK (Dynasen, Inc.), power supply for manganin gauges is CK2 from Dynasen, Inc.

1 GPa, a ramp-wave forms with an amplitude of 0.1 ± 0.01 GPa.

2. Plastic deformation stage: Under the experimental conditions, the shock wave propagates at a velocity (~1.8 km/s) that is below initial bulk wave velocity (~2.96 km/s) and also with a rise time of 1.2 to 1.6 $\mu$s upon propagation through a ~5 to 10 mm thick sample (all these results reflect large compression in the mortar, i.e., densification). These characteristics were observed in previous work on concrete and mortar (*Read and Maiden* [1971] and *Grady* [1995]). The relation of *Read and Maiden* [1971] is found to yield shock wave velocity that is in good agreement with the present measurements (Table 3.5). Therefore, we assumed that the Hugoniot relation of *Read and Maiden* [1971] approximately describes the shock wave eqaution of state of the G-mixture mortar.

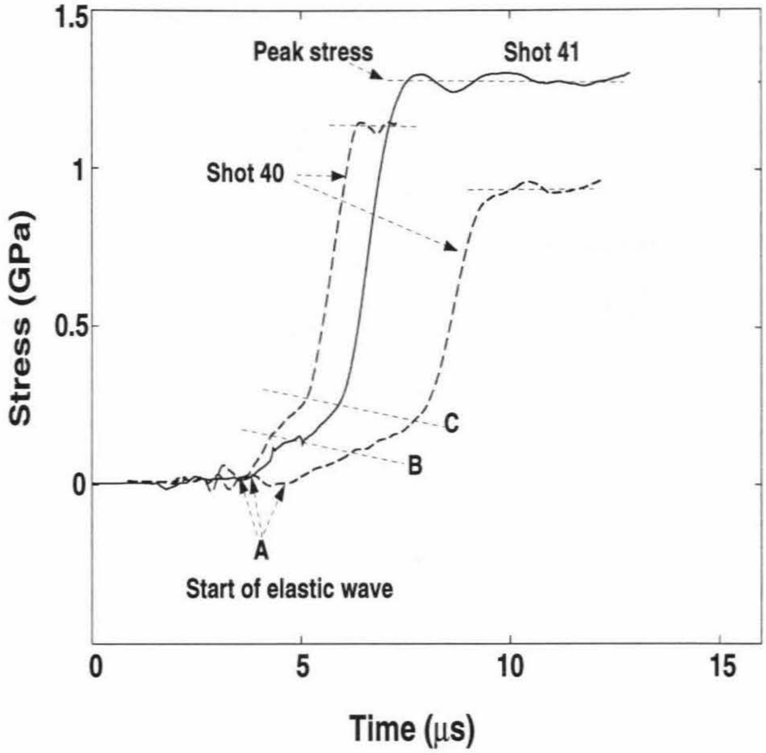

Figure 3.2: Stress wave profiles in G-mixture mortar. Point A to Point B: elastic wave. Point B to Point C: dispersive elastic wave (ramp wave). Beyond Point C: shock wave. From wave profiles, we also see the decay of elastic, ramp and shock wave with propagation distance.

Table 3.6: Uniaxial strain impact data of G-mixture mortar.

| Shot Num. | $V_p$ (m/s) | Gauge Num. | $h_g$ (mm) | $C_e$ (km/s) | $\sigma_{hel}$ (GPa) | $\sigma_r$ (GPa) | $\sigma_p$ (GPa) | $D$ (km/s) |
|---|---|---|---|---|---|---|---|---|
| P40 | 211 | 1 | 5.2 | 4.32 | 0.141 | 0.244 | 1.14 | 1.8 |
| | | 2 | 10.54 | 4.32 | 0.134 | 0.222 | 0.94 | 1.8 |
| P41 | 227 | 2 | 6.67 | 4.2 | 0.136 | 0.245 | 1.26 | 1.75 |

$V_p$ is flyer velocity. Flyer material is tungsten with initial density 19.19 g/cm$^3$. The flyer dimensions are 32 mm diameter and 4 mm thickness. $h_g$ is distance of gauge from impact surface. $\sigma_r$ is ramp wave peak amplitude and $\sigma_p$ is shock wave peak pressure.

### Compressive strength

Material compressive strength is one of the important parameters for penetration. Material strength (compressive and tensile) depends on strain rate. *Li and Huang* [1998] found that mortar compressive strength increases dramatically with strain rate. Their experimental data taken with a testing machine (one-dimensional stress) show that the ratio of mortar compressive strength at a strain rate of $10^{-2}$/s, to initial strength at a strain rate of $10^{-7}$/s, is approximately 1.9 (Figure 3.3). Based on previous work on concrete and mortar(*Ross et al.* [1989] ), a best fit to the low-strain-rate data of *Li and Huang* [1998] yields

$$\frac{\sigma_f}{\sigma_f^0} = \exp(0.095(\log(\frac{\dot{\varepsilon}}{\dot{\varepsilon}_0}))^{1.14}), \tag{3.6}$$

where $\sigma_f^0$ is compressive strength at strain rate $\dot{\varepsilon}_0 = 2.8 \times 10^{-7}$/s.

From the uniaxial strain shock loading experiments, yield stress is also deduced using (*Ahrens* [1993])

$$\sigma_y = \frac{\sigma_{hel}}{\frac{K}{2G} + \frac{2}{3}}. \tag{3.7}$$

Strain rate, $\dot{\varepsilon}$, at the Hugoniot elastic limit (HEL) is estimated using

$$\dot{\varepsilon} \sim \frac{v_e}{C_e \delta t}, \tag{3.8}$$

where $v_e$ is particle velocity at the HEL and $\delta t$ is elastic wave rise time. Based on the wave profiles shown in Figure 3.2 and elastic moduli given in Table 3.4, $\sigma_y$ is calculated to be 0.09 GPa at $\dot{\varepsilon} \sim 4 \times 10^3$/s. In order to approximately estimate compressive strength under shock loading, the ratio of compressive strength to yield stress under uniaxial stress, $\sim 1.5$ (*Li and Huang* [1998]), is used to deduce compressive strength that is 0.13 GPa. This is about 3 times the compressive strength at the quasi-static strain rate of $2.2 \times 10^{-6}$/s measured by *Wahlstrom* [1998]. The two experimental data on the G-mixture mortar are also plotted in Figure 3.3. Figure 3.3 demonstrates

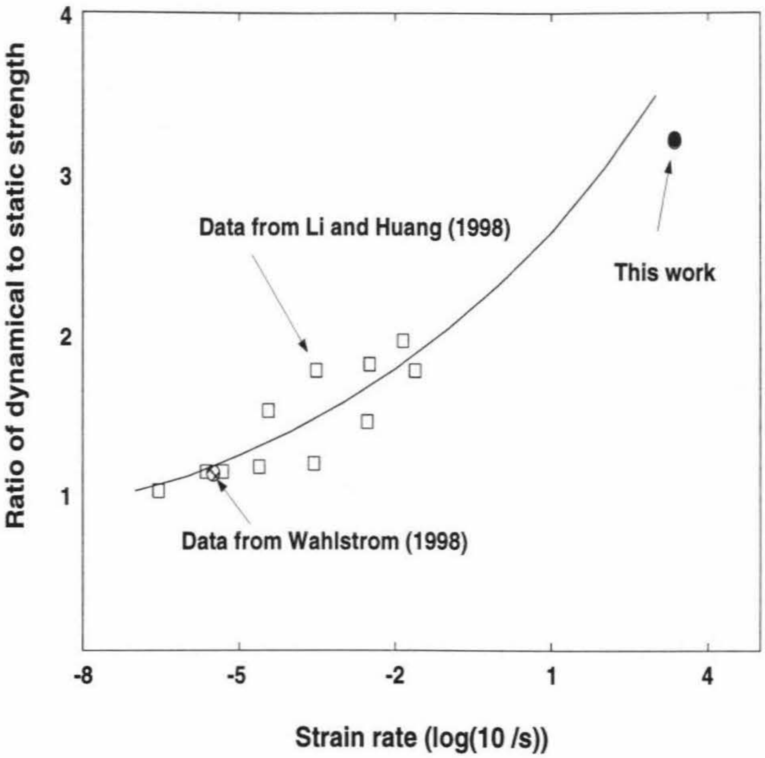

Figure 3.3: Unconfined compressive strength versus strain rate. The solid line is from Eq. (3.6). In order to compare strength at referenced strain rate of $3\times10^{-7}$/s (static), the unconfined compressive strength of G-mixture mortar at $2.8 \times 10^{-7}$ $s^{-1}$ is estimated as $\sigma_f^0 = 0.042$ (GPa) using Eq. (3.6). This value of $\sigma_f^0$ is used as normalization factor for G-mixture mortar.

that the results from the uniaxial strain shock and quasi-static loading experiments are in good correlation with the low strain rate data from *Li and Huang* [1998]. Therefore, the G-mixture compressive strength during penetration can be estimated using Eq.(3.6) because the strain rate during penetration is around the strain rate at the HEL.

## 3.2 Penetration damage characterization

Using the method described in Chapter 2, we conducted a series of projectile penetration tests into the mortar targets using the 40 mm powder gun at Caltech. The

Table 3.7: Penetration experimental parameters.

| Shot # | Projectile length (mm) | Projectile diameter (mm) | Projectile mass (gram) | Projectile velocity (m/s) |
|---|---|---|---|---|
| P38 | 150.0 | 9.96 | 67.5 | 178.0 |
| 1017 | 101.0 | 9.76 | 44.5 | 272.5 |
| 1018 | 150.0 | 10.01 | 64.2 | 505 |
| 1033 | 151.0 | 10.02 | 66.3 | 213.3 |
| 1034 | 151.0 | 9.99 | 66.3 | 321.1 |
| 1035 | 149.8 | 15.03 | 158.6 | 313.1 |
| 1036 | 150.0 | 15.03 | 157.6 | 272.6 |

Measurement error is ± 0.1 mm for projectile length and ±0.01 for projectile diameter, ±0.1 grams for mass. Velocity error is given in Table 2.2.

shape and dimensions of projectiles used in the experiments are shown in Figure 2.6. Table 3.7 lists the experimental parameters. In this section, the features of penetration damage of targets and projectiles are described based on the observations of recovered targets and projectiles. For convenience later in the discussion, crater depth is defined as the depth generated from spallation process near impact surface, and penetration depth is defined as the distance from the impact surface to the final position of the projectile tip (Figure 3.4).

### 3.2.1 Characteristics of recovered targets

For Shots 1017, 1033 and 1034, projectiles were embedded inside recovered targets. For Shots P38, 1018, 1035 and 1036, projectiles bounced off recovered targets because final penetration depth was small for Shots P38 and 1036, and the targets were broken for Shots 1018 and 1035. Figure 3.4 is a general schematic view of a post-shot target with embedded projectile. From the post-shot targets, we observed that penetration damage to target materials away from the penetration path is via two types of cracks, i.e., radial and lateral cracks.

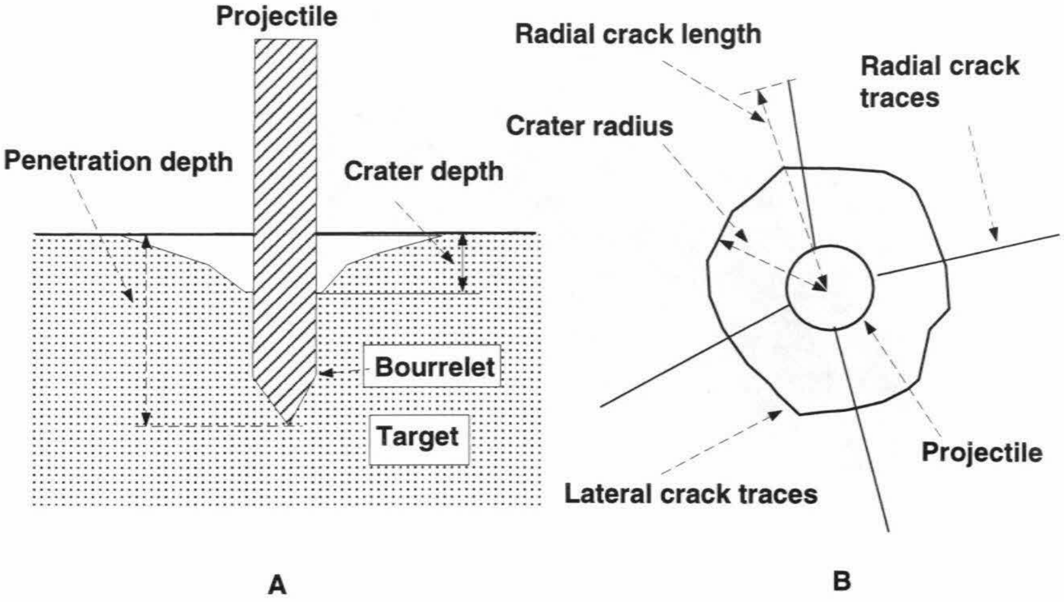

Figure 3.4: Schematic view of postshot targets. A is side-view and B is top-view.

### Radial cracks:

The typical appearance of radial cracks on the impact surface is shown in Figures 3.5 and 3.6. Usually between 4 and 8 radial cracks appeared on the impact surface. These radial cracks with different lengths seem to have propagated along radii from the impact site. Figure 3.7 shows the radial crack length measured on the impact surface as a function of initial projectile energy. Because all crack lengths were measured one or two days after the experiments were conducted, it is possible that the crack length increased after the impact as a result of residual stresses.

Figure 3.7 demonstrates a correlation between radial crack length and initial projectile energy (or penetration depth) for the experiments in which the targets were cratered but intact after impact. For Shots 1018 and 1035, radial cracks propagated both to the lateral target surface and down inside the target. The radial crack length down inside target is much longer than the penetration depth. The recovered target of Shot 1035 is sketched in Figure 3.8. The final penetration depth of Shot 1035 is 78 mm but the height of the radial cracks is $\sim$ 200 mm. The whole target of Shot 1018 was shattered by radial and lateral cracks but the final penetration depth was

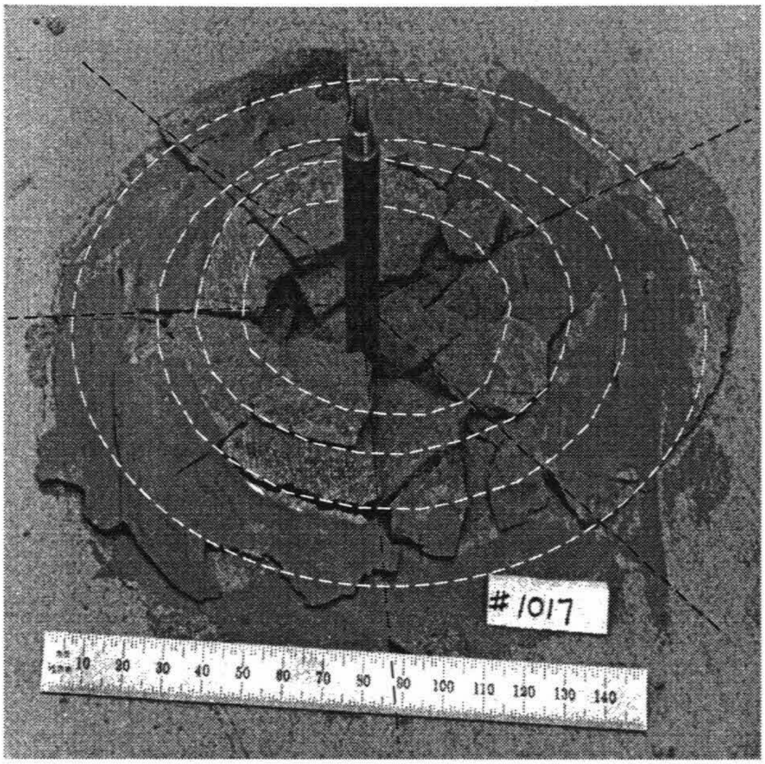

Figure 3.5: Damage pattern of Shot 1017 target. Black lines are trace of radial cracks. White lines are traces of lateral cracks. Spall fragments from the target were reconstructed after the experiment.

only 179 mm. These experimental results indicate that radial cracks propagated at a velocity that is much faster than the penetration velocity during penetration and damaged a much larger region of the target materials than the penetration process itself did. Therefore, it is very important to consider the radial crack damage region in applications of penetrators to space missions.

### Lateral cracks and crater profiles

Figures 3.5 and 3.6 demonstrate that the trace of lateral cracks on the impact surface is close to circular and the spacing of lateral cracks increases away from the impact site. Figure 3.9 shows final crater profiles measured on the recovered targets. The final crater profiles are believed to be formed by the last lateral crack that propagated to impact the free surface during penetration. Crater profiles have several similar

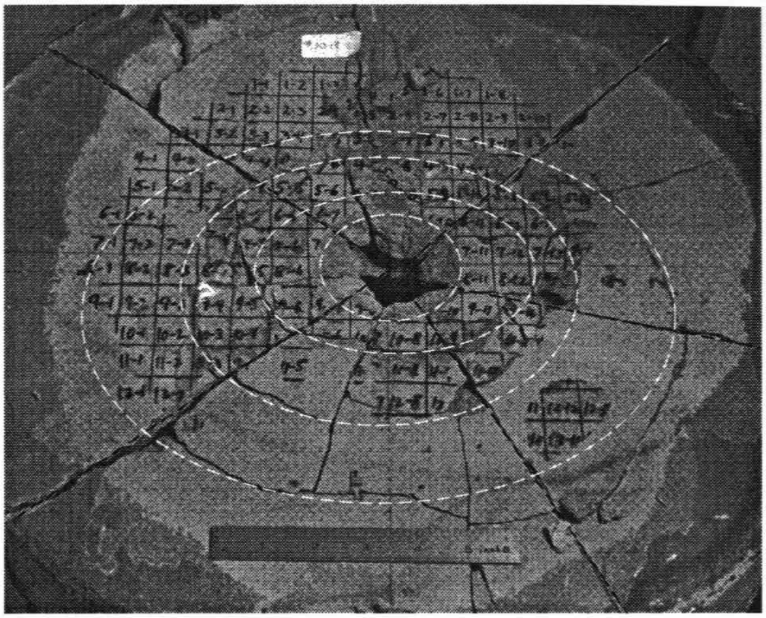

Figure 3.6: Damage pattern of the target for Shot 1018. Black lines are trace of radial cracks. White lines are traces of lateral cracks. Pieces spalled from the target were reconstructed.

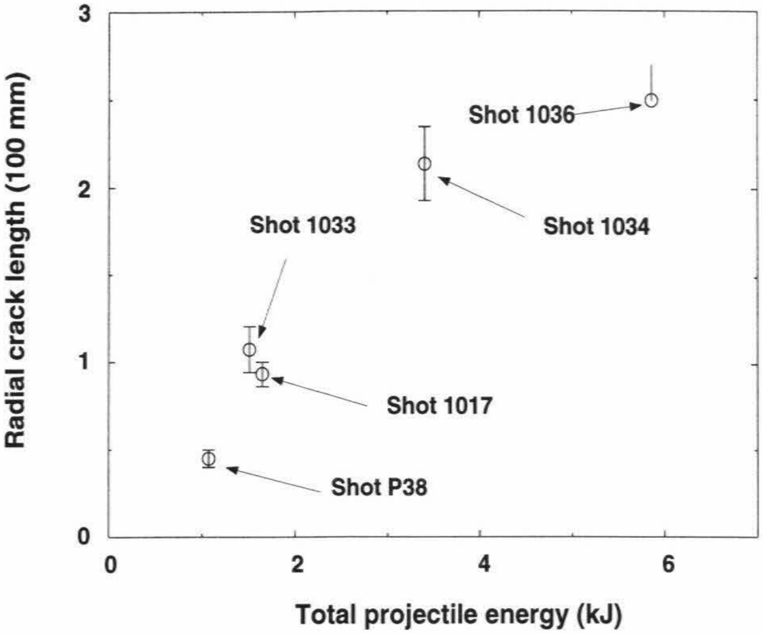

Figure 3.7: Radial crack length versus impact energy. Cracks of Shot 1036 reached the target edge along radial direction on the impact surface, and therefore was probably stopped prematurely.

features:

1. A small plateau appears at the bottom of penetration (Part I in Figure 3.9). The plateau width increases with final penetration depth. This zone may represent mortar comminuted during penetration.

2. The crater wall is falling steep in a region between $\sim 60^o$ and $\sim 20^o$ from the impact surface (Part II in Figure 3.9). The slope of the crater wall in this region increases with final penetration depth.

3. Another plateau or region of low slope on the crater wall is between $\sim 20^o$ and $\sim 16^o$ from the impact surface (Part III in Figure 3.9).

4. The crater wall gets steeper again in a region between $\sim 16^o$ and $\sim 0^o$ from the impact surface (Part IV in Figure 3.9).

5. Figure 3.10 shows the relation between the ratio of crater radius to projectile

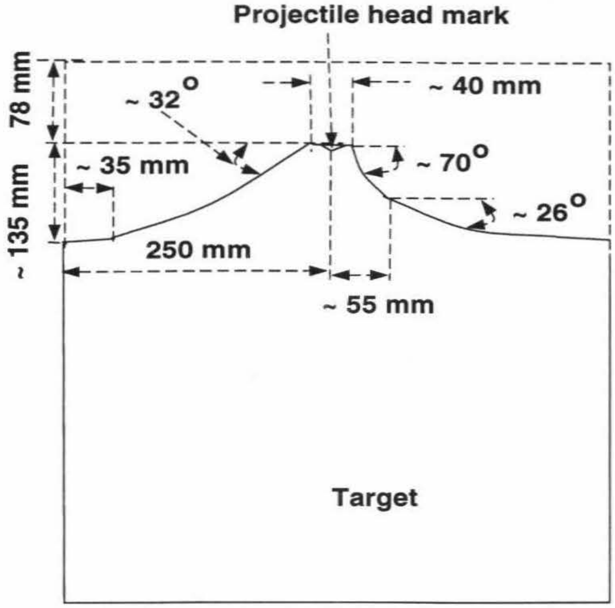

Figure 3.8: Schematic of cross-section of the recovered target for Shot 1035. Features of recovered target are: (1) Unbroken target has a scaled volcano-mountain-like shape, i.e., the center just beneath the penetration is much higher than the surrounding region (the difference between center and edge is ~ 135 mm); (2) There is a relatively smooth and flat annulus region ( ~ 35 mm) next to the lateral surface; (3) The slop near the center is much greater than that near the lateral surface; (4) Radial cracks did not extend into unfractured target.

radius and initial projectile velocity. It seems that the ratio is correlated with impact velocity. Due to the limited data with large error, a linear fit yields

$$\frac{r_c}{R} = (0.129 \pm 0.03)v - (17.2 \pm 7.8), \tag{3.9}$$

where $r_c$ is crater radius and $v$ is initial projectile velocity in m/s.

6. Figure 3.11 shows that the crater depth, $d_c$, is linearly proportional to the initial projectile energy, $E_i$, as

$$d_c = (2.4 \pm 0.6) + (7.27 \pm 0.19)E_i, \tag{3.10}$$

where $d_c$ is in mm and $E_i = mv^2/2$ is in kJ.

Because crater profiles reflect lateral crack propagation during penetration, study of these features would help to understand the formation and propagation of lateral cracks during penetration.

### Damage inside target materials

Post-shot damage conditions induced by projectile penetration provide information on how the target materials respond to penetration. Therefore, it is very useful information towards understanding the penetration process.

In order to investigate post-shot target material damage around the penetrated regime inside recovered targets, the targets for Shots 1017 and P38 were sectioned along the impact axis. Crater and damage patterns from these cross-sections are shown in Figures 3.12 and 3.13. Figure 3.14 schematically shows the damage pattern and some of the tensile (spall) fractures inside the target of Shot 1017. The cross-sections clearly show that there are no visible cracks just in front of the penetrator.

Figure 3.15 gives the micro-structure of mortar near and far away from the bottom of the penetration for Shot P38. It does not show any visible cracks. Figure 3.16

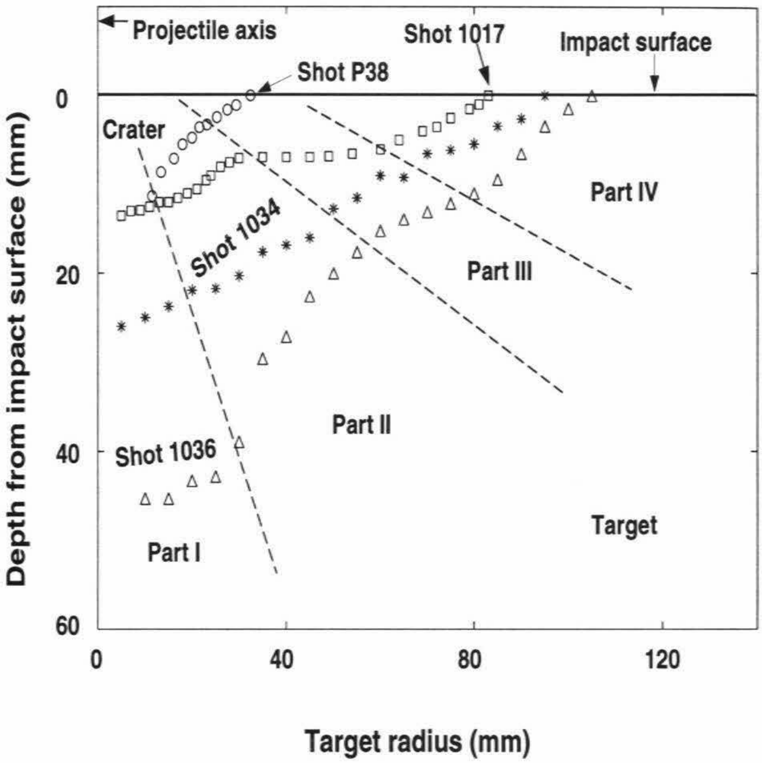

Figure 3.9: Crater profiles of Shots P38, 1017, 1034 and 1036.

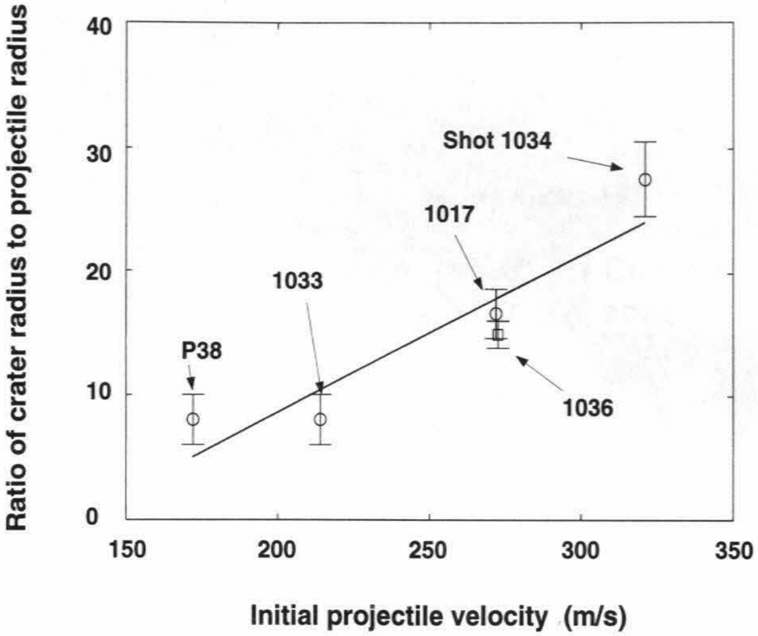

Figure 3.10: Ratio of crater to projectile radius versus initial projectile velocity. Solid line is linear fit (Eq. (3.9)).

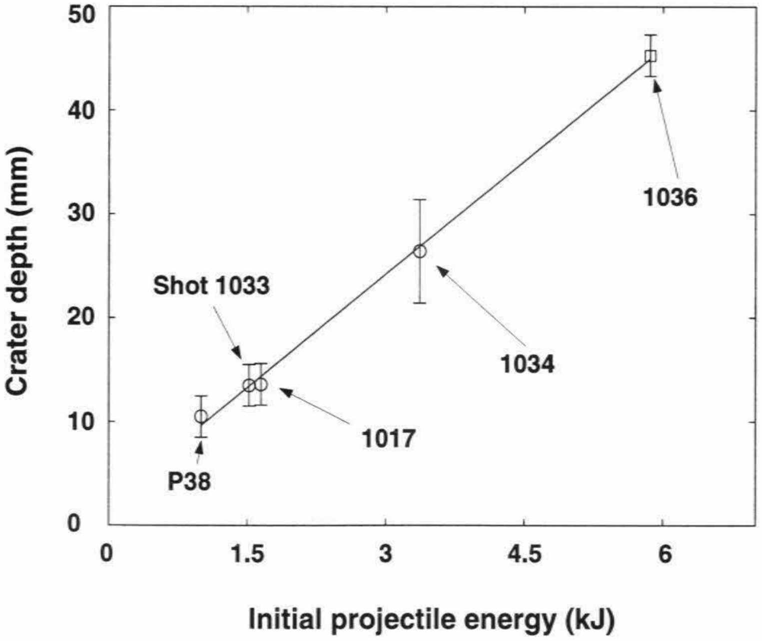

Figure 3.11: Crater depth versus initial projectile energy. Solid line is linear fit (Eq. (3.10)).

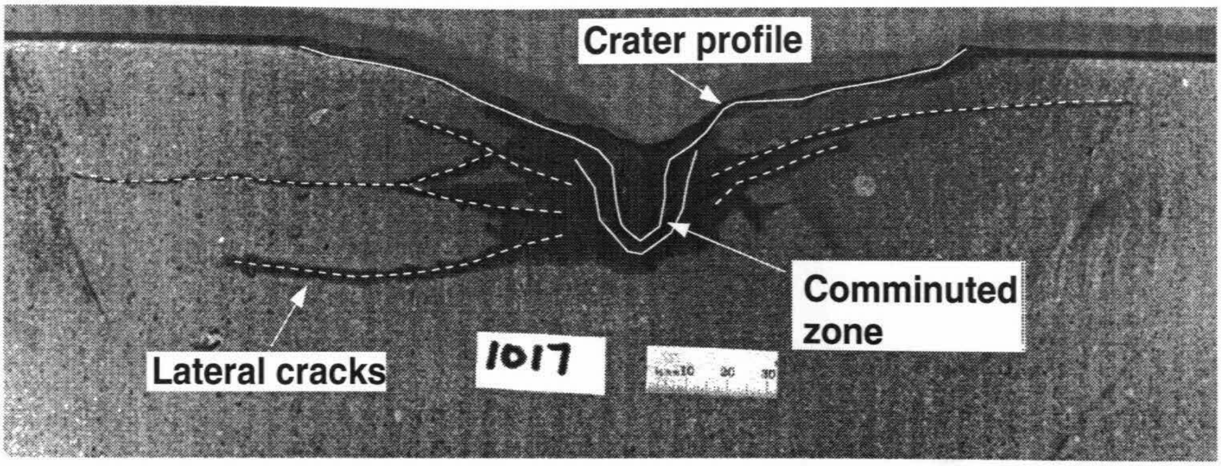

Figure 3.12: Cross-section of the recovered target for Shot 1017. Water was used to increase the contrast between the damaged and undamaged regions.

(a), (b) and (c) show mortar density, and P- and S-wave velocity versus distance from the bottom of the penetration measured on Shot 1017 target, respectively. The density data show that the mortar in front of the penetration was compacted during penetration, and the change in P- and S-wave velocities demonstrates that damage due to compaction occurs in the region. In addition, Figure 3.12 demonstrates that lateral cracks originated only from the region around penetration path, not from the region just in front of the penetration. These results seem to support that damage in front of a penetrator in mortar is via compaction. If compaction was caused by a process with a propagation velocity that is much slower than the crack propagation velocity ($0.4 \sim 0.7\times$ Rayleigh wave velocity), radial and lateral cracks still should be found in front of the penetration. Therefore, the compaction must result from a process that has a velocity faster than the crack propagation velocity.

### 3.2.2 Projectile damage pattern

The damage to the lateral surface of the projectile reflects the degree of contact between projectile and target materials during penetration. Figure 3.17 shows two recovered projectiles. Two parameters related to projectile surface conditions are

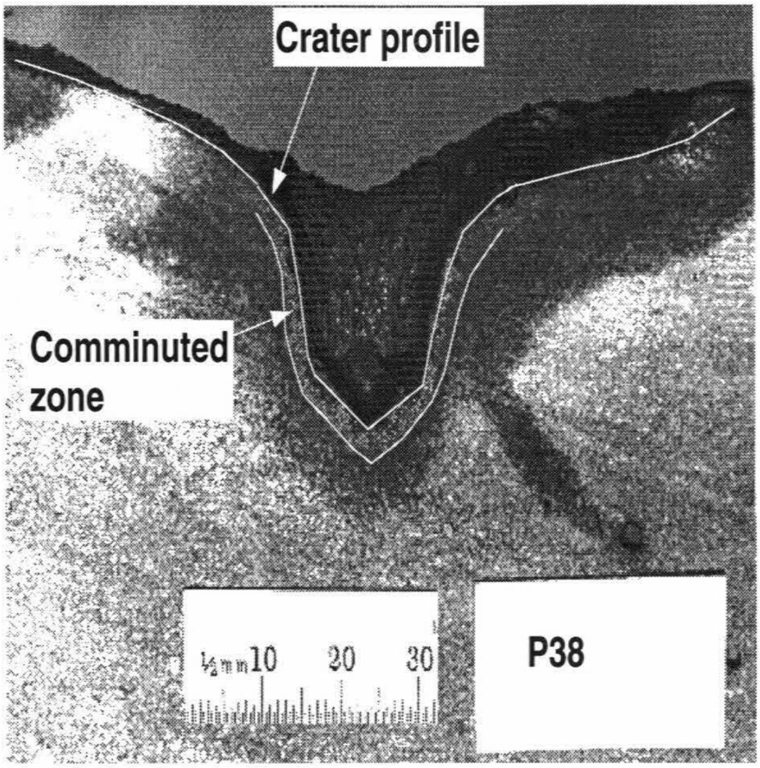

Figure 3.13: Cross-section of recovered target for Shot P38.

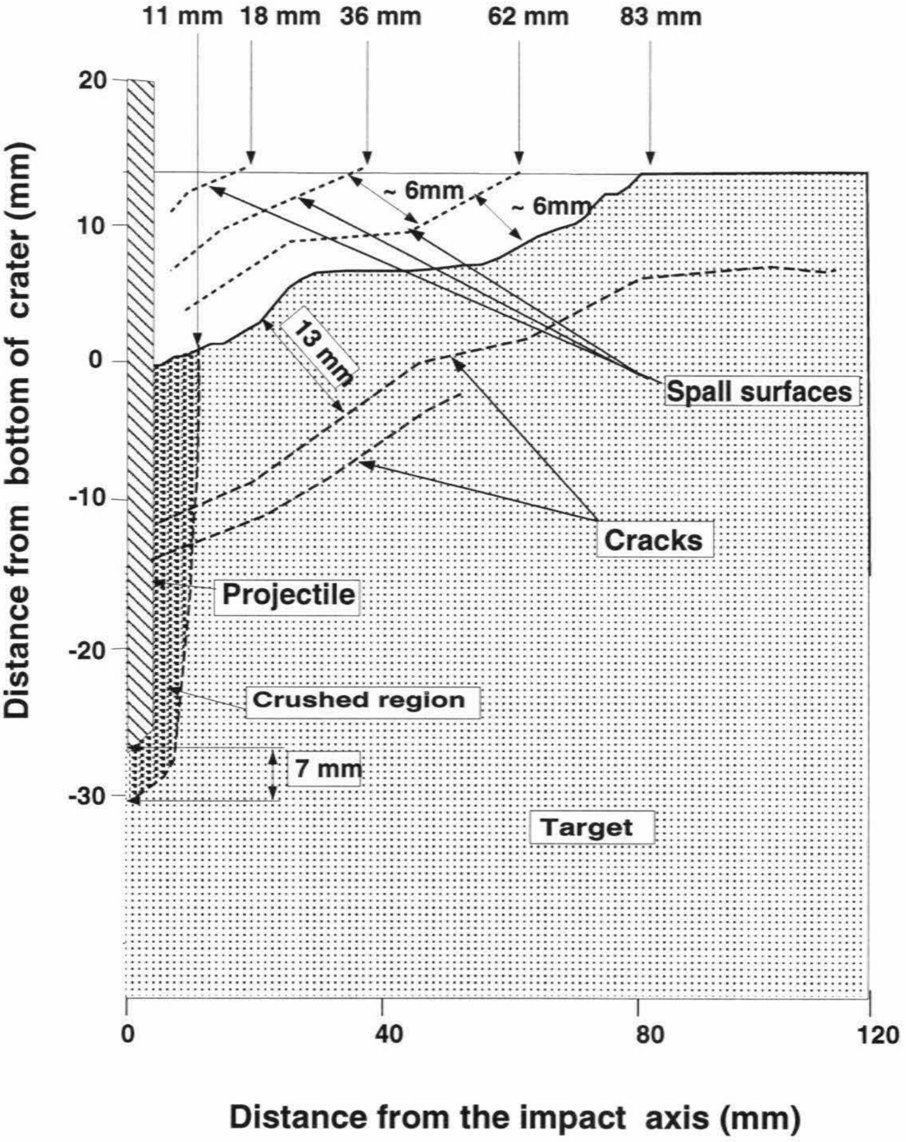

Figure 3.14: Schematic of cross-section of the target for Shot 1017.

~ 5 mm from bottom of penetration

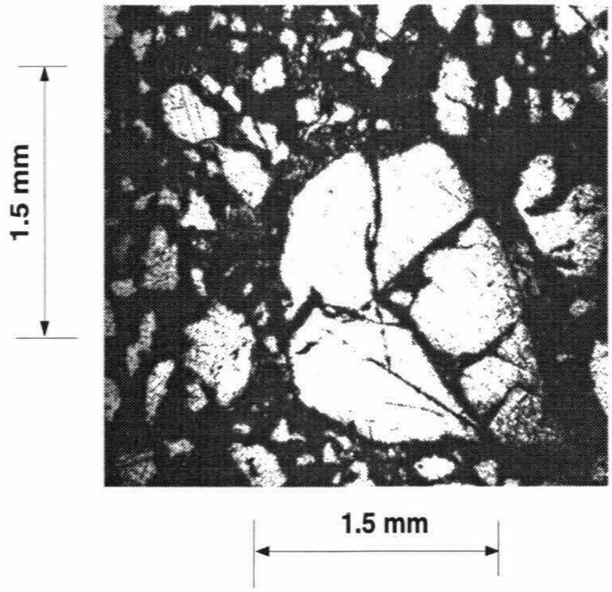

~ 35 mm from bottom of penetration

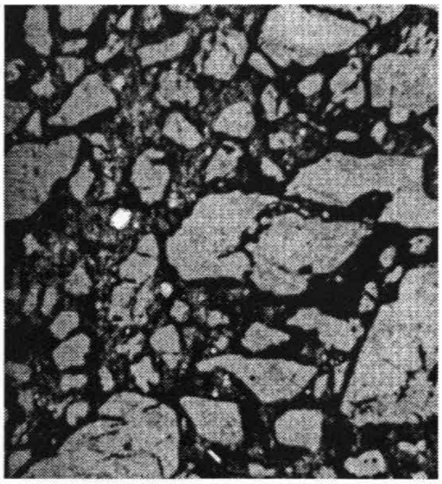

Figure 3.15: Microscopic images (reflected light) of mortar samples from Shot P38. White region is aggregate and dark region is cement.

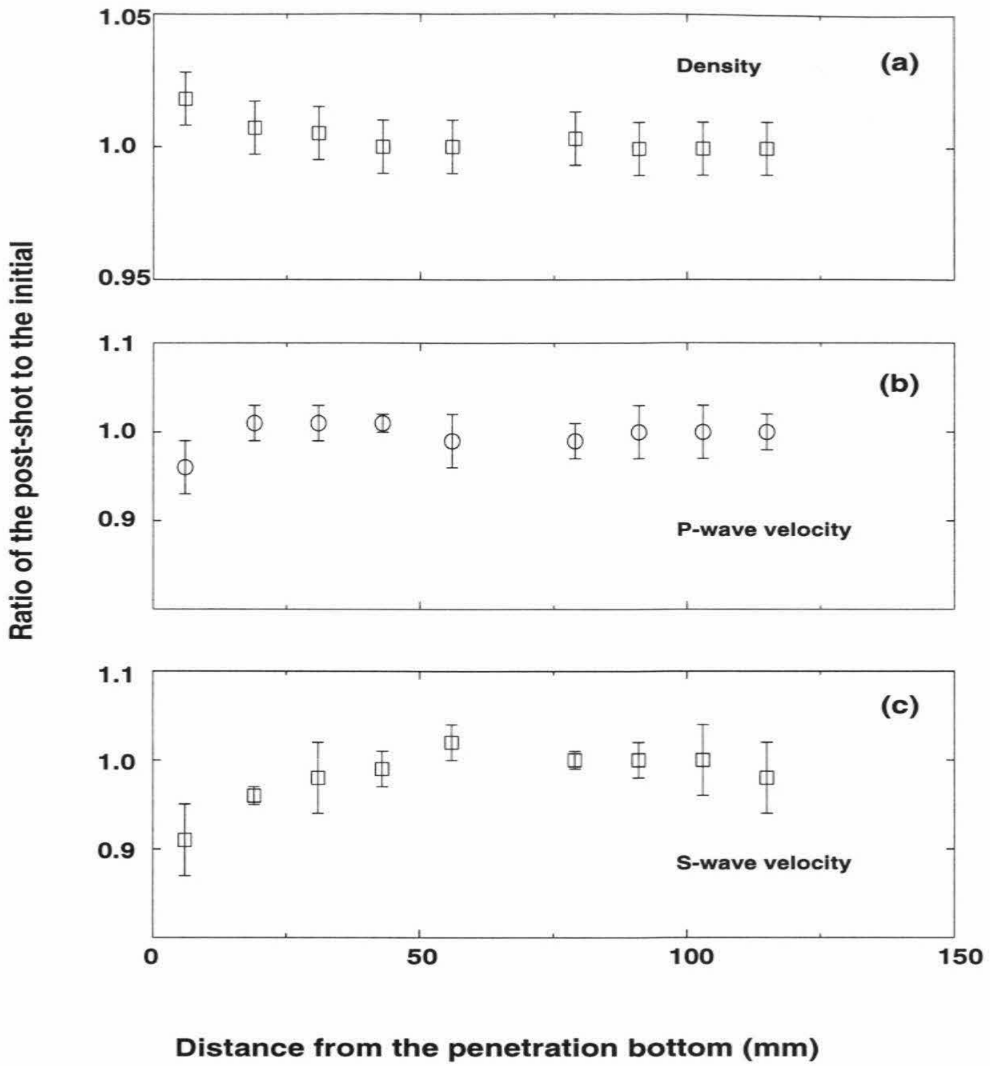

Figure 3.16: Relative variation of density, P- and S- wave velocities in damaged mortar target of Shot P38.

(a), (b) and (c) are relative ratio of the density, P- and S-wave velocities in samples from recovered target to initial density, P- and S-wave velocities in Table 3.4 versus distance from penetration bottom, respectively. The sample position is sketched in (d). The samples are ~1×1×1cm. The procedure to prepare the samples is given in details in *Rubin and Ahrens* [1991].

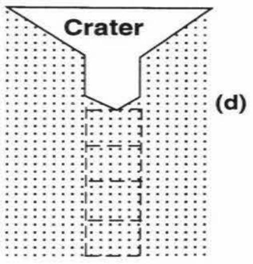

investigated on the recovered projectiles. They are defined as

1. Ink damage length $L_i$: This is measured from the projectile bourrelet (defined in Figure 3.4) to the point at which ink was cleaned but no visible erosion occurred on the projectile surface during penetration. This length only reflects that very light contact between projectile and target materials occurred in this area during penetration.

2. Projectile lateral surface damage length $L_d$: This is measured from the projectile bourrelet to the point at which the projectile surface was eroded by aggregates in the mortar during penetration. This length provides the area in which the projectile surface was in contact with target material under a certain normal pressure during penetration.

For Shot P38, the ink on the projectile lateral surface was nearly untouched by the target materials during penetration. For all the other experiments, various values of $L_i$ and $L_d$ are observed on recovered projectile surfaces. Figure 3.18 shows the two lengths as a function of final penetration depth. Figure 3.19 shows the same damage lengths (normalized by final penetration depth) versus final penetration depth. These results demonstrate that (1) $L_d$ is very short, $< 20\%$ of final penetration depth of the experiments with an intact target after impact. Therefore, frictional effects on the projectile lateral surface can be approximately ignored for an approximate analytic model to describe rigid body penetration into brittle materials under the conditions similar to the present experiments, and (2) for this projectile shape, it is very difficult to deploy an anchor into brittle materials because penetrators only have contact with less than 20 % of the final penetration depth.

The damage to the projectile head surface records the friction or temperature history effect on the surface during penetration. From the recovered projectiles, roughness of the projectile head surface increases with initial impact velocity. Due to the difficulty of measuring roughness on a non-planar surface, I do not show any direct data on the roughness here. However, the variation of projectile diameter at the bourrelet gives a certain degree of representation of the roughness on projec-

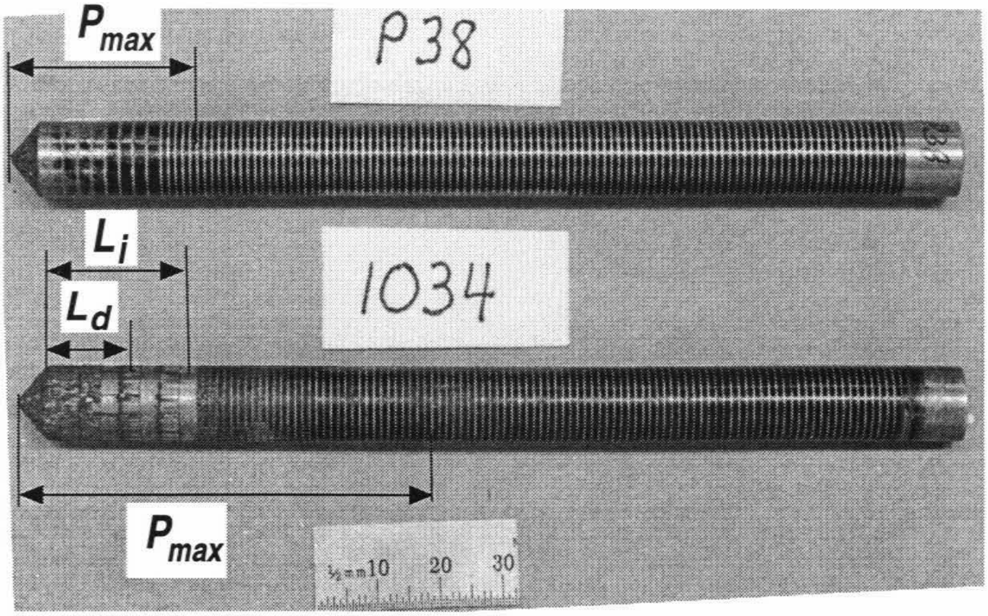

Figure 3.17: Photo of recovered projectiles. $P_{max}$ is final penetration depth. $L_i$ is ink damage length. $L_d$ is projectile lateral surface damage length.

tile head surface. Comparison of the projectile diameter measured before and after impact (Table 3.8) shows that the ratio of projectile diameter after impact to the diameter before impact decreases with impact velocity. Therefore, the roughness of the projectile head surface increases with impact velocity.

## 3.3 Penetration time history data and scaling

In this section, we discuss the experimental data on final penetration depth, energy per penetration unit volume, target dimension effects, penetration duration, penetration depth-time history, and we deduce the penetration velocity- and deceleration-time history. These parameters provide information on different aspects of the penetration process.

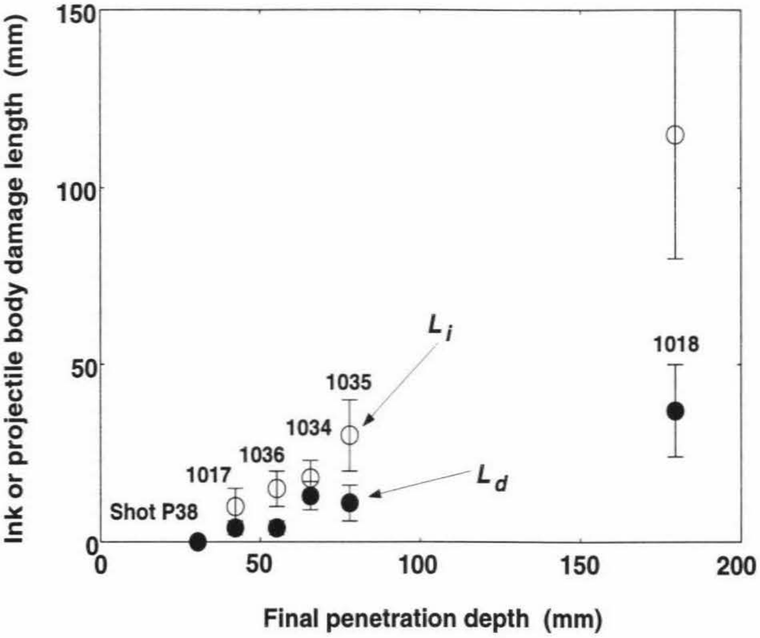

Figure 3.18: Damage length versus final penetration depth. Error bar comes from uneven damage on projectile surface.

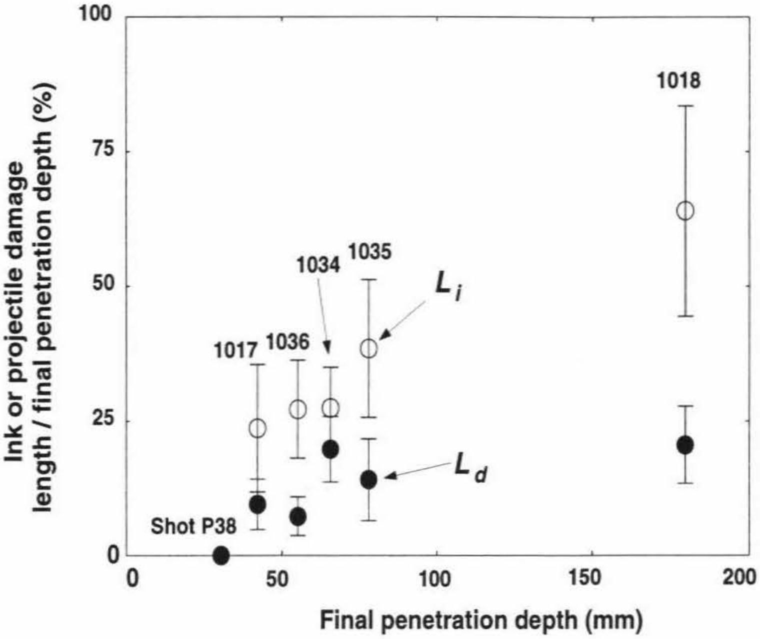

Figure 3.19: Normalized damage length versus final penetration depth.

Table 3.8: Projectile diameter change.

| Shot Num. | P38 | 1017 | 1034 | 1018 | 1035 | 1036 |
|---|---|---|---|---|---|---|
| $2R$ (mm) | 9.96 | 9.76 | 9.99 | 10.01 | 15.03 | 15.03 |
| $\phi_a$ (mm) | 9.95 | 9.69 | 9.86 | 9.65 | 14.98 | 15.00 |
| $\phi_a/(2R)$ | 1.00 | 0.993 | 0.997 | 0.964 | 0.997 | 0.998 |

$\phi_a$ is projectile diameter after impact. $\phi_a$ was measured at the location as shown in sketch.

Table 3.9: Penetration duration and depth.

| Shot # | Penetration duration ($\mu$s) | Penetration depth$^{(1)}$ (mm) | Penetration depth$^{(2)}$ (mm) | Crater depth (mm) |
|---|---|---|---|---|
| P38 | 327.1±3 | 30.2±0.5 | 30.4±0.4 | 10.5 ±2. |
| 1017 | 240± 6 | 41.4±1 | 42.2±0.3 | 13.6±2. |
| 1018 | | 179.5±10 | | |
| 1033 | 350.1±3 | 40.5±1. | 40.3±0.6 | 13.5±2. |
| 1034 | 385.8±3 | 66.7±1. | 65.2±0.6 | 26.4±4. |
| 1035 | 403±49 | 78±5 | | |
| 1036 | 371±49 | 55.2±1 | | 45.2±2 |

Penetration depth$^{(1)}$ is measured in recovered targets. Error of depth$^{(1)}$ comes from smoothness of target surface. Penetration depth$^{(2)}$ is given by the penetration depth-time history measurement. Error of depth$^{(2)}$ is determined by the width of the stripe that the laser beam was focused on when penetration stopped.

### 3.3.1 Final penetration depth

The relation between final penetration depth and initial projectile parameters is very important for all applications. For the present experiments, the parameters that were varied are projectile velocity, projectile dimensions (diameter and length) and projectile mass. The experimental data of Table 3.9 yield a good linear relation between final penetration depth, $P_{max}$, and impact energy per unit cross-section area, $e_s = mv^2/(2\pi R^2)$, for the experiments with intact targets after impact (Figure 3.20). A best fit to the experimental data yields

$$P_{max} = (1.15 \pm 0.08)e_s + (16.39 \pm 2.17), \tag{3.11}$$

where $P_{max}$ is in mm and $e_s$ is in J/mm$^2$. Because the two coefficients in Eq. (3.11) depend on target material properties, friction coefficient, projectile head shape etc., this scaling relation is only true for the same target material under the same projectile shape and rigid body assumption.

### 3.3.2 Energy per unit penetration volume

The impact energy required to open unit penetration volume reflects the resistance of the target material to penetration. It relates to target material strength and its rate dependence, friction coefficient, wave generation and crack propagation during penetration. In order to estimate this parameter, total penetration volume, $Vol$, is defined as

$$Vol = \pi R^2(P_{max} - R) + \frac{\pi}{3}R^3 = \pi R^2(P_{max} - \frac{2}{3}R), \tag{3.12}$$

where the term $\pi R^2/3$ is the volume of the conical head of the projectile. Then, energy per unit penetration volume, $e_v$, is

$$e_v = \frac{\frac{1}{2}mv^2}{Vol} = \frac{e_s}{P_{max} - \frac{2}{3}R}. \tag{3.13}$$

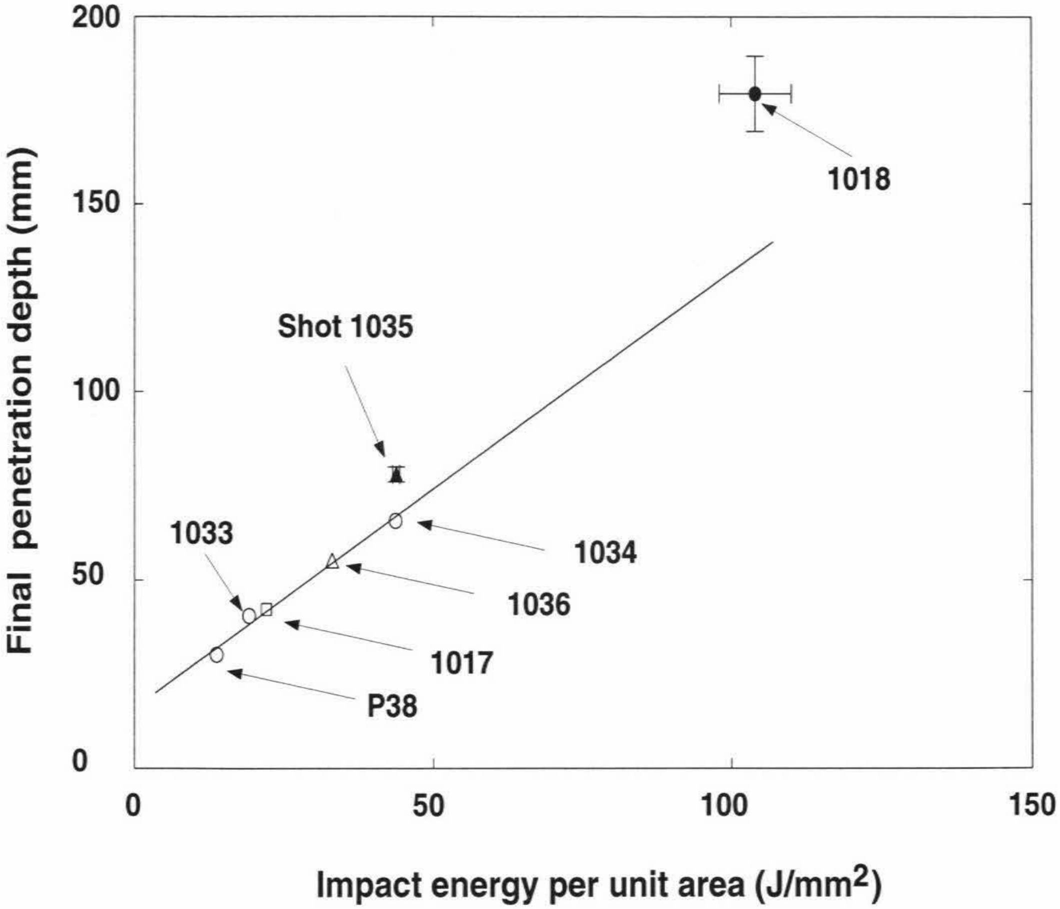

Figure 3.20: Final penetration depth versus initial impact energy per unit cross-section area. Solid line is linear fit to the data (Eq. (3.11)).

Based on the experimental data, $e_v$ is given in Figure 3.21. It shows that $e_v$ increases from 0.5 J/mm$^3$ at $e_s = \sim 15$ J/mm$^2$ to $\sim 0.7$ J/mm$^3$ at $e_s = \sim 45$ J/mm$^2$. Substituting Eq. (3.11) into Eq. (3.13), $e_v$ is a function of $e_s$ as

$$e_v = \frac{e_s}{(1.15 \pm 0.08)e_s + (16.39 \pm 2.17) - \frac{2}{3}R}, \tag{3.14}$$

where $e_v$ is in J/mm$^3$, $e_s$ is in J/mm$^2$ and $R$ is in mm. The calculated results for 10 and 15 mm diameter projectiles are also given in Figure 3.21. From Figure 3.21, $\partial e_v / \partial e_s$ decreases with increasing $e_s$.

$e_v$ also represents average pressure acting on the target material in the spot beneath the penetrator during penetration. This pressure includes all contributions from wave generation, material strength and its strain rate dependence and also friction. Figure 3.21 demonstrates that averaged pressure acting on the projectile is 0.5 GPa at $e_s = \sim 15$ J/mm$^2$ and 0.7 GPa at $e_s = \sim 45$ J/mm$^2$ (J/mm$^3$ $\sim$ GPa). These values are $\sim$ 10 to 20 times higher than the resistance pressure expected based on unconfined strength tests of the G-mixture mortar (0.04 GPa under quasi-static loading (*Wahlstrom* [1998])) and $\sim$ 6 to 8 times higher than the resistance pressure due to the mortar unconfined strength expected from the Hugoniot elastic limit (Figure 3.3). If it is assumed that friction coefficient is 1, the measured averaged pressure is still $\sim$ 3 to 4 times higher than the possible highest averaged pressure just due to mortar strength and its rate dependence. Therefore, the dependence of material strength on strain rate and the friction effect alone can account for less half of the estimated energy consumed during penetration. This result demonstrates that wave generation may be the dominant process during rigid body penetration into brittle materials.

### 3.3.3 Effects of target dimension on penetration

Scaling relations based on experimental data are always used to predict penetration parameters in various applications in which target dimensions are much larger than

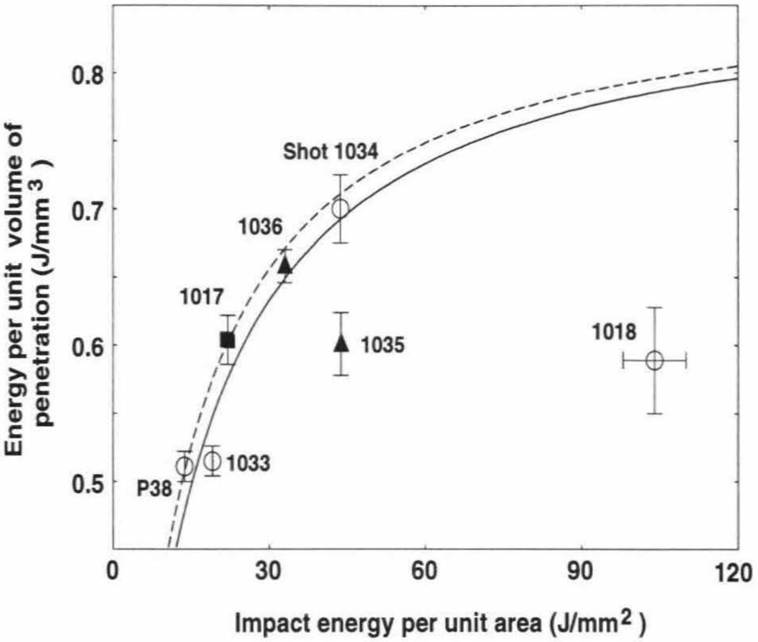

Figure 3.21: Energy per unit penetration volume versus impact energy per unit cross-section area. Dashed and solid lines are calculated from Eq. (3.14) for projectiles with 15 and 10 mm diameter, respectively.

targets used in laboratory experiments. Therefore, the effect of target dimension on penetration parameters should be considered properly in order to give reasonable predictions.

For brittle target materials, finite dimensions affect penetration processes via two ways: interactions between the wave generated from penetration and the free surface, and also cracks generated during penetration which may reach the free surface. Figure 3.21 demonstrates that interaction between cracks and the free surface has significant effects on penetration under the present experimental conditions because $e_v$ for the experiments in which targets were intact after impact (Shots P38, 1017, 1033, 1034 and 1036) is much higher than $e_v$ for the experiments in which targets were broken into pieces (Shots 1018 and 1035) during penetration. Therefore, in order to avoid data contamination from crack propagation in brittle materials, an upper limit to the initial projectile velocity must be determined based on target dimensions. Because target dimension effects on penetration come from crack propagation through the

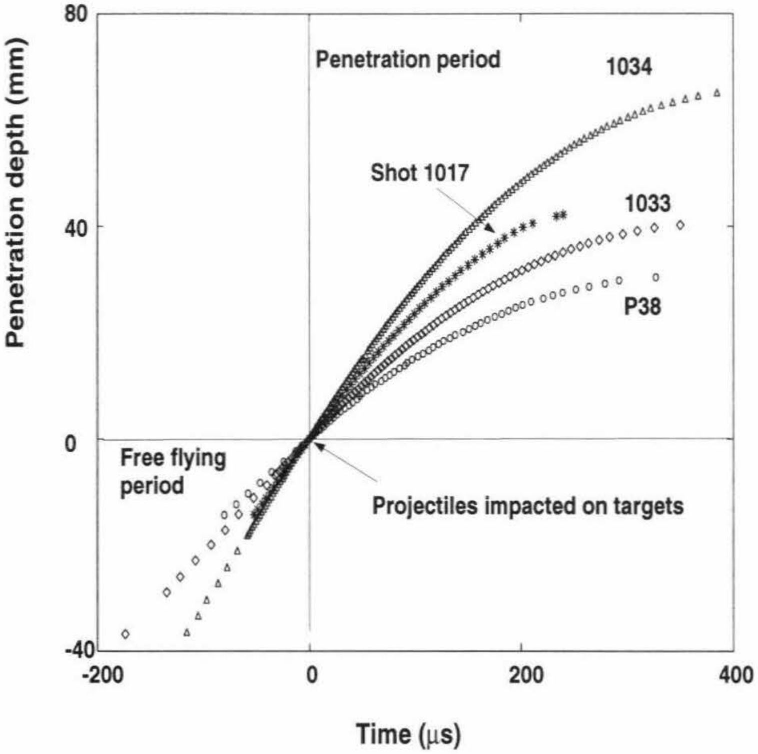

Figure 3.22: Penetration depth versus time.

target, the method used to encapsulate brittle target materials with a cylindrical steel shell (e.g., *Forrestal et al.* [1992]) to eliminate finite dimension effects appears to be difficult to rationalize.

For a mortar target with a diameter of 500 mm, the finite dimensions will significantly affect the penetration when the velocity of 10 (15) mm diameter and 150 mm length projectiles is above 350 (280) m/s, based on the present experiments.

### 3.3.4 Penetration time history

As discussed in Chapter 1, the penetration time history is important for both applications (on-board instrument safety) and understanding of the penetration process itself because it provides detailed information on the interaction between the projectile and target materials during penetration. In the following, experimental data on penetration depth-time histories is presented first, and then the deduced parameters are discussed in detail. Penetration depth-time histories obtained from the experiments are given in Figure 3.22. Penetration durations, $t_{max}$, are listed in Table 3.9.

### Penetration duration

Penetration duration is one of important parameters in penetration dynamics because it provides the time constraints on theoretical models and practical applications. Due to the difficulty in measuring it, no empirical scaling relation has been published and only a few very scattered data are available for very large dimension experiments on soil targets(*Heuze* [1990]). In general, the duration of penetration depends on initial velocity, target materials, and projectile dimensions. Based on the present results, we only discuss the effects of initial velocity and projectile dimension on penetration duration.

Figure 3.23 gives the experimental data on penetration duration versus $e_s$. The experimental results demonstrate:

1. Penetration duration increases very slowly with the $e_s$ for projectiles with same length.
2. The large difference between penetration durations for Shot 1017 and 1033 shows that penetration duration is very sensitive to projectile length.
3. Projectile diameter does not play an important role in changing penetration duration if mass per unit cross-section area is approximately constant (0.86 g/mm$^2$ for 10 mm diameter projectiles and 0.89 g/mm$^2$ for 15 mm diameter projectiles).

Based on the experimental data, the penetration duration $t_{max}$ for the experiments with the same projectile length is linearly proportional to $e_s$ (Figure 3.23). A best fit to the data yields

$$t_{max} = (2.08 \pm 0.25)e_s + (303.64 \pm 8.04), \tag{3.15}$$

where $t_{max}$ is in $\mu s$ and $e_s$ is in J/mm$^2$. As mentioned above, penetration duration is not sensitive to $e_s$, e.g., $t_{max}$ only changes $\sim$ 25% while $e_s$ increases by 4 times ($t_{max}$= 324.4 and 407 $\mu$s at $e_s$ = 10 and 50 J/mm$^2$, respectively).

Based on Eq. (3.15) and the fact that penetration duration is approximately independent of projectile diameter, penetration duration is believed to be mainly controlled by projectile mass per unit cross-section area, $m_m = m/(\pi R^2)$. In addition, the penetration duration of Shot 1017 is much shorter than that of Shot 1033 although $e_s$ is approximately the same ($e_s$ is 22 and 19 J/mm$^2$ for Shot 1017 and 1033, respectively). Therefore it is believed that the dependence of $t_{max}$ on $m_m$ should be reflected by the second term in Eq. (3.15). As an estimation, the second term is assumed to be linearly proportional to $m_m$ and Eq. (3.15) is rewritten as

$$t_{max} = (2.08 \pm 0.25)e_s + (349.0 \times m_m \pm 8.04), \tag{3.16}$$

where $m_m$ is in g/mm$^2$. $t_{max}$ is calculated to be 253.4 $\mu$s using Eq. (3.16) for the conditions of Shot 1017 ($e_s$=22 J/mm$^2$ and $m_m$ = 0.595 g/mm$^2$). The predicted penetration duration is in good agreement with the measured penetration duration (240 $\mu$s). Therefore, Eq. (3.16) approximately gives the scaling rule of penetration duration under the present experimental conditions.

### Penetration velocity-time history

The penetration velocity time-history is deduced by differentiating a tenth-degree polynomial that fits measured penetration depth-time history data for each experiment. The deduced velocity-time histories (Figure 3.24) are divided into three stages as:

1. Initial penetration stage: In this stage, the projectile velocity did not change significantly during a short period ($\sim$ 20 $\mu$s) just after the projectile impacted the target. This is due to both the rigid body assumption (velocity change on impact surface needs some time ($\sim$ 10 $\mu$s) to affect the velocity at measurement

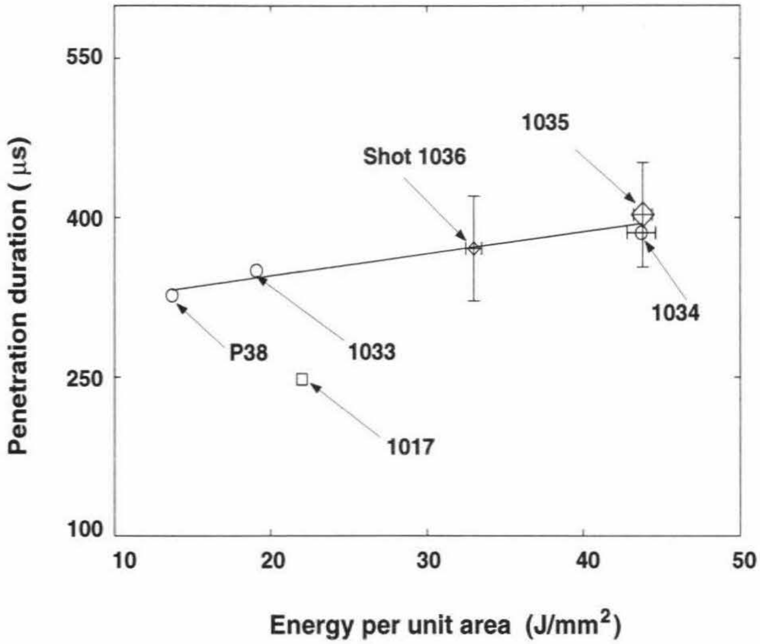

Figure 3.23: Penetration duration versus energy per unit area. Solid line is linear fit (Eq. (3.15)).

location) and the very small contact area between the projectile head and the target material during the initial penetration.

2. Steady penetration stage: In this stage, the projectile was under a relatively long and steady deceleration period. The duration of this period is $\sim$ 276, 170, 325 and 318 $\mu$s for Shots P38, 1017, 1033 and 1034, respectively.

3. Penetration stop stage: When projectile velocity decreased to a critical value, projectile deceleration increased and penetration stopped suddenly. The critical velocity is $\sim$ 37, 37, 18 and 49 m/s for Shots P38, 1017, 1033 and 1034, respectively. The average critical velocity for projectiles with 150 mm length and 10 mm diameter is (35±15) m/s.

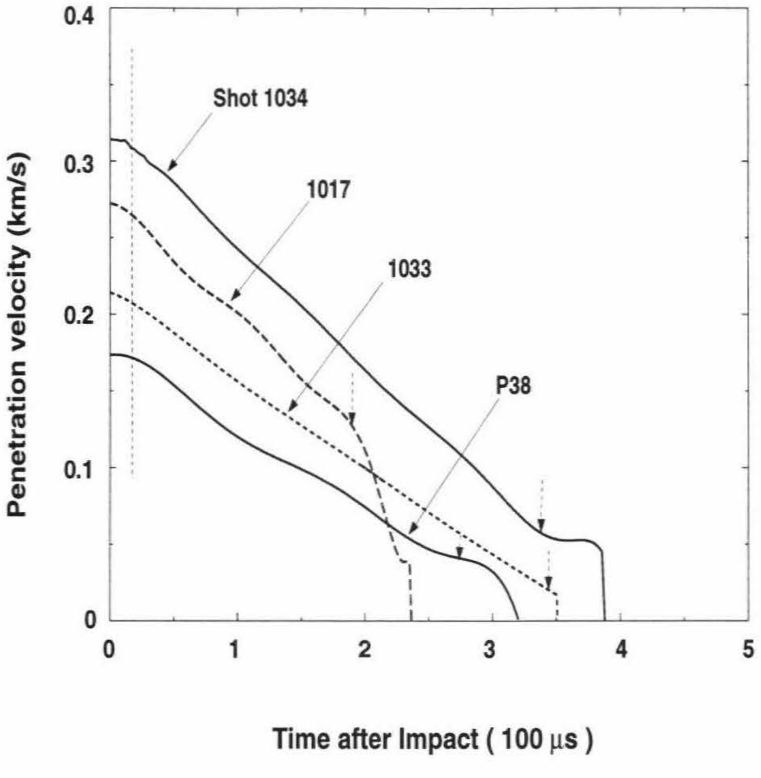

Figure 3.24: Deduced penetration velocity time history. The initial penetration stage is between the vertical dashed line and zero time (impact time). The steady penetration stage is between the vertical dashed line and the vertical arrow. The penetration stop stage is beyond the vertical arrow.

### Penetration deceleration-time history

In order to deduce the deceleration from the measured penetration depth-time history, the tenth-order polynomial was differentiated twice. But the result was very noisy generally because the second differentiation magnifies the minor misfit of the polynomial to the data and measurement errors. The best deceleration time-history deduced is for Shot 1033 as shown in Figure 3.25. The features of deduced deceleration time history are (1) deceleration increases rapidly from 0 to about $7\times10^4$ g in the first $\sim 40$ $\mu$s, (2) deceleration slowly decreases from $7\times10^4$ g to $\sim 5.5\times10^4$ g in about 270 $\mu$s and (3) deceleration jumps up again when penetration is close to stopping.

In order to estimate average deceleration amplitude during penetration, penetration velocity in the steady penetration stage is assumed to decrease linearly with time (Figure 3.24). Then, the average deceleration obtained is shown in Figure 3.26. The results demonstrate that the average deceleration, $\overline{a}$, in the steady penetration stage for projectiles with same length is linearly proportional to initial impact velocity. A best fit to the data for projectiles with same length yields:

$$\overline{a} = 192.4v + 1.89 \times 10^4, \tag{3.17}$$

where $\overline{a}$ is in g, and $v$ is in m/s.

Eq. (3.17) can be used to estimate averaged pressure acting target materials during steady penetration. Assuming that friction force on projectile lateral surface is ignored as discussed in previous section, for a conical projectile, pressure normal to the projectile cone surface, $\sigma$, is (detail discussion is given in Chapter 4)

$$\sigma = \frac{m\overline{a}}{\sqrt{2}\pi R^2(\eta\cos(\theta) + \sin(\theta))}, \tag{3.18}$$

where $\eta$ is the friction coefficient and $\theta$ is the half-cone angle. The possible value of $\eta$ ranges from 0 to 1 (*Kishida and Uesugi* [1987]). Therefore, upper and lower limit of $\sigma$ is estimated when $\eta = 0$ and 1, respectively as shown in Figure 3.27. This

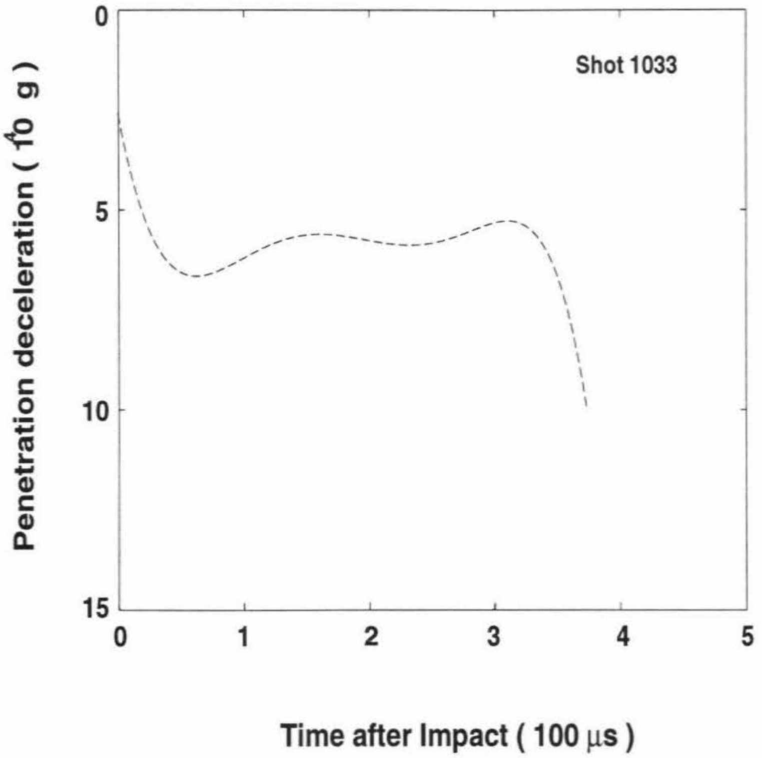

Figure 3.25: Deduced deceleration time history.

estimated results once again show that resistance pressure acting on projectile surface is about 2 to 4 times higher than the possible highest pressure induced only by friction and material strength and its strain rate effect. In order to estimate average shock wave pressure generated by the penetration in target materials, particle velocity is assumed to be half of initial impact velocity. Then average shock wave pressure is calculated using the Hugoniot relation of *Read and Maiden* [1971] listed in Table 3.5. The average shock wave pressure (Figure 3.27) is very comparable with the average pressure acting on projectile surface. Therefore, this result strongly supports that shock wave generation is the dominant process during rigid body penetration into brittle materials under present experimental conditions.

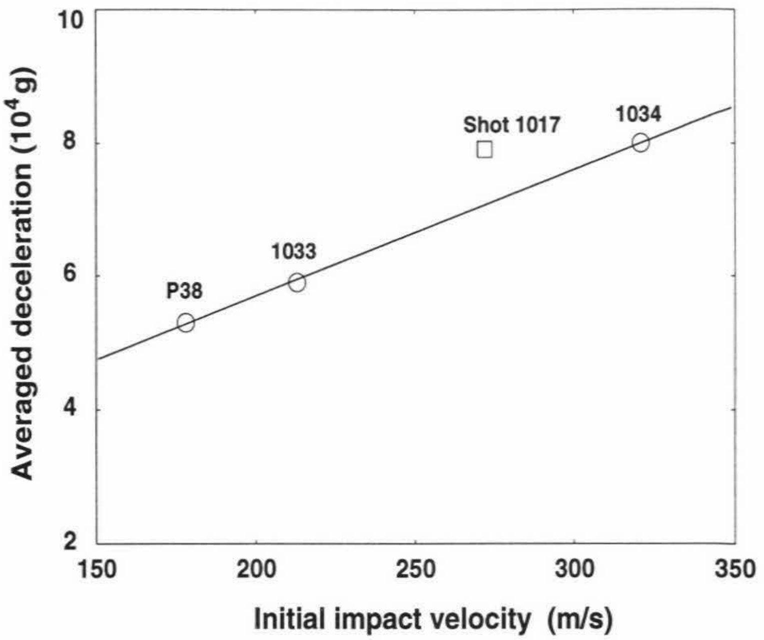

Figure 3.26: Averaged deceleration versus initial impact velocity. Solid line is linear fit to the data of Shots P38, 1033 and 1034 (Eq. (3.17)).

### 3.3.5 Penetration process similarity

The purpose to investigate the similarity among penetration time histories under different initial conditions is to see if any scaling relation for penetration time histories exists. Figure 3.28 shows all the experimental data of penetration depth time history normalized by final penetration depth versus penetration time normalized by penetration duration. It demonstrates a very strong penetration process similarity among the experimental data of Shots P38, 1033 and 1034. These experiments have same projectile length and diameter. The relation between the normalized penetration depth versus the normalized penetration time is fully similar with each other in whole penetration process. This result suggests that a scaling relation for penetration process with same projectile dimensions exists as

$$\frac{P(t,v)}{P_{max}} = f(\frac{t}{t_{max}}), \tag{3.19}$$

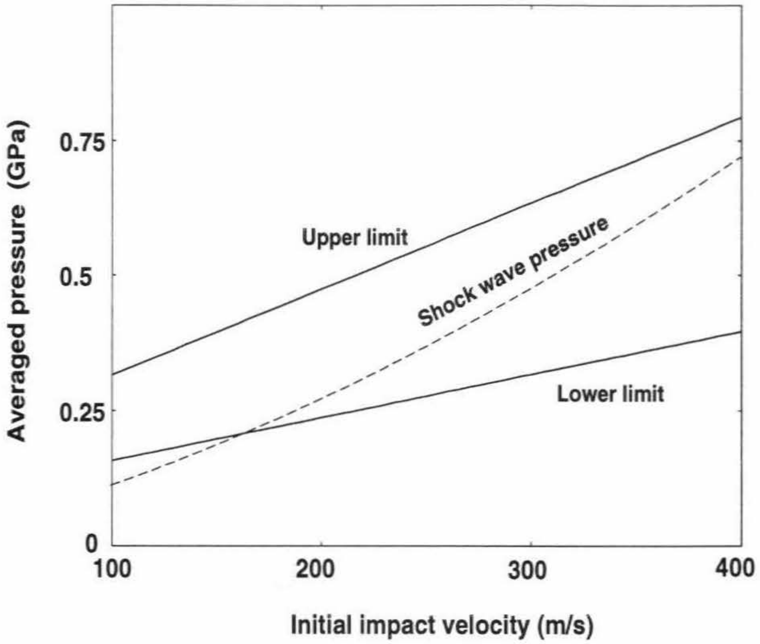

Figure 3.27: Average pressure normal to projectile surface versus initial impact velocity. Upper and lower solid lines are calculated using Eq. (3.18) under $\eta$ =0 and 1, respectively. Dashed line is calculated using the Hugoniot relation of *Read and Maiden* [1971] under the assumption that the average particle velocity in G-mixture mortar is half of the initial impact velocity.

where $f$ is a function of $t/t_{max}$. $f$ can be determined by polynomial fit to the data of the three experiments (Shots P38, 1033 and 1034). Then, the scaling relation of penetration depth time history is

$$P(t,v) = P_{max} f(\frac{t}{t_{max}}). \tag{3.20}$$

Substituting $P_{max}$ and $t_{max}$ with Eq. (3.11) and (3.16), respectively, the scaling relation is

$$P(t,v) = ((1.15 \pm 0.08)e_s + (16.39 \pm 2.17)) f(\frac{t}{(2.08 \pm 0.25)e_s + (349.0 \times m_m \pm 8.04)}). \tag{3.21}$$

If the projectile dimension effect has been included in $e_s$ and $m_m$, Eq. (3.21) can be used to predict penetration depth-time history under different initial conditions. Using Eq. (3.21), the predicted penetration depth time history of Shot 1017 is in a very good agreement with the experimental data as shown Figure (3.28). Based on this figure, projectile dimension effect on penetration process seems to be included in $e_s$ and $m_m$. Therefore, Eq. (3.21) can be used to scale penetration depth-time history under different initial conditions for rigid body penetration into G-mortar target. Also, Eq. (3.21) predicts that average deceleration of projectiles increases with projectile length, this is confirmed by the experimental results shown in Figure 3.26. However, I must mention that the above conclusion is only based on the experimental data under two projectile lengths, and more experiments are needed to verify it.

## 3.4 Comparisons among empirical relations

In order to compare the predictions of previous empirical relations, the empirical parameters in Eqs. (1.5), (1.6), and (1.7) are determined based the present data because these expressions were suggested for penetration into rocks or concretes. Only the data of the experiments in which the targets were still intact after impact

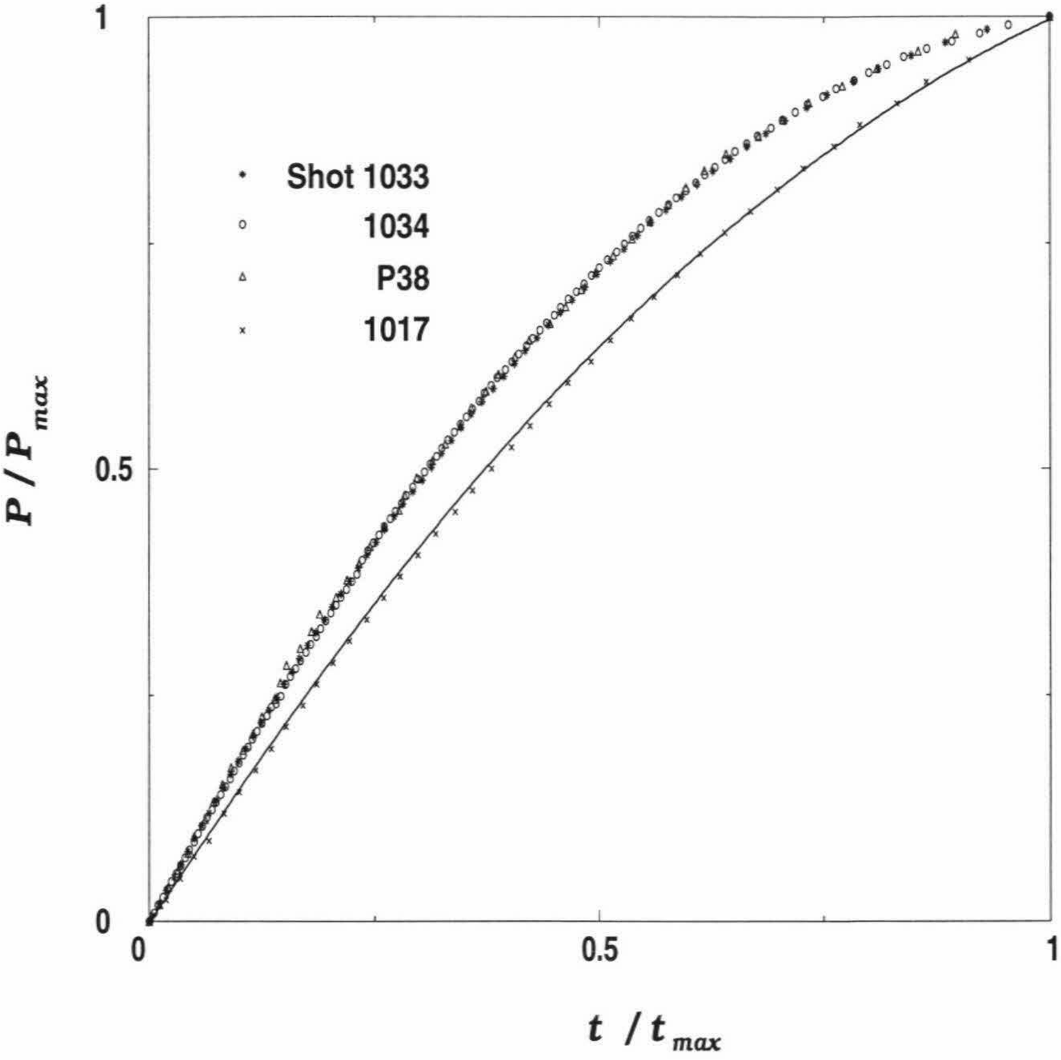

Figure 3.28: Normalized penetration depth versus normalized penetration time. Solid line is penetration depth-time history for Shot 1017 predicted using Eq. (3.21).

are used to determine the parameters.

1. Eq. (1.5) suggested by Sandia National Laboratories is given again as

$$P_{max} = 1.14 \times 10^{-6} S \times N \frac{m}{A}(v_0 - 100), \tag{3.22}$$

   where $S$ and $N$ are defined as target penetrability number (a measure of rock resistance) and projectile nose performance coefficient. Although Eq. (3.22) includes two dimensionless empirical parameters, they are equivalent to one parameter. The averaged value of $S \times N$ determined from the present data is

$$S \times N = 0.353 \pm 0.035. \tag{3.23}$$

   Substituting this value into Eq. (3.22), the predicted final penetration depth using Eq. (3.22) is shown in Figure 3.29.

2. Eq. (1.7) (Army's Waterways Experiment Station (*Heuze* [1990])) is

$$P_{max} = \frac{M}{A}\frac{N_{rc}}{\rho}[\frac{v_0}{3}(\frac{\rho}{\sigma_{cr}})^{0.5} - \frac{4}{9}\ln(1 + \frac{3v_0}{4}(\frac{\rho}{\sigma_{cr}})^{0.5})], \tag{3.24}$$

   where $\rho$ is target material density, and

$$\begin{aligned} N_{rc} &= 0.863(\frac{4(\mathrm{CRH})^2}{4\mathrm{CRH} - 1})^{0.25}, \quad \text{for a ogive head projectile ,} \\ N_{rc} &= 0.805 \sin^{-0.5}(\theta), \quad \text{for a cone head projectile,} \\ \sigma_{rc} &= \sigma_f(\frac{\mathrm{RQD}}{100})^{0.2}. \end{aligned}$$

   Because the projectiles used in the present experiments had conical head with half-angle 45°, $N_{rc} = 0.957$. Only one parameter, $\sigma_{rc}$, needs to be determined empirically. Based on the present experimental data, the average value of $\sigma_{rc}$ is

$$\sigma_{rc} = 81.5 \pm 9, \qquad \text{MPa}. \tag{3.25}$$

Substituting the determined values into Eq. (3.24), the predicted final penetration depth is shown in Figure 3.29. From the definition of RQD (*Heuze* [1990]), the value of RQD must be $< 100$ for any materials with pre-existed micro-cracks, cavities etc. because RQD $= 100$ is for perfect target materials. However, RQD is deduced to be 2060 when $\sigma_f = 44.5$ MPa for the G-mixture mortar.

3. *Forrestal* [1986] suggested that the final penetration depth of a projectile with a ogive nose (Eq. (1.6)) is

$$P_{max} = \frac{m}{2A\rho z}\ln(1 + \frac{\rho v_1^2 z}{B}) + 4R, \qquad P_{max} > 4R, \tag{3.26}$$

where $v_1$ and $z$ are defined as

$$v_1^2 = v_0^2 - \frac{4\pi R^3 B}{m}, \tag{3.27}$$

$$z = \frac{4R_o R - R^2}{6R_o}, \tag{3.28}$$

where $R_o$ is ogive head radius (Figure 1.1).

For a conical projectile, $z = 0$ because $R_o$ is infinite. Therefore, Eq. (3.26) can not be used for a conical projectile directly. However the right-hand-side of Eq. (3.26) is $0/0$ type when $z \to 0$, the limit of the right-hand-side is

$$\lim_{z \to 0} P_{max} = \frac{m v_1^2}{2AB} + 4R. \tag{3.29}$$

Using the definition of $v_1$ (Eq. (3.27)), the above equation is

$$P_{max} = \frac{mv_0^2}{2AB} + R(4 - \frac{2}{\pi}). \tag{3.30}$$

The averaged value of $B$ is determined to be

$$B = (9.3 \pm 1.1) \times 10^8, \qquad \mathrm{J/m^3}. \tag{3.31}$$

Substituting the $B$ value into Eq. (3.30), the predicted final penetration depth is given in Figure 3.30.

Figures 3.29 and 3.30 demonstrate that all the three expressions discussed above give reasonable prediction of final penetration depth under the present experimental conditions. Eq. (3.22) predicts that final penetration depth is linearly proportional to impact momentum per unit cross-section area, and Eq. (3.24) also predicts the same relation when initial impact velocity is not very high (say, $v_0 < 4(\sigma_{cr}/\rho)^{0.5}/3$, that is $\sim$ 280 m/s under the present experimental conditions). Eq. (3.30) predicts that final penetration depth is linearly proportional to impact energy per unit cross-section area. However, the present experimental data show that the final penetration depth is linearly proportional to the impact energy per unit cross-section area. Therefore, the present experimental data support the linear relationship between final penetration depth and impact energy per unit area.

## 3.5 Conclusions

From the experimental data and the simple consideration of impact physics, the conclusions are:

1. The compressive strength strain rate dependence of the G-mixture mortar is

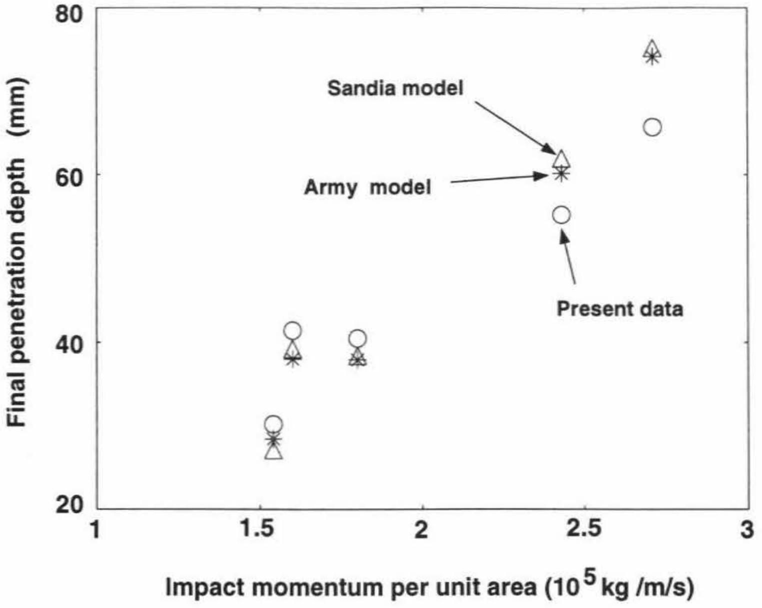

Figure 3.29: Final penetration depth versus impact momentum per unit area.

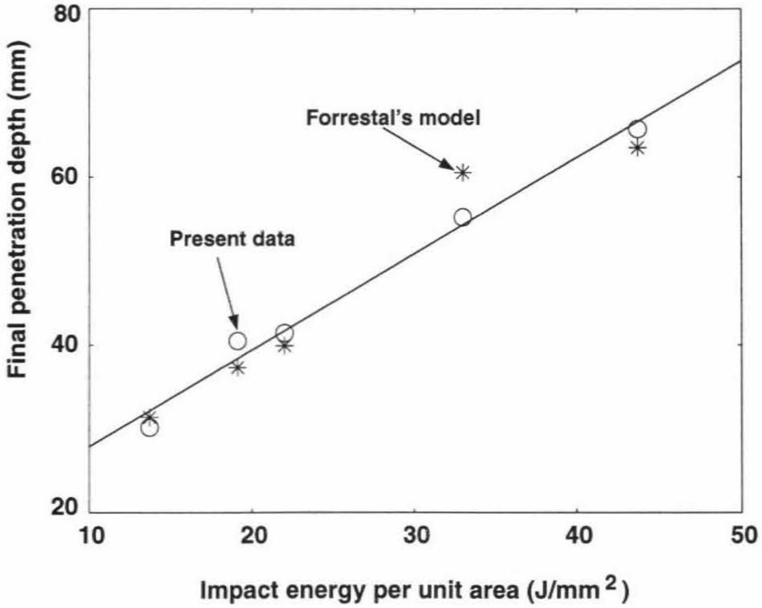

Figure 3.30: Final penetration depth versus impact energy per unit area. Solid line is Eq. (3.11).

described by

$$\frac{\sigma_f}{\sigma_f^0} = \exp(0.095(\log(\frac{\dot{\varepsilon}}{\dot{\varepsilon}_0}))^{1.14}), \tag{3.32}$$

for a strain rate in the range of $10^{-7}$/s to $10^3$/s.

2. The non-dispersive Hugoniot elastic wave in the G-mixture has an amplitude of $\sim 0.14$ GPa and a velocity of $\sim 4.3$ km/s. The amplitude of the dispersive elastic wave is about 0.1 GPa under the peak shock wave pressure of $\sim 1$ GPa. The present experimental data show that the Hugoniot relation of *Read and Maiden* [1971] can be used to approximately describe the G-mixture mortar response to shock loading.

3. The target materials are damaged via compacting in the region in front of penetrators and via brittle radial and lateral cracks propagations in the region surrounding penetration path. Macro-cracks just in front of penetrators as suggested by *Forrestal and Tzou* [1998] and *Bless et al.* [1978] were not produced in the material studied here. The density measurement verifies that target material in front of penetrators was compacted. The results suggest that expected cracks in front of penetrators may be stopped by the comminuted region.

4. Radial crack traces on impact surface are very straight along radial from impact site. The number of radial cracks appearing on impact surface is between 4 and 8. Since radial cracks have longer length than lateral cracks, the radial cracks must propagate either faster or be generated earlier than the lateral cracks. Radial crack length appearing on impact surface is correlated with initial projectile energy.

5. Lateral cracks have circular trace on impact surface. The distance between two adjacent lateral cracks increases with the distance from impact site. Lateral cracks follow a very complex propagation path given by crater profiles. Crack surface morphology looks similar to that of the radial cracks and seems to be tensile cracks. Crater radius induced by lateral cracks is scaled with initial

impact velocity and projectile radius. The crater depth is linearly scaled with initial impact energy.

6. Energy needed to create unit penetration volume is found to be increase with impact velocity or penetration depth for the experiments in which targets were still intact after impact. Based on average value of energy per unit penetration volume, average pressure acting on target material during penetration is found to be 10 to 20 times higher than that due to strength of target materials under quasi-static loading and 3 to 4 times higher than the possible highest pressure due to friction, material strength and its rate dependence. This result also suggests that shock wave generation may be dominant process during penetration.

7. The interaction between cracks and target free surface significantly affects rigid body penetration into brittle materials based on present data. The experimental results show that the upper velocity limit for the mortar target with 500 mm diameter and 400/600 mm length is about 350 m/s when projectiles have a 10 mm diameter and an 150 mm length, 280 m/s when projectiles have a 15 mm diameter and an 150 mm length if effect induced by interaction between cracks and lateral free surface is avoided.

8. Aggregate erosion on projectile lateral surface is $< 20$ % of final penetration depth. This result suggests that lateral friction effect on penetration process can be approximately ignored, and shows the difficulty to employ penetrators into brittle materials as anchors. The roughness of projectile head surfaces increases with penetration velocity. This reflects friction (temperature) effects on projectile head surface.

9. Final penetration depth, $P_{max}$, is linearly scaled with initial projectile energy per unit cross-section area, $e_s$, for projectiles with same projectile head shape, different length and diameter when targets are intact after impact. Based on

the experimental data on the G-mixture mortar targets, the scaling relation is

$$P_{max} = (1.15 \pm 0.08)e_s + (16.39 \pm 2.17), \tag{3.33}$$

where $P_{max}$ is in mm and $e_s$ is in J/mm$^2$.

10. For the first time, whole penetration depth-time history was recorded with very dense datum point under $10^5$ g deceleration. The results provide dynamic constrains to theoretic models, specially numerical simulations.

11. Penetration duration, $t_{max}$, is found to scale linearly with $e_s$ for projectiles with same length and different diameters. Based on experimental data, the relation for 150 mm long projectiles with a 10 or 15 mm diameter is

$$t_{max} = (2.08 \pm 0.25)e_s + (303.64 \pm 8.04), \tag{3.34}$$

where $t_{max}$ is in $\mu$s and $e_s$ is in J/mm$^2$.

Based on the facts that $t_{max}$ is not very sensitive to $e_s$ and seems not to depend on projectile radius approximately, and the large difference between the penetration durations of Shots 1017 and 1033, penetration duration dependence on projectile length is believed to be reflected by the large value of the second term in Eq. (3.34). Therefore, penetration duration dependence on projectile length is suggested to be described by

$$t_{max} = (2.08 \pm 0.25)e_s + (349.0 \times m_m \pm 8.04), \tag{3.35}$$

where $m_m = m/(\pi R^2)$. The prediction from this relation is in good agreement with the experimental data under different projectile length.

12. Deduced penetration velocity time histories suggest that whole penetration history is divided into three stages: (1) initial stage in which projectile velocity

change is small due to very small contact between projectile and target materials, (2) steady penetration stage in which projectile velocity continues to decrease smoothly, (3) penetration stop stage in which projectile deceleration jump up when velocities is close to a critical value that is $\sim 35$ m/s from the experiments. Generally, the first and last stages are much shorter than the second.

13. Deduced average deceleration, $\overline{a}$, in the steady penetration stage is found to be linearly proportional to initial impact velocity when projectiles have the same dimensions. Based on the experimental data, $\overline{a}$ is

$$\overline{a} = 192.4v + 1.89 \times 10^4, \tag{3.36}$$

where $\overline{a}$ is in g and $v$ is in m/s. Average pressure acting on target materials during penetration is estimated to be very comparable with shock wave pressure. This result suggests once again that shock wave generation is the dominant process for energy exchanging between projectile and target materials during penetration.

14. The experimental data of penetration depth-time histories suggest that a penetration process similarity between normalized penetration depth, $P/P_{max}$, and normalized penetration time, $t/t_{max}$, exists. This similarity is obtained to be

$$\frac{P}{P_{max}} = f(\frac{t}{t_{max}}), \tag{3.37}$$

where $f$ is a function of $t/t_{max}$. After $f$ is determined using the penetration depth-time history of the experiments with 150 mm length and 10 mm diameter projectiles, the predicted penetration depth-time history is in good agreement with the experimental data for projectile with 100 mm length and 10 mm diameter in whole penetration process. This similarity also predicts that average deceleration in the steady penetration stage increases with decreasing of projectile length. This is verified by the experimental data.

# Chapter 4 An analytical model for rigid body penetration

The scaling/empirical relations discussed in Chapter 3 do not give the physics involved in dynamic penetration processes. In order to understand penetration process, first principle models (analytic and numerical) are needed. In this part, we suggest a simple analytic model for rigid body penetration based on the experimental data described in Chapter 3.

## 4.1 Rigid projectile motion equation

Projectile kinetic energy change rate during penetration is divided into two categories:

1. Energy, $E_s$, is transferred to target through projectile-target contact area, such as wave energy, elastic and plastic deformation energy.
2. Energy, $E_f$, is transferred to heat through friction on the contact area between projectile and target.

Projectile energy budget during penetration is written as

$$\frac{dE_p}{dt} = -(\frac{dE_f}{dt} + \frac{dE_s}{dt}), \tag{4.1}$$

where $E_p$ is projectile energy at time $t$. It is given by

$$E_p = \frac{1}{2}mv^2(t), \tag{4.2}$$

where $m$ is projectile mass and $v(t)$ is projectile velocity at time $t$. Therefore, the projectile energy change rate is

$$\frac{dE_p}{dt} = mv(t)\frac{dv(t)}{dt}. \tag{4.3}$$

The energy transferring rate into target is estimated using

$$\frac{dE_s}{dt} = \int_{S(t)} \sigma_n(t)v_n(t)ds, \tag{4.4}$$

where $S(t)$ is the contact area between projectile and target, $\sigma_n(t)$ is normal pressure acting on projectile surface and $v_n(t)$ is particle velocity normal to projectile surface. The rate of energy transferred into heat due to friction is

$$\frac{dE_f}{dt} = \int_{S(t)} v_t(t)\sigma_n(t)\eta ds, \tag{4.5}$$

where $\eta$ is friction coefficient and $v_t$ is the velocity tangent to projectile surface at time t.

Using Eqs.(4.3), (4.4) and (4.5), Eq.(4.1) is rewritten as

$$mv(t)\frac{dv(t)}{dt} = -\int_{S(t)} \sigma_n(t)(v_n(t) + v_t(t)\eta)ds. \tag{4.6}$$

For rigid body penetration, the relative velocity between projectile and target materials is assumed to be only from projectile motion (we do not consider shear flow in target materials due to plastic deformation). When a conical projectile penetrates into target materials, the relative velocities on the conical area between projectile and target materials are

$$v_n(t) = v(t)\sin\theta, \tag{4.7}$$

$$v_t = v(t)\cos\theta, \tag{4.8}$$

where $\theta$ is cone half angle. Relative velocities on projectile shank surface are

$$v_n(t) = 0, \tag{4.9}$$

$$v_t = v(t). \tag{4.10}$$

Then, Eq.(4.6) is simplified to

$$m\frac{dv(t)}{dt} = -(\int_{S_l(t)} \sigma_n(t)\eta ds + \int_{S_h(t)} \sigma_n(t)(\eta\cos\theta + \sin\theta)ds), \tag{4.11}$$

where $S_h(t)$ is the contact area between projectile head and target, and $S_l(t)$ is the contact area between projectile shank and target. Approximately, we assume that $\sigma_n(t)$ and $\eta$ are constant on $S_h(t)$, then,

$$m\frac{dv(t)}{dt} = -(\int_{S_l(t)} \sigma_n(t)\eta ds + S_h(t)\sigma_n(t)(\eta\cos\theta + \sin\theta)). \tag{4.12}$$

In order to solve Eq. (4.12) for penetration parameters, the models for $S_l(t)$, $S_h(t)$, $\eta$ and $\sigma_n(t)$ are needed first.

## 4.2 Parameter models

### 4.2.1 Contact area

Based on the deduced velocity-time history (Figure 3.24), the penetration time history is divided into three stages: the initial penetration stage, the steady penetration stage and the penetration stop stage. The contact area between projectile and target materials in each stage is discussed in the following.

1. Initial penetration stage:

   This stage starts from impact and ends when projectile conical head has penetrated into target. Because the contact area between projectile and target materials increases with penetration depth, total resistance force (deceleration) increases with the depth. For conical projectiles, the contact area, $S_h(t)$, between projectile and target materials is

$$S_h(t) = \pi P^2(t)\frac{\sin(\theta)}{\cos^2(\theta)}, \tag{4.13}$$

where $P(t)$ is penetration depth at time $t$ and $\theta$ is cone half-angle.

2. Steady penetration stage:

After the projectile head is fully embedded into the target material, it is possible that target materials start to contact the projectile lateral surface. Therefore, the total contact area, $S(t)$, is

$$S(t) = S_h + S_l(t), \tag{4.14}$$

where $S_h$ is the whole area of projectile cone head and $S_l(t)$ is the contact area on projectile lateral surface at time $t$. If there is no inertial effects in target materials, $S_l(t)$ is

$$S_l(t) = 2\pi R(P(t) - \frac{R}{\tan(\theta)}), \tag{4.15}$$

where $R/\tan(\theta)$ is projectile cone height. However, as we observed from the recovered projectiles (Figure 3.17), the eroded area on projectile lateral surface is much small than the area given by Eq. (4.15) because eroded length on projectile lateral surface is $< 20$ % of final penetration depth (Figure 3.19). This experimental result means that contact area must be significantly reduced by some dynamic processes. Cavitation process (*Hill* [1980]) is suggested to be the major process that reduces the contact area between projectile and target materials during rigid body penetration. It is defined as that a separation between projectile and target material occurs. Cavitation process is basically

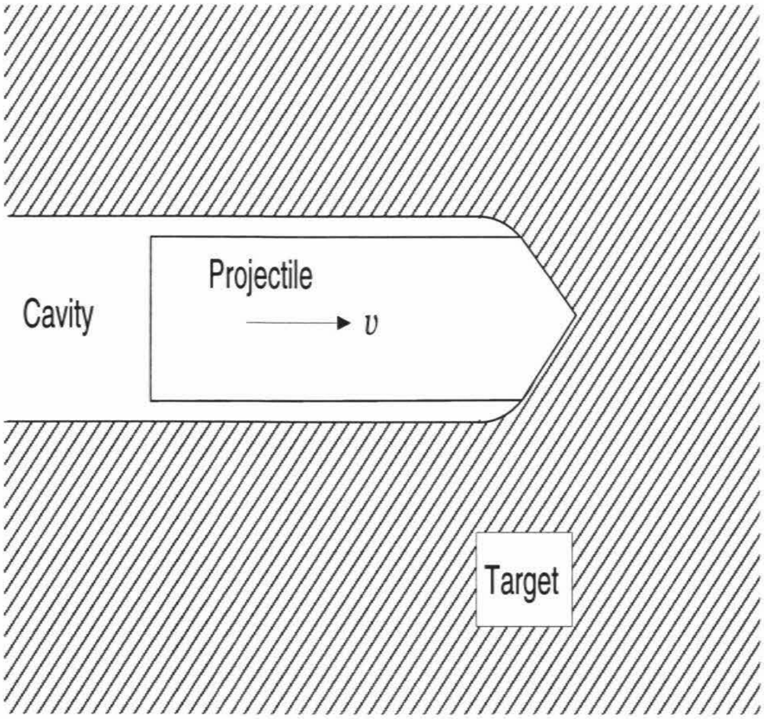

Figure 4.1: Schematics of cavitation process during penetration (after *Hill* [1980]).

due to inertial, plastic deformation and fracture effects (especially fracture that decreases or even diminishes the recovery ability of target material). It depends on impact velocity and projectile head shape. For rigid projectiles with conical head, cavitation only happens at projectile bourrelet. Therefore, we suggest that $S_l = 0$ during steady penetration stage based on present experimental data. Then, the contact area between projectile and target materials is constant as

$$S(t) = S_h = \frac{\pi R^2}{\sin(\theta)}. \tag{4.16}$$

3. Penetration stop stage:

   In this stage, cavitation may be very weak because the penetration velocity is relatively low. Target materials may start to contact projectile on lateral surface. Most of the contact observed on the recovered projectiles may occur in this stage. For the present model, this contact is not considered for simplicity. Therefore, the contact area between projectile and target materials is still given by Eq. (4.16).

### 4.2.2 Friction coefficient

Friction coefficient may be the most difficult parameter to determine because it not only depends on all the parameters involved, e.g., surface time history, slip velocity, normal pressure, surface condition, temperature etc. (*Dieterich* [1967], *Linker and Dieterich* [1992], *Kilgore et al.* [1992], *Chester* [1994], *Scott et al.* [1994], *Tejchman and Wei* [1995], and *Marone* [1998]), but also very limited experimental data are available for the velocity and normal pressure range we are interested in (*Montgomery* [1976], *Forrestal* [1986], and *Forrestal et al.* [1988]). The experimental data under different conditions (slip velocity from $\sim\mu$m/s to $10^2$ m/s, normal pressure $<$ 100 MPa) (*Dieterich* [1967], *Montgomery* [1976], *Kishida and Uesugi* [1987], and *Tejchman and Wei* [1995]) show that the friction coefficient decreases with slip velocity, increases with contact time, and generally decreases with increasing contact surface smoothness.

Basic constitutive relation of friction coefficient (*Linker and Dieterich* [1992]) is

$$\eta(\sigma_n, v_t, T, \varphi) = \eta_0 + \eta_1(\sigma_n, v_t, T, \varphi), \tag{4.17}$$

where $\sigma_n$, $v_t$ and $T$ are normal pressure, slip velocity and temperature, respectively, $\eta_0$ is static friction coefficient, $\eta_1$ is a function of the variables and $\varphi$ (called surface state parameter(*Linker and Dieterich* [1992])) that basically reflects the history-dependence of friction coefficient.

*Montgomery* [1976] found that friction coefficient between metallic materials drops to 0.02 from 0.8 when the product of normal pressure and slip velocity reaches $\sim$ 110 GPa m/s as shown in Figure 4.2 because melting occurs on the interface. Based on limited data, *Forrestal* [1986] suggested that the friction coefficient between steel and porous rocks during penetration is

$$\eta = \begin{cases} \eta_s - (\eta_s - \eta_d)\dfrac{v}{v_d}, & \text{for } v < v_d, \\ \\ \eta_d, \text{ for} & v > v_d, \end{cases} \tag{4.18}$$

where $\eta_s = 0.5$, $\eta_d = 0.08$ and $v_d = 30$ m/s. Later, *Forrestal and Luk* [1992] chose the friction coefficient between steel and aluminum to be from 0.0 to 0.06 during penetration. However, this model does not reflect the effect of surface history on friction coefficient (or surface state parameter, $\varphi$) because friction coefficient depends on not only current slip velocity, but also slip velocity time history (surface condition change, e.g., surface roughness). Experimental data (Table 3.8) show that the roughness on projectile head surface increased with initial penetration velocity. Surface roughness-dependence of friction coefficient has been verified by experimental data (*Tejchman and Wei* [1995] and *Kishida and Uesugi* [1987]) for a system such as steel versus sand. *Tejchman and Wei* [1995] found that friction coefficient between steel and sand increases from $\sim 0.26$ to 1.1 when the normalized roughness changes from smooth to very rough (normalized roughness is defined as the ratio of steel plate surface roughness to mean sand grain size. Surface is smooth, rough, and very rough when the normalized roughness is $< 0.1$, between 0.1 and 0.5, and $> 1.0$, respectively). The reason for discussing the relation between friction coefficient and surface roughness is that projectile head surface roughness changes with initial penetration velocity and penetration depth because of friction heating.

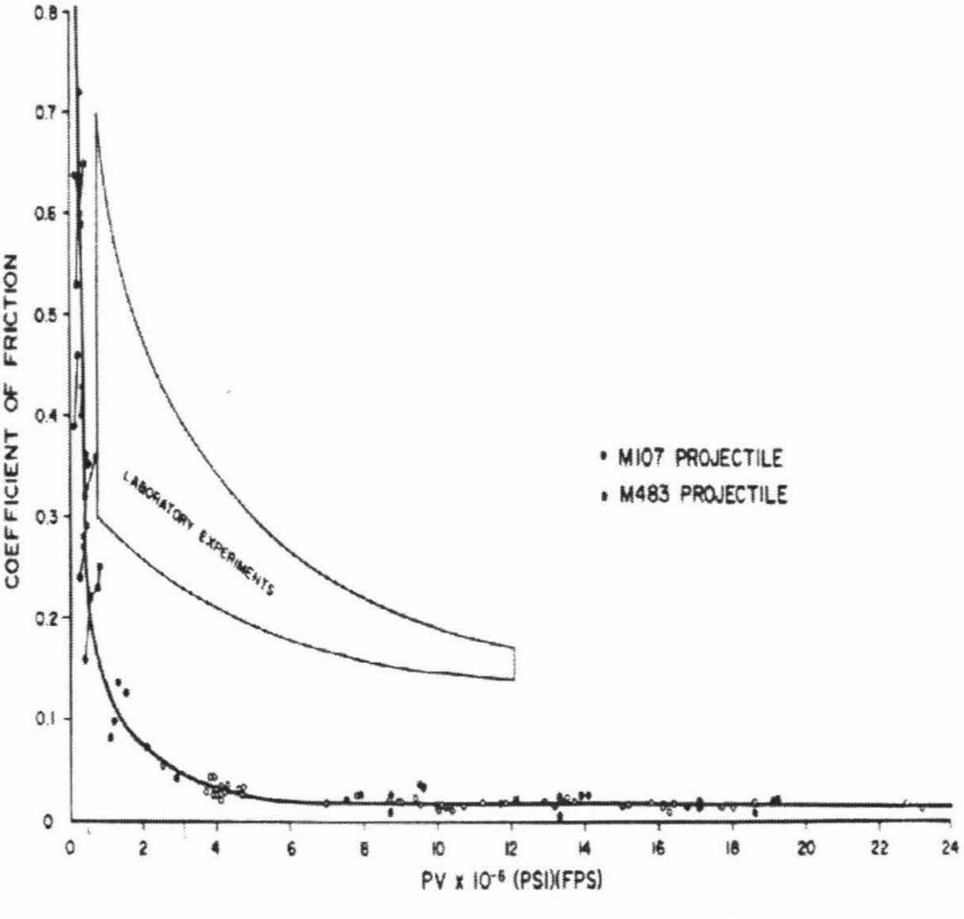

Fig. 4. Coefficient of friction as a function of the product of bearing pressure and sliding velocity for gilding metal rotating bands.

Figure 4.2: Friction coefficient as a function of the product of normal pressure and slip velocity given by *Montgomery* [1976]. Horizontal axis unit is Psi fps.

Based on the discussion above, a model for friction coefficient during rigid body penetration into mortar targets is suggested to be

$$\eta = \begin{cases} \eta_m, & \text{for } v_t(t) > v_m, \\ \dfrac{\eta_m v_s - \eta_s v_m}{v_s - v_m} + \dfrac{\eta_s - \eta_m}{v_s - v_m} v_t(t), & \text{for } v_s < v_t(t) < v_m, \\ \eta_s(v), & \text{for } v_t(t) < v_s, \end{cases} \tag{4.19}$$

where $v_m$ is a critical velocity over which melting occurs on the contact surface melts, $v_s$ is a critical velocity below which no melting occurs on the surface, $\eta_m$ is friction coefficient on melted surface, and $\eta_s$ is friction coefficient on non-melted surface. $\eta_s$ depends on surface history that is affected by initial impact velocity, $v$. When $v_t(t)$ is between the two critical velocities, the projectile surface presumably melts partially. Based on the experimental data given by *Montgomery* [1976] and *Tejchman and Wei* [1995], $\eta_m$ and $\eta_s$ are chosen to be

$$\begin{aligned} \eta_m &= 0.02, \quad \text{for } v_t(t) > v_m, \\ \eta_s &= \begin{cases} 0.2, & \text{for } v\cos(\theta) < v_s, \\ 0.4, & \text{for } v_s < v\cos(\theta) < v_m, \\ 0.9 & \text{for } v\cos(\theta) > v_m. \end{cases} \end{aligned} \tag{4.20}$$

In order to determine $v_m$ and $v_s$, the experimental data on metal-metal interface (Figure (4.2) are assumed to be applicable for for metal-mortar interface. Based on Figure 4.2, full melting occurs when the product of normal pressure and slip velocity is equal to 110 GPa m/s ($5\times10^6$ psi fps), and no melting occurs when the product is 8.8 GPa m/s ($4\times10^5$ psi fps). Then, melting velocity, $v_m$, and no-melting velocity,

$v_s$, are determined to be $\sim$ 180 m/s and $\sim$ 80 m/s using

$$\begin{aligned} \sigma_n v_m &= 110, \quad \text{GPa m/s}, \\ \sigma_n v_s &= 8.8, \quad \text{GPa m/s}, \end{aligned} \tag{4.21}$$

where $\sigma_n$ is estimated using the Hugoniot relation of G-mixture mortar listed in Table 3.5.

### 4.2.3 Stress normal to projectile surface

If we just look at the contact area between projectile and target materials, target material is pushed along the direction normal to projectile surface without considering friction. From impact dynamic point view, penetration history is equivalent to a series of impact events with different velocity. It means that stress normal to projectile surface can be directly and easily estimated using the Hugoniot relation of target material as

$$\sigma_n(t) = \rho_0 D v_n(t), \;\; v_n(t) > v_e, \tag{4.22}$$

where $D$ and $v_e$ are shock wave velocity and particle velocity at the Hugoniot elastic limit of target material, respectively, $v_n(t)$ is particle velocity normal to projectile surface. The relation between penetration velocity, $v(t)$, and $v_n(t)$ is $v_n(t) = v(t)\sin(\theta)$ on the surface of projectile conical head. This assumption is supported by the facts that (1) average pressure acting on projectile during penetration is about 2-4 times higher than the possible highest pressure just due to surface friction and material strength based on the experimental data on both average deceleration and energy needed to create unit penetration volume, and (2) estimated shock wave pressure is very comparable with the average pressure from the experimental data (Figure 3.27).

### 4.2.4 Penetration stop velocity

Because penetration into target materials basically requires a projectile to plastically deform and/or fracture target materials, the pressure acting on target material must not be lower than yield strength of target material. Therefore, resistance pressure acting on a projectile by target material must be larger than the target material yield strength. Thus, the necessary condition for penetration is

$$m|\frac{dv}{dt}| > S_h \sigma_n^y (\eta \cos(\theta) + \sin(\theta)), \tag{4.23}$$

where $\sigma_n^y$ is material yield stress. Based on the model for normal stress given by Eq. (4.22), $\sigma_n^y$ is the Hugoniot elastic limit of the target material. Therefore, the necessary condition for penetration is

$$|\frac{dv}{dt}| > \frac{S_h (\eta \cos(\theta) + \sin(\theta))}{m} \sigma_{hel}. \tag{4.24}$$

## 4.3 Formulation

Based on parameter models given in the previous section, the penetration equation is formulated as

$$
\begin{aligned}
m\frac{dv(t)}{dt} &= -S_h\sigma_n(t)(\eta\cos\theta+\sin\theta), \\
\sigma_n(t) &= \rho_0 D v(t)\sin(\theta), \\
\eta &= \begin{cases} \eta_m, & \text{for } v_t(t) > v_m, \\ \dfrac{\eta_m v_s - \eta_s v_m}{v_s - v_m} + \dfrac{\eta_s - \eta_m}{v_s - v_m} v_t(t), & \text{for } v_s < v_t(t) < v_m, \\ \eta_s(v), & \text{for } v_t(t) < v_s, \end{cases} \\
v_t(t) &= v(t)\cos(\theta),
\end{aligned}
$$

$$
S_h = \begin{cases} \dfrac{\pi\sin(\theta)}{\cos^2(\theta)}P^2, & \text{when } P < R/\tan(\theta), \\ \\ \dfrac{\pi R^2}{\sin(\theta)}, & \text{when } P > R/\tan(\theta), \end{cases} \tag{4.25}
$$

where D is given in Table 3.5, $\eta_m$ and $\eta_s$ are given in Eq. (4.20). $\theta$, $R$, $m$ and $S_h$ are projectile parameters. Therefore, Eq. (4.25) is used to numerically calculate deceleration time history of rigid body penetration into target materials. If the deceleration is known, penetration velocity- and depth-time history can be easily obtained using

$$
\begin{aligned}
v(t) &= v_0 + \int_0^t \frac{dv}{dt}dt, \\
P(t) &= \int_0^t v(t)dt.
\end{aligned} \tag{4.26}
$$

## 4.4 Comparison with experimental data

### 4.4.1 Comparison with present experimental data

Using Eq. (4.25) and the experimental parameters listed in Table 3.7, calculated penetration depth, velocity and deceleration time histories are shown in Figures 4.3 –4.6 in which the experimental data are also given. Based on these figures, we have

1. Penetration depth-time history

   Penetration depth-time histories predicted from the model are in good agreement with the experimental data of Shots P38, 1033, 1034 and in reasonable agreement with the data of Shot 1017. For Shot P38, 1033 and 1034, the predicted penetration depths are larger than the experimental data when the penetration velocity is below $\sim$ 75 m/s. The difference may be caused by the assumption of cavitation when penetration process is close to stop. For Shot 1017, the difference between the predicted and experimental data is relatively larger when the penetration velocity is below 180 m/s.

2. Final penetration depth

   Final penetration depths predicted from the model and measured from the experiments are compared in Figure 4.7. The prediction is in good agreement with the data of the experiments in which targets were intact after impact. The prediction for Shot 1018 is far below the experimental result.

3. Penetration duration

   Predicted penetration duration is shown in Figure 4.8. The predicted penetration duration is in good agreement with the experimental data for Shots P38, 1033, 1034. The predicted time is longer than the experimental data for Shot 1017.

4. Penetration velocity

From Figures 4.3 – 4.6, the predicted velocity time history are in good agreement with the experimental data when velocity is high than 100 m/s for Shots P38, 1033 and 1034, and are generally higher than the that deduced from the experimental data when velocity is below 100 m/s. For Shot 1017, velocity from the experiment is higher than the predicted from $\sim$ 80 to 200 $\mu$s.

5. Penetration acceleration

   The comparison between predicted deceleration time history and the average deceleration in the steady penetration stage shows that they are comparable.

From the agreements between the predicted and the experimental data of penetration depth-, velocity-time history and penetration duration, it is believed that the model suggested here reflects major ongoing physical processes in penetration such as normal stress, cavitation in the beginning of penetration, and stop criterion. The major point we try to make through this simple model is that shock wave generation and cavitation are two major processes that control the energy exchange between projectile and target materials during penetration based on the experimental data. This point is validated by the agreement between the predicted and experimental data in early penetration stage because we have the confidence to say that cavitation occurs in this stage based on present penetration experimental data.

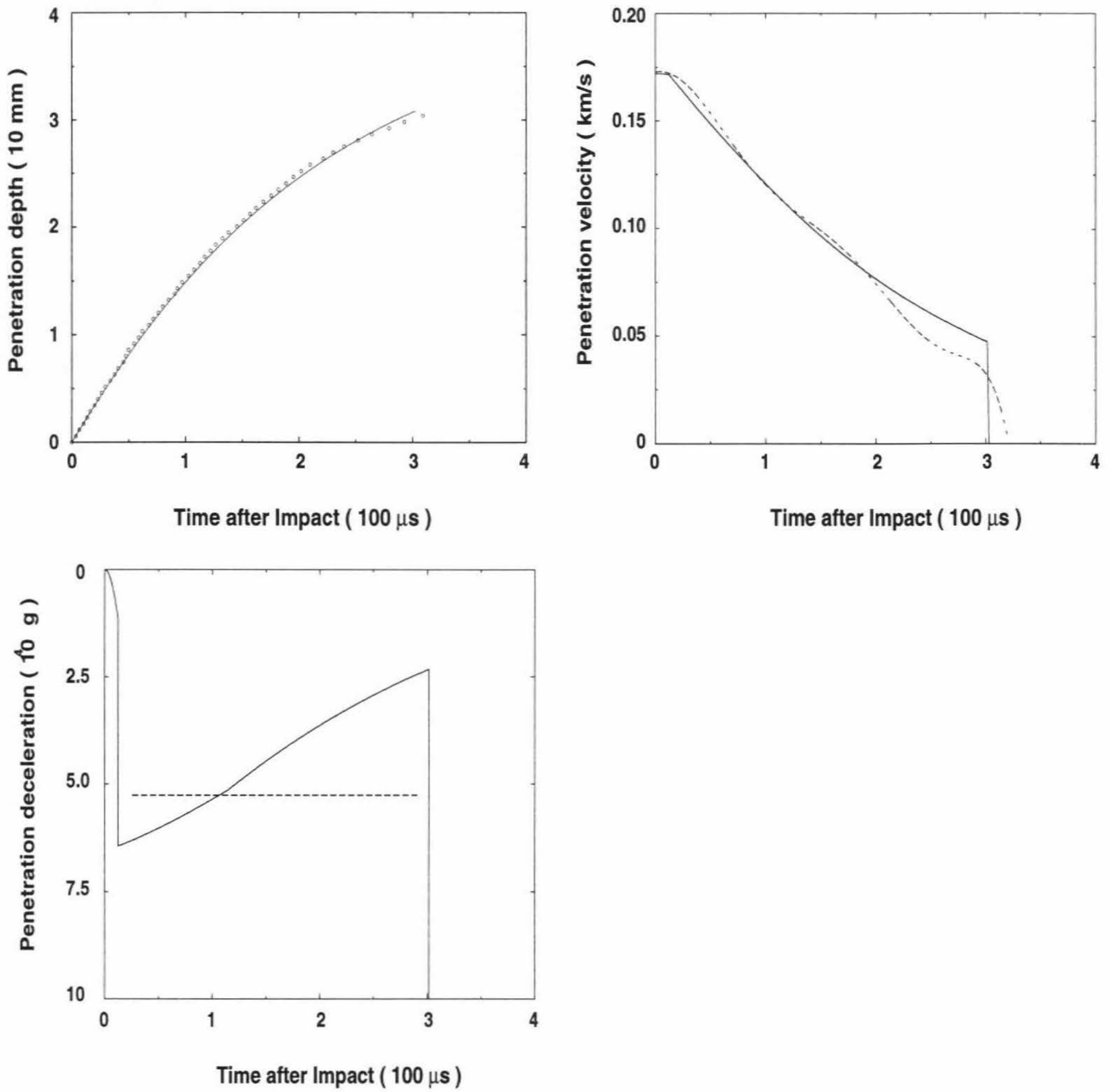

Figure 4.3: Comparison between experimental and predicted results for Shot P38. All solid lines are model prediction. All dashed lines are deduced results from the experimental data. Dashed line in the plot of deceleration versus time is average deceleration deduced from experimental data.

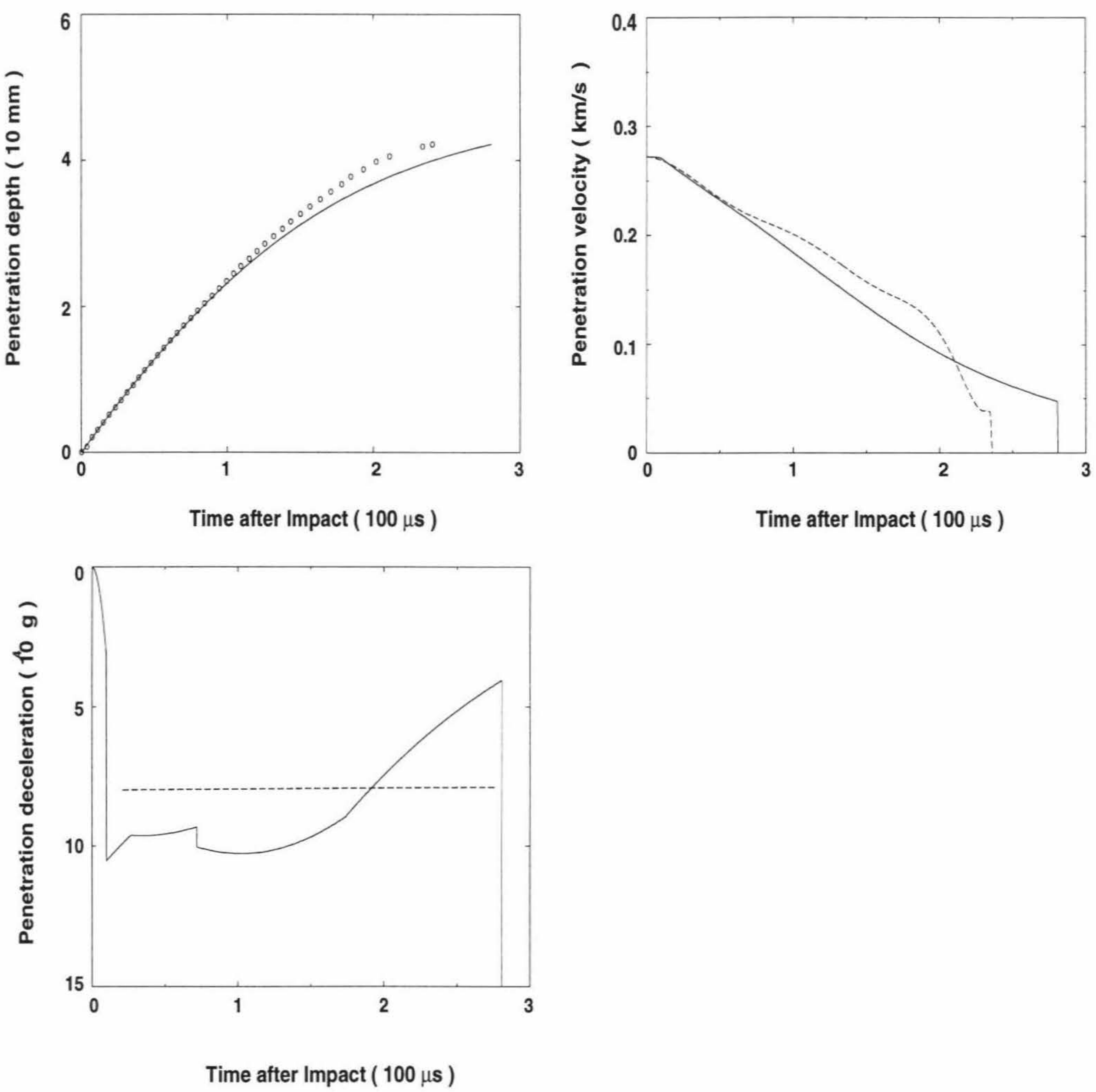

Figure 4.4: Comparison between experimental and predicted results for Shot 1017. All dashed lines are deduced results from the experimental data. Dashed line in the plot of deceleration versus time is average deceleration deduced from experimental data.

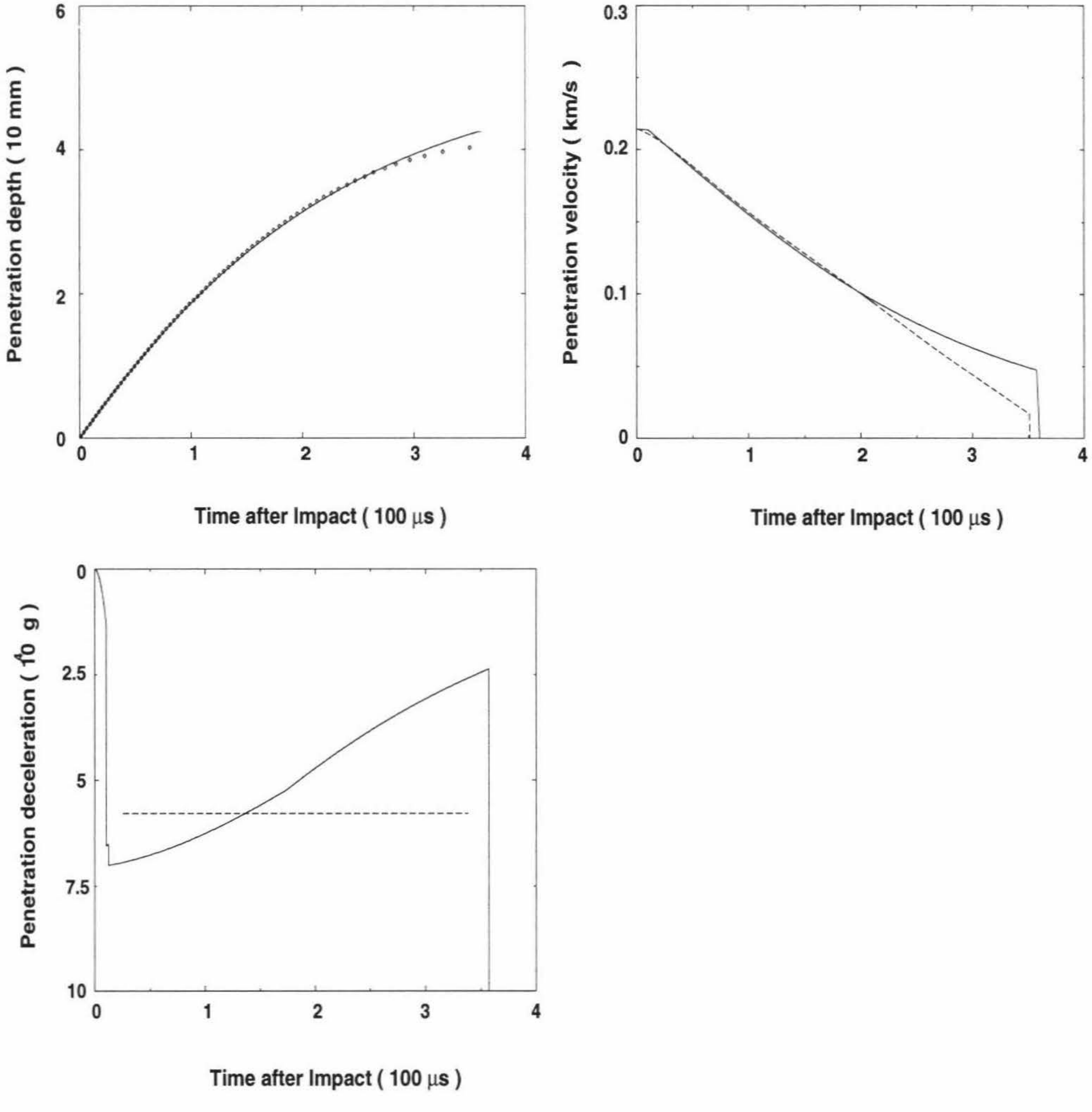

Figure 4.5: Comparison between experimental and predicted results for Shot 1033. All dashed lines are deduced results from the experimental data. Dashed line in the plot of deceleration versus time is average deceleration deduced from experimental data.

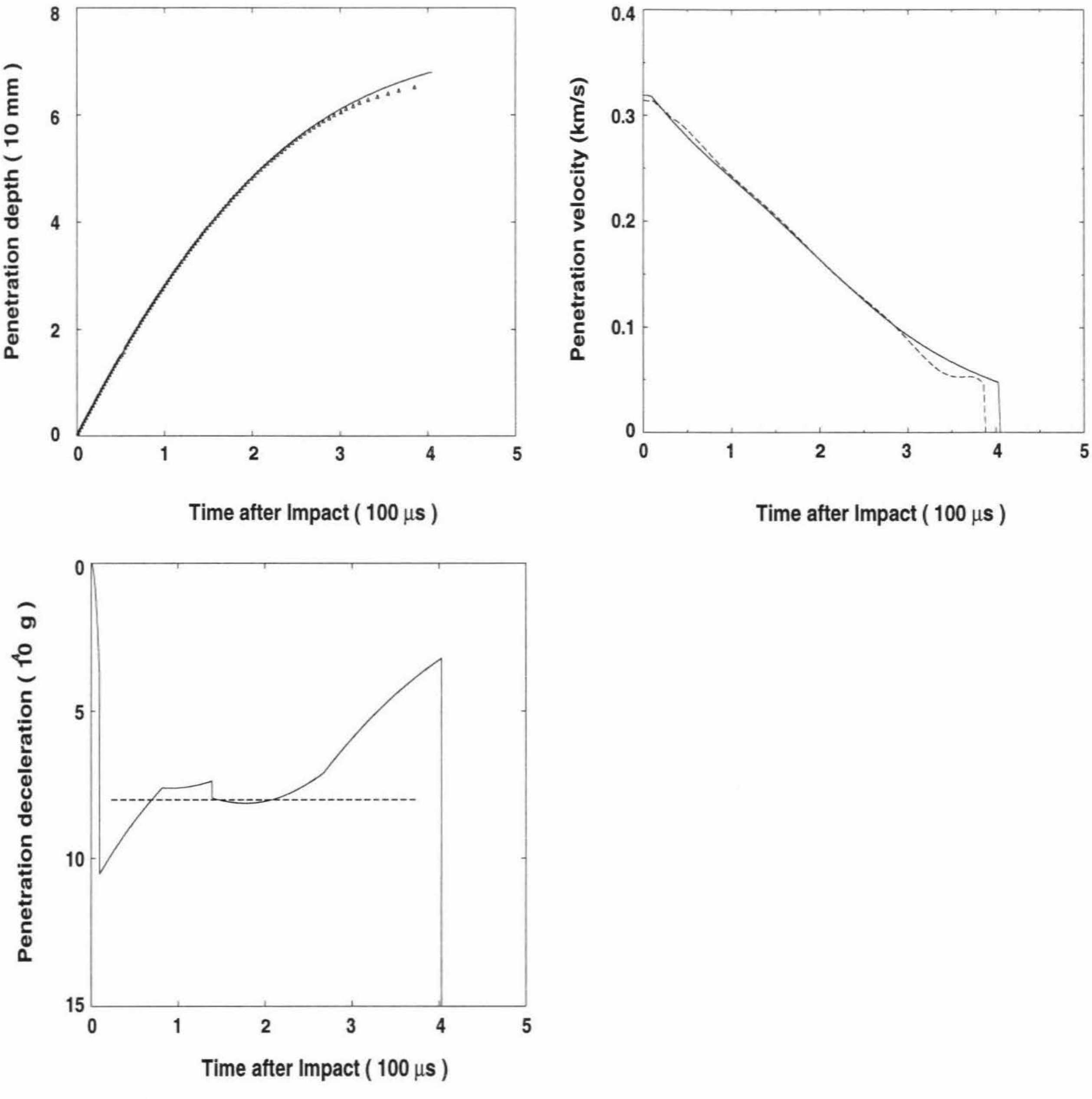

Figure 4.6: Comparison between experimental and predicted results for Shot 1034. All dashed lines are deduced results from the experimental data. Dashed line in the plot of deceleration versus time is average deceleration deduced from experimental data.

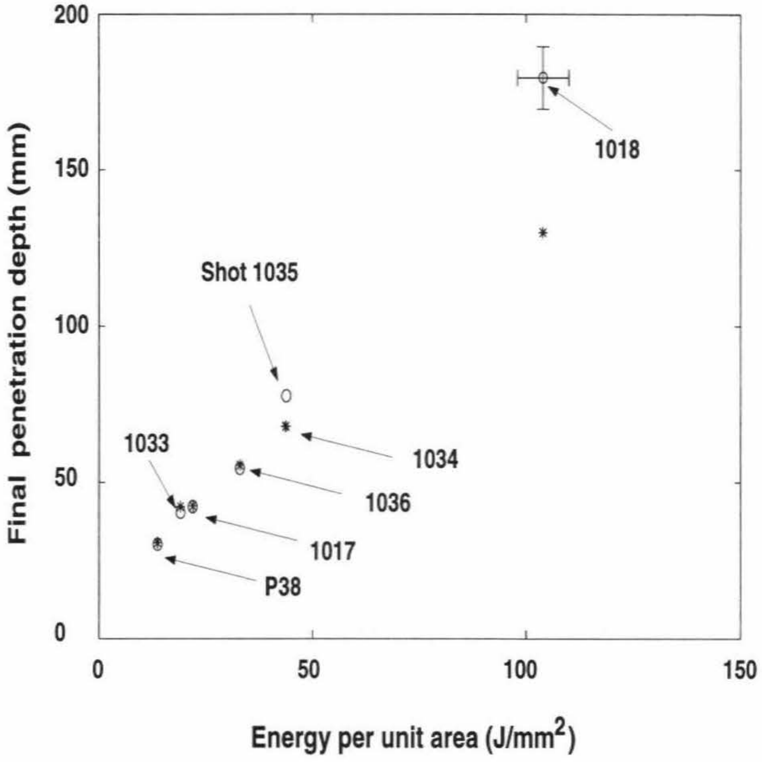

Figure 4.7: Comparison between experimental and predicted penetration depth. Open circles are experimental data. Stars are predicted results.

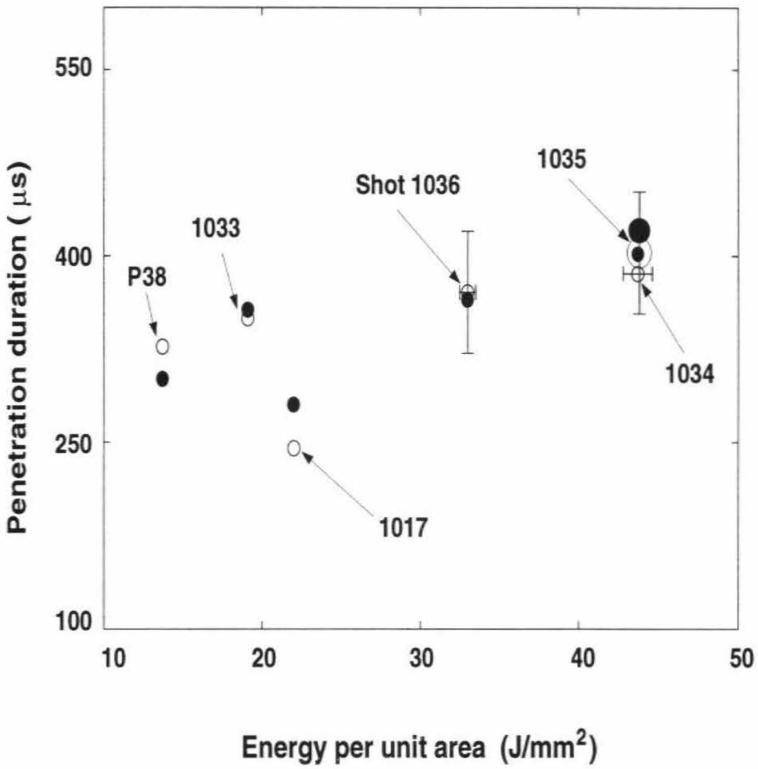

Figure 4.8: Comparison between experimental and predicted penetration duration. Open cycles are experimental data. Filled cycles are predicted results.

## 4.5 Conclusions

Based on the discussion and the first principle model suggested, the main conclusions are

1. A simple analytic model is suggested with the following aspects:
   (a) Friction coefficient during penetration is described by:

$$\eta = \begin{cases} \eta_m, & \text{for } v_t(t) > v_m, \\ \dfrac{\eta_m v_s - \eta_s v_m}{v_s - v_m} + \dfrac{\eta_s - \eta_m}{v_s - v_m} v(t), & \text{for } v_s < v_t(t) < v_m, \\ \eta_s(v), & \text{for } v_t(t) < v_s, \end{cases} \tag{4.27}$$

   where,

$$\eta_m = 0.02, \quad \text{for } v_t(t) > v_m$$

$$\eta_s = \begin{cases} 0.2, & \text{for } v\cos(\theta) < v_s \\ 0.4, & \text{for } v_s < v\cos(\theta) < v_m \\ 0.9, & \text{for } v\cos(\theta) > v_m, \end{cases} \tag{4.28}$$

   where $v_m = 180$ m/s and $v_s = 80$ m/s for rigid body penetration into G-mixture mortar target.

   (b) The minimum penetration velocity is determined by:

$$|\frac{dv}{dt}| > \frac{S_h(\eta\cos(\theta) + \sin(\theta))}{m}\sigma_{hel}. \tag{4.29}$$

(c) The stress normal to projectile surface is given by:

$$\sigma_n(t) = \rho_0 D v(t) \sin(\theta), \quad v(t)\sin(\theta) > v_e. \tag{4.30}$$

(d) Penetration equation is:

$$m\frac{dv(t)}{dt} = -S_h \sigma_n(t)(\eta \cos\theta + \sin\theta), \tag{4.31}$$

$$S_h = \begin{cases} \dfrac{\pi \sin(\theta)}{\cos^2(\theta)} P^2, & \text{when } P < R/\tan(\theta), \\ \\ \dfrac{\pi R^2}{\sin(\theta)}, & \text{when } P > R/\tan(\theta). \end{cases} \tag{4.32}$$

2. Good agreements between the model prediction and present data support the assumptions made in the model. Therefore, it is believed that the model suggested reflects some of major physical processes occurring in penetration, i.e., normal stress, cavitation in earlier penetration process and penetration stop criterion. Specially, shock wave generation and cavitation seem to be two major processes that control the energy exchange between projectile and target materials in early stage of penetration.

# Chapter 5 Summary

In this work, the major progress we made toward the understanding of the physics involved in rigid body penetration into brittle target materials includes:

1. The compressive strength strain rate dependence of the G-mixture mortar is described by

   $$\frac{\sigma_f}{\sigma_f^0} = \exp(0.095(\log(\frac{\dot{\varepsilon}}{\dot{\varepsilon}_0}))^{1.14}), \tag{5.1}$$

   for the strain rates in range of $10^{-7}$/s to $10^3$/s.

2. The non-dispersive Hugoniot elastic wave in the G-mixture has an amplitude of $\sim 0.14$ GPa and a velocity of $\sim 4.3$ km/s. The amplitude of the dispersive elastic wave is about 0.1 GPa under peak shock wave pressure of $\sim 1$ GPa. Experimental data show that the Hugoniot relation of *Read and Maiden* [1971] can be used to approximately describe the G-mixture mortar response to shock loading.

3. Target materials are damaged via compacting in the region in front of penetrators and via brittle radial and lateral cracks propagations in the region surrounding penetration path. Macro-cracks just in front of penetrators as suggested by *Forrestal and Tzou* [1998] and *Bless et al.* [1978] are not produced in the material studied here. Density measurement verifies that target material in front of penetrators was compacted. The results suggest that expected cracks in front of penetrators may be stopped by comminuted region.

4. Radial crack traces on impact surface are very straight along radial from impact site. The number of radial cracks appearing on impact surface is between 4 and 8. Since radial cracks have longer length than lateral cracks, the radial cracks must propagate either faster or be generated earlier than the lateral

cracks. Radial crack length appearing on impact surface is correlated with initial projectile energy.

5. Lateral cracks have circular trace on impact surface. The distance between two adjacent lateral cracks increases with the distance from impact site. Lateral cracks follow a very complex propagation path given by crater profiles. Crack surface morphology looks similar to that of the radial cracks and seems to be tensile cracks. Crater radius induced by lateral cracks is scaled with initial impact velocity and projectile radius. The crater depth is linearly scaled with initial impact energy.

6. Energy needed to create unit penetration volume is found to be increase with impact velocity or penetration depth for the experiments in which targets were still intact after impact. Based on average value of energy per unit penetration volume, average pressure acting on target material during penetration is found to be 10 to 20 times higher than that due to strength of target materials under quasi-static loading and 3 to 4 times higher than the possible highest pressure due to friction, material strength and its rate dependence. This result also suggests that shock wave generation may be dominant process during penetration.

7. The interaction between cracks and target free surface significantly affects rigid body penetration into brittle materials based on present data. The experimental results show that the upper velocity limit for the mortar target with 500 mm diameter and 400/600 mm length is about 350 m/s when projectiles have a 10 mm diameter and an 150 mm length, 280 m/s when projectiles have a 15 mm diameter and an 150 mm length if effect induced by interaction between cracks and lateral free surface is avoided.

8. Aggregate erosion on projectile lateral surface is $< 20$ % of final penetration depth. This result suggests that lateral friction effect on penetration process can be approximately ignored, and shows the difficulty to employ penetrators

into brittle materials as anchors. The roughness of projectile head surfaces increases with penetration velocity. This reflects friction (temperature) effects on projectile head surface.

9. Final penetration depth, $P_{max}$, is linearly scaled with initial projectile energy per unit cross-section area, $e_s$, for projectiles with same projectile head shape, different length and diameter when targets are intact after impact. Based on the experimental data on the G-mixture mortar targets, the scaling relation is

   $$P_{max} = (1.15 \pm 0.08)e_s + (16.39 \pm 2.17), \tag{5.2}$$

   where $P_{max}$ is in mm and $e_s$ is in J/mm$^2$.

10. For the first time, whole penetration depth-time history was recorded with very dense datum point under $10^5$ g deceleration. The results provided dynamic constrains to theoretic models, specially numerical simulations.

11. Penetration duration, $t_{max}$, is found to scale linearly with $e_s$ for projectiles with same length and different diameters. Based on experimental data, the relation for 150 mm long projectiles with a 10 or 15 mm diameter is

    $$t_{max} = (2.08 \pm 0.25)e_s + (303.64 \pm 8.04), \tag{5.3}$$

    where $t_{max}$ is in $\mu$s and $e_s$ is in J/mm$^2$.

    Based on the facts that $t_{max}$ is not very sensitive to $e_s$ and seems not to depend on projectile radius approximately, and the large difference between the penetration durations of Shots 1017 and 1033, penetration duration dependence on projectile length is believed to be reflected by the large value of the second term in Eq. (5.3). Therefore, penetration duration dependence on projectile length is suggested to be described by

$$t_{max} = (2.08 \pm 0.25)e_s + (349.0 \times m_m \pm 8.04), \tag{5.4}$$

where $m_m = m/(\pi R^2)$. The prediction from this relation is in good agreement with the experimental data under different projectile length.

12. Deduced penetration velocity time histories suggest that whole penetration history is divided into three stages: (1) initial stage in which projectile velocity change is small due to very small contact between projectile and target materials, (2) steady penetration stage in which projectile velocity continues to decrease smoothly, (3) penetration stop stage in which projectile deceleration jump up when velocities is close to a critical value that is ~ 35 m/s from the experiments. Generally, the first and last stages are much shorter than the second.

13. Deduced average deceleration, $\overline{a}$, in the steady penetration stage is found to be linearly proportional to initial impact velocity when projectiles have the same dimensions. Based on the experimental data, $\overline{a}$ is

$$\overline{a} = 192.4v + 1.89 \times 10^4, \tag{5.5}$$

where $\overline{a}$ is in g and $v$ is in m/s. Average pressure acting on target materials during penetration is estimated to be very comparable with shock wave pressure. This result suggests once again that shock wave generation is the dominant process for energy exchanging between projectile and target materials during penetration.

14. The experimental data of penetration depth-time histories suggest that a penetration process similarity between normalized penetration depth, $P/P_{max}$, and

normalized penetration time, $t/t_{max}$, exists. This similarity is obtained to be

$$\frac{P}{P_{max}} = f(\frac{t}{t_{max}}), \tag{5.6}$$

where $f$ is a function of $t/t_{max}$. After $f$ is determined using the penetration depth-time history of the experiments with 150 mm length and 10 mm diameter projectiles, the predicted penetration depth-time history is in good agreement with the experimental data for projectile with 100 mm length and 10 mm diameter in whole penetration process. This similarity also predicts that average deceleration in the steady penetration stage increases with decreasing of projectile length. This is verified by the experimental data.

15. Based on present experimental data and analysis of penetration process, a simple analytic model is suggested for rigid body penetration into brittle materials. The model consists of the models of contact area between projectile and target material, friction coefficient on the contact area, pressure normal to projectile surface, and penetration stop criterion. The penetration-depth time histories predicted from the model are in good agreement with present experimental data. These agreements support that shock wave generation and cavitation are two major processes involved in rigid body penetration.

Important unsolved problems related with rigid body penetrations are

1. Friction coefficient under high normal pressure ($\sim$ kbar) and high slip velocity ($\sim 10^2$ m/s) is still poorly understood and constrained.

2. Related to friction effect during penetration, detail of cavitation process is not known. This process is very important for space missions in which penetrators are used as anchors.

3. Lateral and radial crack formation and propagation are not touched here because they are not only very complex, also we do not have any measuremental

on it. However, they are important for both applications and numerical simulations. Specially for space missions in which penetrators are used as anchors or deploying probes, the maximum depth of lateral cracks and the largest radius of radial cracks induced by penetration are very important because they are related to both data interpretation and safety of landers.

These problems should be investigated in much detail through the combination of experimental measurement, and numerical and analytic simulation.

# Bibliography

Ahrens, T. J., Equation of state, *High-Pressure Shock Compressions of Solids,* edited by J. R. Asay and M. Shahinpoor, published by Springer-Verlag, New York, 75-114, 1993.

Ahrens, T. J., Champollion physical properties probe and sample acquisition and transfer mechanism, *Proposal for Rosetta Mission*, 1995.

Ahrens, T. J. and M. L. Johnson, Shock wave data for minerals, *Rock Physics and Phase Relations*, edited by T. J., Ahrens, published by the American Geophysical Union, 35-44, 1995.

Ahrens, T. J., H. Lower, and P. L. Lagus, Equation of state of forsterite, *J. Geophys. Res.,* 76, 518-528, 1971.

Anderson, W. W., T. J. Ahrens, A. Gibson, R. Scott, and K. Suzuki, Emplacement of penetrators into planetary surfaces, *J. Geophys. Res.*, 101, 21,137-21,149, 1996.

Backman, M. E. and W. Goldsmith, The mechanics of penetration of projectile into targets, *Int. J. Engng. Sci.*, 16, 1-99, 1978.

Boyer, H. E. and T. L. Gall, *Metals Handbook,* published by American Society for Metals, Materials Park, OH, 1985.

Birch, R. S. and N. Jones, Measurement of impact loads using a laser Doppler velocimeter, *J. Mech. Eng. Sci.,* 204, 1-8, 1990.

Bishop, R. F., R. Hill and N. F. Mott, The theory of indentation and hardness tests, *Proc. Phys. Soc.*, 53, 147-155, 1945.

Bless, S. J., J. P. Barber, R. S. Bertke and H. F. Swift, Penetration mechanics of yawed rods, *Int. J. Eng. Sci.,* 16, 829-834, 1978.

Bowden, F. P. and D. Tabor, *The Friction and Lubrication of Solids*, published by Oxford University Press, London, Chapter 22, 1968.

Chang, A. L. and A. M. Rajendran, Novel in-situ ballistic measurements for validation of ceramic constitutive models, *Proceedings of the 14th US Army Symposium on Solid Mechanics,* edited by K. R. Iyer and S. C. Chou, published by Battele Press, Ohio, 99-110, 1996.

Chester, F., Effects of temperature on friction: Constitute equations and experiments with quartz gouge, *J. Geophys. Res.,* 99, 7247-7261, 1994.

Chiang, S., D. B. Marshall and A. G. Evans, The response of solids to elastic/plastic indentation: I. Stresses and residual stresses, *J. Appl. Phys.,* 53, 298-311, 1981.

Chiang, S., D. B. Marshall and A. G. Evans, The response of solids to elastic/plastic indentation: II. Fracture initiation, *J. Appl. Phys.,* 53, 312-317, 1981.

Choi, J. H., C. H. Lee, S. N. Chang and S. K. Moon, Long-rod impact phenomena: Role of wave interaction on crack propagation, *Int. J. Impact Engng.,* 17, 195-204, 1995.

Cook R. and G. Pharr, Direct observation and analysis of indentation cracking in glasses and ceramics, *J. Am. Ceram. Soc.,* 73, 787-817, 1990.

Corbett, G. G, S. R. Reid, and W. Johnson, Impact loading of plates and shells by free-flying projectiles: A review, *Int. J. Impact Engng,* 18, 141-230, 1996.

Dieterich, J., Nucleation and triggering of earthquake slip: effect of periodic stresses, *Tectonophysics,* 144, 127-139, 1987.

Durst, F., A. Melling and J. H. Whitelaw, *Principles and Practice of Laser Doppler Anemometry*, published by Academic Press, New York, 1981.

Forrestal, M. J. and D. B. Longcope, Closed-form solutions for forces on conical-nosed penetrators into geological targets with constant shear strength, *Mech. Mater.*, 1, 285-295, 1982.

Forrestal, M. J., Gas-gun experiments to determine forces on penetrations into geological targets, *J. Appl. Mech., Trans. ASME*, 51 , 602-607, 1984.

Forrestal, M. J., Penetration into dry porous rock, *Int. J. Solids Structure,* 22, 1485-1500, 1986.

Forrestal, M. J., K. Okajima and V. K. Luk, Penetration of 6061-T651 aluminum targets with rigid long rods, *Journal of Applied Mechanics,* 55, 755-760, 1988.

Forrestal, M. J., V. K. Luk and N. S. Brar, Perforation of aluminum armor plates with conical-nose projectiles, *Mechanics of Materials,* 10, 97-105, 1990.

Forrestal, M. J., V. K. Luk, Z. Rosenberg and N. S. Brar, Penetration of 7075-T651 aluminum targets with ogival-nose rods, *Int. J. Solids Structures,* Vol. 29, 1729-1736, 1992.

Forrestal, M. J. and V. K. Luk, Penetration into soil targets, *Int. J. Impact Engng.,* Vol. 12, 427-444, 1992.

Forrestal M. J. and D. Y. Tzou, A spherical cavity-expansion penetration model for concrete targets, to appear in *Int. J. Solids Struct.*, 1998.

Frew, D. J., S. J. Hanchak, M. L. Green, and M. J. Forrestal, Penetration of concrete targets with ogive-nose steel rods, *Int. J. Impact Engng.*, 21, 489-497, 1998.

Gavit, S. A and G. Powell, The new millennium programs Mars microprobe mission, *Acta Astronautic,* 39, 273-280, 1996.

Goldsmith, W., Review non-ideal projectile impact on targets, *Int. J. Impact Engng.*, 22, 101-395, 1999.

Grady, D., Shock and release data for SAC-5 concrete to 25 GPa, Sandia National Laboratories Technical Memorandum-TMDG0595, October, 1995.

Grady, D., private communication, 1998.

Gran, J. K. and D. J. Frew, In-target radial stress measurements from penetration experiments into concrete by ogive-nose steel projectiles, *Int. J. Impact Engng.*, Vol. 19, 715-726, 1997.

Hall, C. A., L. C. Chhabildas and W. D. Reinhart, Shock Hugoniot and release states in concrete mixtures with different aggregate sizes from 3 to 23 GPa, *Proceeding of Conference of the American Physical Society Topical Group on Shock Compression of Condensed Matter,* edited by S. C. Schmidt, D. Dandekar and J. Forbes, published by AIP, New York, 119-122, 1998.

Hanagud, S. and B. Ross, Large deformation, deep penetration theory for a compressible strain-hardening target material, *AIAA Journal*, 9, 905-911, 1971.

Heuze, F. E, An overview of projectile penetration into geological materials, with emphasis on rocks, *Int. J. Rock Mech. Min. Sci. & Geomech. Abstr.*, 27, 1-14, 1990.

Hill, R., *The Mathematical Theory of Plasticity,* published by Oxford University Press, London, 1950.

Hill, R., Cavitation and the influence of handshape in attack of thick targets by non-deforming projectiles, *J. Mech. Phys. Solids*, 28, 249-263, 1980.

Hohler, V. and A. J. Stilp, Long-rod penetration mechanics, *High Velocity Impact Dynamics,* edited by J. A. Zukas, published by John Wiley& Sons, Inc., New York, 321-404, 1990.

Hopkison, B., A method of measuring the pressure produced in the detonation of high explosives or by the impact of bullets, *Phil. Trans. R. Soc.*, A213, 437-456, 1914.

Hopkins, H. G., Dynamic expansion of spherical cavity in metals, *Progress in Solid Mechanics*, edited by R. Hill and I. N. Sneddon, Pergamon Press, Oxford, England, 1960, pp 84-164.

Hunter, S. C. and R. J. M. Crozier, Similarity solution for the rapid uniform expansion of a spherical cavity in a compressible elastic-plastic solid, *Quart. Journ. Mech. and Applied Math.,* XXI, 467-486, 1968.

Johnson, K. L., *Contact Mechanics*, published by Cambridge University Press, New York, 1989.

Kirchner H. P. and T. J. Larchuk, Comparisons of static and impact loading damage in Zinc Sulfide, *J. Am. Ceram. Soc.,* 65, 506-510, 1982.

Kishida, H. and M. Uesugi, Tests of the interface between sand and steel in the simple shear apparatus, *Geotechnique*, 37, 45-52, 1987.

Kilgore, B., M. Blanpied and J. Dieterich, Velocity dependent friction of granite over a wide range of conditions, *Geophys. Res. Lett.,* 20, 903-906, 1993.

Kipp, M. E., L. C. Chhabildas and W. D. Reinhart, Elastic shock response and spall strength of concrete, *Proceeding of Conference of the American Physical Society Topical Group on Shock Compression of Condensed Matter,* edited by S. C. Schmidt, D. Dandekar and J. Forbes, published by AIP, New York, 557-560, 1998.

Levy, N. and W. Goldsmith, Normal impact and perforation of thin plates by hemispherically tipped projectiles, *Int. J. Impact Engng*, 2, 209-229, 1984.

Li Zhaoxia and Yaoping Huang, Effect of strain rate on the compressive strength surface cracking and failure model of mortar, *ACI Material Journal,* 95, 512-518, 1998.

Linker M. F. and J. H. Dieterich, Effects of variable normal stress on rock friction: observations and constitutive equations, *J. Geophys. Res.,* 97, 4923-4940, 1992.

Luk, V. K. and M. J. Forrestal, Penetration into semi-infinite reinforced-concrete targets with spherical and ogival nose projectiles, *Int. J. Impact Engng.*, 6, 291-301, 1987.

Marone, C., Laboratory-derived friction laws and their application to seismic faulting, *Annual Review of Earth and Planetary Sciences*, 16, 643-697, 1998.

Masket, A. V., The measurement of forces resisting armor penetration, *J. Appl. Phys.*, 20, 132-140, 1949.

Masket, A. V., and J. C. Lindsay, Dynamic analysis of ballistic impacts, Progress Report, Ser. II, No. 2, Naval Research Laboratory, Contract N7 28406, 1953.

Marsh, S. P., *LASL shock Hugoniot data*, published by University of California Press, 1980.

Mizutani, H., Lunar interior exploration by Japanese lunar penetrator mission, LUNAR-A, *J. Phys. Earth,* 43, 657-670, 1995.

Montgomery, R. S., Surface melting of rotating bands, *Wear*, 38, 235-246, 1976.

Nicholas, T and A. M. Rajendran, Material characterization at high strain rates, *High Velocity Impact Dynamics,* edited by J. A. Zukas, published by John Wiley&Sons, Inc., 127-296, 1990.

Persson, A., A theoretical and experimental study of rigid projectile penetration mechanics, *Proceedings of Second International Symposium on Ballistics,* Daytona Beach, FL., 1976.

Read, H. E. and C. J. Maiden, The dynamic behavior of concrete, *Systems, Science and Software Topical Report* 3SR-707, 1971.

Recht, R. F., High velocity impact dynamics: analytical modeling of plate penetration dynamics, *High Velocity Impact Dynamics,* edited by J. A. Zukas, published by John Wiley&Sons, Inc., 443-514, 1990.

Ross, C. A., P. Y. Thompson and J. W. Tedesco, Split-Hopkinson pressure-bar test on concrete and mortar in tension and compression, *ACI Materials Journal*, 86, 475-481, 1989.

Rubin, A. M., and T. J. Ahrens, Dynamic tensile failure induced velocity deficits in rock, *Geophys. Res. Lett.,* 18, 219-223, 1991.

Scott, D., C. Marone and C. Sammis, The apparent friction of granular fault gouge in shearer layers, *J. Geophys. Res.*, 99, 7231-7246, 1994.

Stilp, A. J. and V. Hohler, Experimental methods for terminal ballistics and impact physics, *High Velocity Impact Dynamics,* edited by J. A. Zukas, published by John Wiley& Sons, Inc., New York, 515-592, 1990.

Tate, A., A theory for the deceleration of long rods after impact, *J. Mech. Phys. Solids*, 15, 387-399, 1967.

Tejchman, J. and W. Wei, Experimental and numerical study of sand-steel interfaces, *International Journal for Numerical and Analytical Methods in Geomechanics*, 19, 513-536, 1995.

Theodore N. and A. M. Rajendran, Material characterization at high strain rates, *High Velocity Impact Dynamics,* edited by J. A. Zukas, published by John Wiley& Sons, Inc., New York, 127-296, 1990.

Timoshenko, S. and J. Goodier, *Theory of Elasticity*, published by McGraw-Hill Book Company, New York, 1970.

Togami, T. C., W. E. Baker and M. J. Forrestal, A split Hopkinson bar technique to evaluate the performance of accelerometers, *J. of Applied Mechanics,* 63, 353-356, 1996.

Virostek, S. P., J. Dual and W. Goldsmith, Direct force measurement in normal and oblique impact of plates by projectiles, *Int. J. Impact Engng.*, 6, 247-269, 1987.

Wahlstrom, D., Compressive strength of G-mixture mortar and concrete, (letter), 1998.

Walker, J. D. and C. E. Anderson, A time-dependent model for long-rod penetration, *Int. J. Impact Engng,* 16, 19-48, 1995.

Wood, W. and W. Bando, MOU penetrator acceleration data, 1990.

Woodward, R. L., Material failure at high strain rates, *High Velocity Impact Dynamics,* edited by J. A. Zukas, published by John Wiley& Sons, Inc., New York, 65-107, 1990.

Wu E., H. Sheen, Y. Chen and L. Chang, Penetration force measurement of thin plates by laser Doppler anemometry, *Experimental Mechanics,* 34, 93-99, 1994.

Xu, Y., L. M. Keer and V. K. Luk, Elastic-cracked model for penetration into unreinforced concrete targets with ogival nose projectiles, *Int. J. Solids Structures*, Vol. 34, 1479-1491, 1997.

Yankelevsky, D. Z., Cavitation phenomena in soil-projectile interaction, *Int. J. Impact. Engng.,* 3, 167-178, 1985.

Young C. W, Depth prediction for earth penetration projectiles, *Proc. ASCE,* 95 SM3, 803-817, 1969.

Zhu G., W. Goldsmith and C. K. H. Dharan, Penetration of laminated Kevlar by projectiles-I. Experimental Investigation, *Int. J. Solids Structures*, 29, 399-420, 1992.

Zukas, J, A., Introduction to penetration mechanics, *High Velocity Impact Dynamics,* edited by J. A. Zukas, published by John Wiley& Sons, Inc., New York, 128-297, 1990.

Zukas, J, A., Survey of computer codes for impact simulation *High Velocity Impact Dynamics,* edited by J. A. Zukas, published by John Wiley& Sons, Inc., New York, 593-714, 1990.

Zukas, J, A. and W. P. Walters, Analytical models for kinetic energy penetration, *High Velocity Impact Dynamics,* edited by J. A. Zukas, published by John Wiley& Sons, Inc., New York, 405-442, 1990.

# Part II

# Phase Change Effect on Shock Wave Propagation in Vitreous $GeO_2$

# Abstract

Stress wave profiles in vitreous $GeO_2$ were measured using piezoresistance gauges in the pressure range of 5 to 18 GPa under planar plate and spherical projectile impact. Experimental data show that the response of vitreous $GeO_2$ to planar shock loading can be divided into three stages: (1) A ramp elastic precursor has peak amplitude of 4 GPa and peak particle velocity of 333 m/s. Wave velocity decreases from initial longitudinal elastic wave velocity of 3.5 km/s to 2.9 km/s at 4 GPa; (2) A ramp wave with amplitude of 2.11 GPa follows the precursor when peak loading pressure is 8.4 GPa. Wave velocity drops to the value below bulk wave velocity in this stage; (3) A shock wave achieving final shock state forms when peak pressure is $> 6$ GPa. The Hugoniot relation is $D = 0.917 + 1.711u$ (km/s) using present data and the data of *Jackson and Ahrens* [1979] when shock wave pressure is between 6 and 40 GPa for $\rho_0 = 3.655$ g/cm$^3$. Based on the present data, the phase change from 4-fold to 6-fold coordination of $Ge^{+4}$ with $O^{-2}$ in vitreous $GeO_2$ occurs in the pressure range of 4 to 15 ± 1 GPa under planar shock loading. Comparison of the shock loading data for fused $SiO_2$ to that on vitreous $GeO_2$ demonstrates that transformation to the rutile structure in both media are similar. The Hugoniots of vitreous $GeO_2$ and fused $SiO_2$ are found to coincide approximately if pressure in fused $SiO_2$ is scaled by the ratio of fused $SiO_2$ to vitreous $GeO_2$ density. This result, as well as the same structure, provides the basis for considering vitreous $GeO_2$ as an analogous material to fused $SiO_2$ under shock loading. Experimental results from the spherical projectile impact demonstrate: (1) The supported elastic shock in fused $SiO_2$ decays less rapidly than a linear elastic wave when elastic wave stress amplitude is higher than 4 GPa. The supported elastic shock in vitreous $GeO_2$ decays faster than a linear elastic wave; (2) In vitreous $GeO_2$, unsupported shock waves decays with peak pressure in the phase transition range (4 -15 GPa) with propagation distance, $x$, as $\propto 1/\mathrm{x}^{-3.35}$, close to

the prediction of *Chen et al.* [1998]. Based on a simple analysis on spherical wave propagation, we find that the different decay rates of a spherical elastic wave in fused $SiO_2$ and vitreous $GeO_2$ is predictable on the base of the compressibility variation with stress under one-dimensional strain condition in the two materials.

# Chapter 6 Introduction

Research on $GeO_2$ response under shock loading has several applications. The first is that the $Ge^{+4}$ ion transforms from 4 to 6 fold coordination occurring in $GeO_2$ under relatively low pressure may be used to understand phase transitions in silicate minerals and glasses under very high pressure. The second is that the phase transitions effect on shock wave propagation can be used to constrain the initial conditions of giant impact events on the Earth.

The phase transition in $SiO_2$ is important for Earth science as it demonstrates that the $Si^{+4}$ ion transformation from 4 to 6 fold coordination with $O^{-2}$ ion yields a 30 % increase in density. Although the shock-induced transformations were first discussed in the form of the quartz to stishovite transition, the change in coordination of $Si^{+4}$ occurs in all other silicate minerals and glasses as well, hence, shock wave loading is used to deduce the equation of the state of materials deep inside the Earth. The equation of the state of $SiO_2$ has been deduced from numerous studies starting with crystal (quartz) and glass phase (*Wackerle* [1962], *Barker and Hollenbach* [1970], *Marsh* [1980], *Sugiura et al.* [1980], *Grady* [1995], and *Chen et al.* [1998]). However, the dynamic phase transformation pressure range of $SiO_2$ is still not well defined (*Grady* [1998]) because it is difficult to monitor stress wave profiles under the shock wave pressure (up to 40 GPa) in which phase transition is expected to occur in $SiO_2$. In order to investigate phase transition mechanisms in $SiO_2$, it is useful to study the phase transition in $GeO_2$ because it has been recognized that $GeO_2$ displays similar phase change at pressures that are a factor of 2 to 10 lower than the similar transition in silicates (*Itie et al.* [1989], *Itie et al.* [1990]l, *Durben and Wolf* [1991], and *Wolf et al.* [1992]). Previous studies under quasi-static loading show that the coordination of Ge changes from fourfold to sixfold in the pressure range of 5 and 13 GPa from various experimental methods (*in situ* x-ray-absorption spectra(*Itie et al.* [1989]) and

Raman spectra (*Itie et al.* [1990])). These results verify that the structure change in $GeO_2$ and $SiO_2$ is similar under quasi-static loading. Although many previous works on $GeO_2$ under quasi-static loading and $SiO_2$ under shock loading have been published, only two papers (*Jackson and Ahrens* [1979] and *Chen et al.* [1998]) are related with $GeO_2$ response under shock loading. *Jackson and Ahrens* [1979] gave the Hugoniot data for the high-pressure range up to 160 GPa and suggested that both vitreous and rutile phases transform to a common phase under high pressure, which is about 5 percent denser than the rutile-type structure. *Chen et al.* [1998] speculated that vitreous $GeO_2$ undergoes an irreversible phase change when shock wave pressure is higher than 8 GPa based on the comparison between the experimental interface velocity profiles and numerical simulations. However, it is still unclear what actually is the pressure range for the phase change to occur under shock loading and if the response of $GeO_2$ to shock loading is similar to that of $SiO_2$.

Besides military application, shock wave decay rate is an important parameter to understand giant impact effect on materials on the Earth. Research on $GeO_2$ phase transition effect on shock wave decay helps to understand silicate phase transition effect on shock wave decay rate that has not been fully studied (*Ahrens and O'Keefe* [1977] and *Robertson and Grieve* [1977]). Based on the irreversible phase transition model in vitreous $GeO_2$ and a large hysteresis in loading-unloading loop, *Chen et al.* [1998] predicted that shock wave with pressure over 8 GPa decays much faster than shock waves with pressure below 8 GPa. It is important to investigate phase transition effect on shock wave decay rate experimentally.

In order to investigate $GeO_2$ phase transition pressure range, the effect of phase transition on shock wave decay and the similarity between $GeO_2$ and $SiO_2$ responses to shock loading, we conducted a series of planar plate and spherical projectile impact experiments on vitreous $GeO_2$ using Caltech 40 mm powder gun. Piezoresistance stress gauges for planar plate impact experiments and piezoresistance stress-strain gauges for spherical projectile impact experiments were employed to monitor stress-wave profiles in the pressure range of upto 18 GPa.

# Chapter 7 Experimental method

Because stress wave profiles provide dynamical informations on deformation process occurring in materials, such as elastic-plastic deformation, phase change and shock decay, embedded piezoresistance stress gauge method (*Rosenberg et al.* [1980]) was employed to monitor stress wave profiles under two different impact conditions (planar and spherical projectile impact) using Caltech 40 mm powder gun.

## 7.1 Sample preparation

A cylindrical disc (100 mm in diameter and 150 mm height) of bubble-free vitreous $GeO_2$ (Corning, Inc.) was cut into 40x40 mm cubic samples with the thickness ranging from 1.7 to 10 mm. The density is measured to be 3.655 g/cm$^3$. The samples used in the experiments were first polished to within 0.005 mm of uniform thickness. Then, stress gauges mounted on mylar film (0.013 mm thickness) were sandwiched between two samples. Epoxy was used to force air out of the contact surfaces between the gauges or samples and mylar film. After the epoxy cured (typically 24 hours), the whole sample assembly was encapsulated into epoxy as shown in Figure 7.1.

## 7.2 Planar impact

In order to generate uniaxial strain shock wave in $GeO_2$ samples, planar impactor as shown in Figure 7.2 was launched to impact on $GeO_2$ samples. Manganin stress gauges were used to monitor stress wave profiles in $GeO_2$. Manganin stress gauge operates on the principle that manganin resistance is nearly linearly dependent on volume strain. Therefore, stress wave profiles in samples can be measured if the relation between

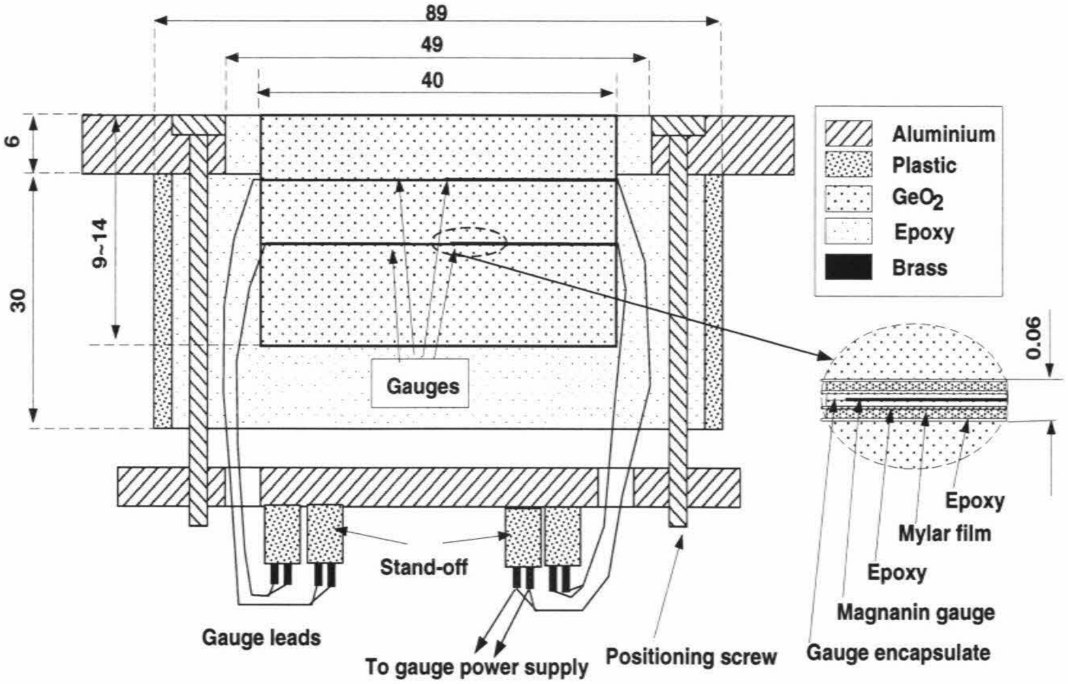

Figure 7.1: Target assembly. All dimensions are in mm.

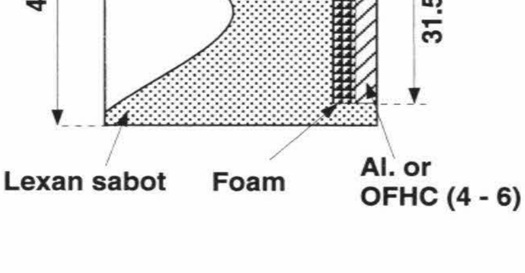

Figure 7.2: Projectile for planar experiment. All dimensions are in mm.

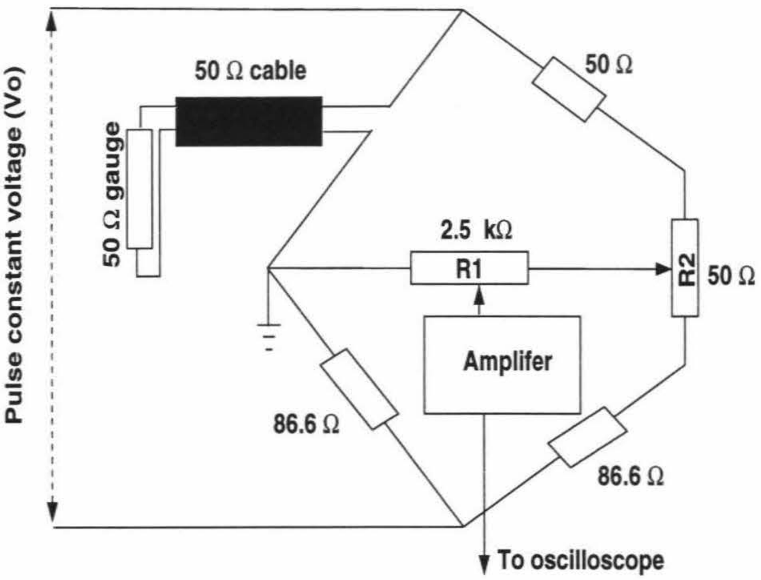

Figure 7.3: Constant voltage method. $R_1$ is used to adjust gain and $R_2$ is used to adjust the bridge balance before measurement.

normal stress and gauge resistance change is known. The way to record stress gauge resistance change is either to use constant current or to use constant voltage circuit method. In this work, we used the constant voltage circuit method as shown in Figure 7.3. A pulse power supply is used to provide a constant voltage to a resistance bridge that consists of a stress gauge and several other resistors. Stress gauge resistance change during shock loading can be deduced from voltage imbalance of the bridge. Therefore, in order to deduce stress wave profile from voltage change of the bridge, we need to know two relations that are (1) the relation between gauge resistance change and voltage output from the bridge and (2) the relation between gauge resistance change and stress change. The relations were obtained experimentally.

Under the assumption that the relation between stress change and gauge resistance change does not depend on sample material, the relation between normal stress, $\sigma(t)$, and manganin stress gauge resistance change, $dR(t)$, was obtained experimentally

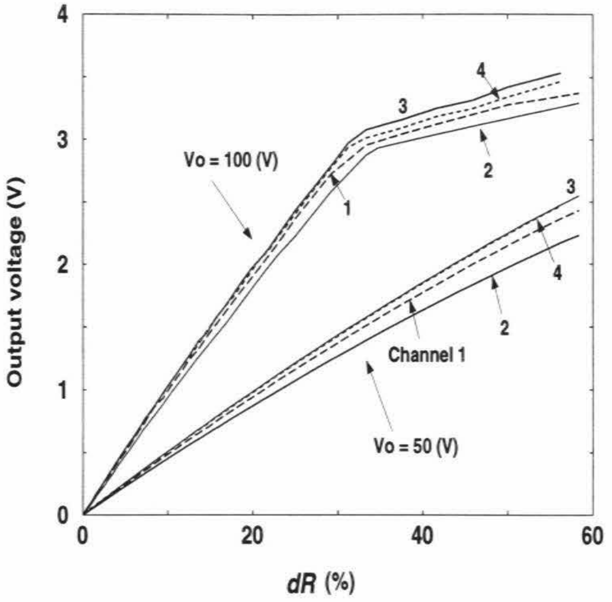

Figure 7.4: Voltage output versus resistance change. $V_0$ is voltage on the bridge. Both 50 and 100 V were used in the experiments.

using impact loading as (*Rosenberg et al.* [1980])

$$\sigma(t) = A_0 + A_1 dR(t) + A_2 dR^2(t) + A_3 dR^3(t) + A_4 dR^4(t), \tag{7.1}$$

where $dR(t) = (R(t) - R_0)/R_0$ ($R(t)$ is gauge resistance at time $t$ and $R_0$ is initial gauge resistance). The $A_i$ are assumed to be constant. When $\sigma \leq 1.5$ GPa, $A_1 = 50$ (GPa) and all the others are zero. When $\sigma \geq 1.5$ GPa, $A_0 = 0.572$ GPa, $A_1 = 29.59$ GPa, $A_2 = 95.20$ GPa, $A_3 = -312.74$ GPa and $A_4 = 331.77$ GPa.

Piezoresistance manganin stress gauge (Mn4-50-EK, Dynasen, Inc.) used in the experiments has initial resistance 50 Ω. Two two-channel power supplies used in the experiments (CK-2, Dynasen, Inc.) with built-in preamplifers can provide a 30 - 300 voltage pulse with a duration of 5 to 1500 μs. The fastest response time of the system including built-in preamplifer and stress gauge is less than 20 ns. The relation between gauge resistance change and voltage output for the two power supplies used in the experiments was calibrated for each channel as given in Figure 7.4.

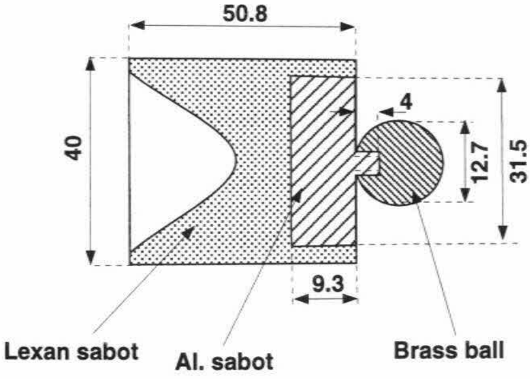

Figure 7.5: Spherical projectile for Shot 1030 and 1031. All dimensions are in mm.

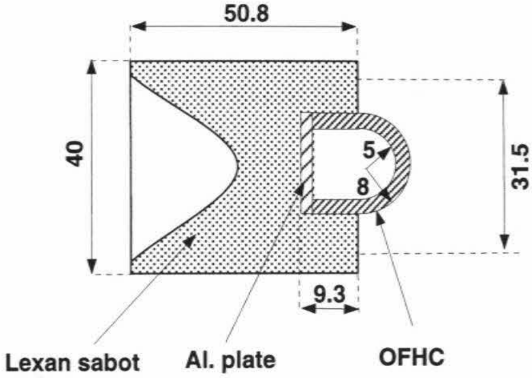

Figure 7.6: Spherical projectile for Shot 1023. All dimensions are in mm.

In each experiment, four stress gauges were used at two interfaces among three $GeO_2$ samples (two gauges at each interface in case one fails during experiments). Digital oscilloscopes (HP54502, HP) were used to record the voltage output from the power supplies.

The procedure to deduce stress wave profiles from recorded voltage profiles is

1. Resistance change percentage of each stress gauge, $dR(t)$, is calculated using the calibrated curve for the channel to power the gauge (Figure 7.4).

2. Stress wave profile is calculated by substituting $dR(t)$ into Eq. (7.1).

### 7.2.1 Spherical projectile impact

In order to investigate phase transition effect on spherical wave propagation, three spherical projectile impact experiments were conducted on vitreous $GeO_2$ (two shots) and fused $SiO_2$. Figure 7.5 shows the drawing of projectiles used for the experiments on vitreous $GeO_2$ and Figure 7.6 is the drawing for the experiment on fused $SiO_2$.

Due to non-planar geometry of shock waves generated by spherical projectile impact, stress gauge resistance change will also include effects from gauge geometry change in addition to resistance change induced by stress normal to gauge as shown in Figure 7.7. In order to deduce stress profile under spherical projectile impact, piezoresistance stress-strain gauges were used to determine stress along impact axis approximately. Stress-strain gauge is the combination of manganin stress and constantan strain gauges that have approximately same geometry. Under non-planar shock wave loading, manganin stress gauge resistance change, $dR_{Mn}$, has two components: one is the resistance change due to stress, $dR_{Mn-stress}$, and the second is the resistance change due to strain along gauge direction, $dR_{Mn-strain}$. However, constantan strain gauge resistance change, $dR_{Cn}$, results only from strain along gauge direction because constantan gauge resistance does not depend on stress approximately. Therefore, strain, $\varepsilon$, along gauge direction is measured by strain gauges as

$$\varepsilon = \frac{dR_{Cn}}{G_{Cn}R_{Cn0}}, \tag{7.2}$$

where $G_{Cn}$ is strain factor of constantan strain gauge and $R_{Cn0}$ is initial strain gauge resistance. If it is assumed that stress gauge resistance change is the linear combination of stress and strain induced resistance changes,

$$dR_{Mn} = dR_{Mn-stress} + dR_{Mn-strain}. \tag{7.3}$$

Then, stress gauge resistance change related to stress is

$$dR_{Mn-stress} = dR_{Mn} - dR_{Mn-strain}. \tag{7.4}$$

Because $dR_{Mn-strain} = G_{Mn}\varepsilon R_0$, Eq. (7.4) becomes

$$dR_{Mn-stress} = dR_{Mn} - G_{Mn}\varepsilon R_0, \tag{7.5}$$

where $G_{Mn}$ is strain factor of manganin stress gauge. $G_{Mn}$ and $G_{Cn}$ are calibrated experimentally to be (Dynasen, Inc.)

$$\begin{aligned} G_{Mn} &= 2.08 - 1.08e^{-0.6\varepsilon}, \\ G_{Cn} &= 2.08. \end{aligned}$$

In each experiment, two piezoresistance stress-strain gauges (Mn/Cn-4-50-ER, Dynasen Inc.) were used to monitor stress wave profiles at two interfaces among three samples under spherical projectile impact. The initial stress and strain gauge resistance is 50 and 47 Ω, respectively. Each stress-strain gauge was powered by one two-channel power supply (CK-2, Dynasen Inc.).

The procedure to deduce stress wave profiles from recorded voltage output (e.g., Figure 7.8) is:

1. $dR_{Mn}$ and $dR_{Cn}$ are calculated using recorded voltage during shock loading and the relation between gauge resistance change and voltage output (Figure 7.4).
2. $\varepsilon$ is calculated using Eq. (7.2) and $dR_{Cn}$.
3. $dR_{Mn-stress}$ is calculated using Eq. (7.5).
4. Stress profile is deduced using Eq. (7.1).

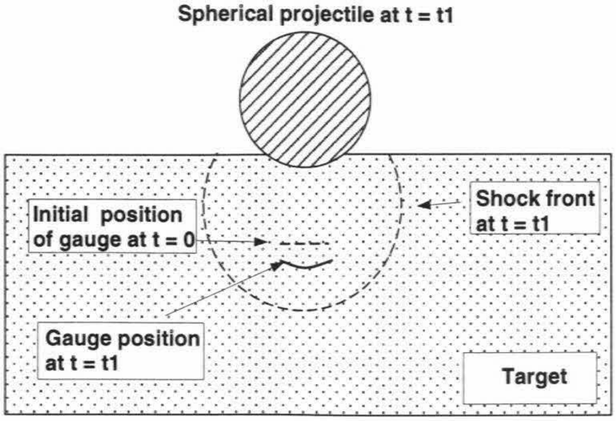

Figure 7.7: Schematic of spherical wave measurement.

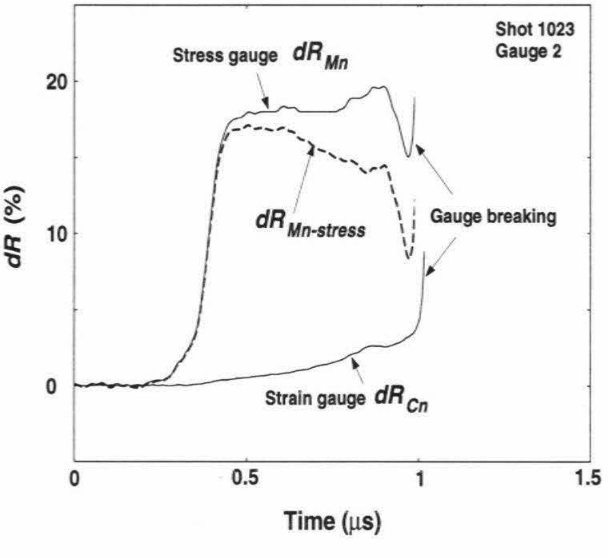

Figure 7.8: Typical recorded stress-strain gauge resistance change profiles.

# Chapter 8 Experimental results

Four planar and three spherical experiments were conducted using the 40 mm powder gun at Caltech. Table 8.1 lists the experimental parameters of the impactor and samples. The experimental results under planar and spherical impact are discussed separately in the following.

## 8.1 Planar impact results

Figure 8.1 shows the stress wave profiles of all the four experiments, where the stress wave profiles deduced are plotted as a function of time. From the stress wave profiles, it is seen that the two stress gauges at same interface gave nearly identical stress wave fronts except Gauges 1 and 2 in Shot 1027, and had a small difference in the peak stress behind the wave front. The difference is believed to be normal for the stress gauge method (*Rosenberg et al.* [1980]). In Shot 1026, the release wave from the impactor back surface also was recoded in all three gauges.

The general features of stress wave profiles in vitreous $GeO_2$ (Figure 8.1) are three wave structures: an elastic precursor with relative long rise time, a ramp wave and then a normal shock wave when the peak stress is $> 6$ GPa. Because each wave is related to a different dynamic process, the parameters of each wave are determined under different approximations as discussed in the following.

1. Elastic precursor parameters

   From the recorded wave profiles, the precursor rise time is very long, approximately 100 and 150 ns at 1.84 and 4.2 mm from impact surface (Figure 8.2), respectively. In order to verify that the long rise time is not the response of the

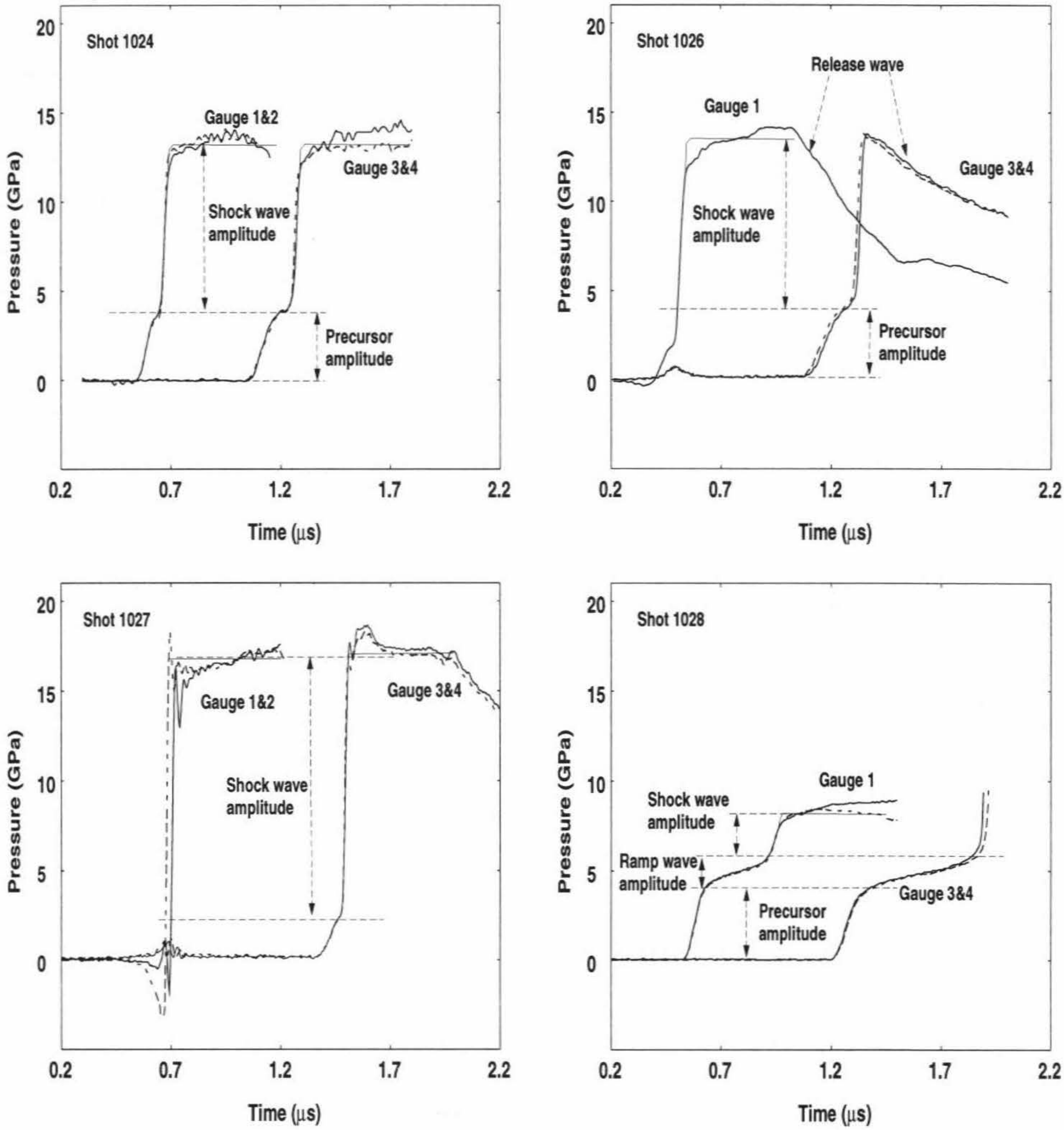

Figure 8.1: Stress wave profiles in vitreous $GeO_2$ under planar impact.

Table 8.1: Experimental parameters.

Planar experiments

| Shot # | Impactor material | Impactor thickness (mm) | Impactor velocity (km/s) | $H_1$ (mm) | $H_2$ (mm) | $H_3$ (mm) |
|---|---|---|---|---|---|---|
| 1024 | OFHC | 5.997±0.001 | 1.547±0.006 | 1.857±0.0041 | 1.745±0.0034 | 10.378 |
| 1026 | 2024 Al. | 4.02±0.001 | 2.062±0.013 | 2.454±0.0021 | 2.238±0.0019 | 5.883 |
| 1027 | 2024 Al. | 6.015±0.005 | 2.310±0.001 | 2.202±0.0038 | 2.588±0.0021 | 6.192 |
| 1028 | 2024 Al. | 6.021±0.0043 | 1.304±0.001 | 1.836±0.004 | 2.360±0.005 | 5.298 |

Spherical experiments

| Shot # | Impactor material | Impactor diameter (mm) | Impactor velocity (km/s) | $H_1$ (mm) | $H_2$ (mm) | $H_3$ (mm) |
|---|---|---|---|---|---|---|
| 1023 | OFHC | 16 | 1.302±0.01 | 6.294±0.009 | 6.462±0.003 | 4.86 |
| 1030 | Brass | 12.722±0.0018 | 1.709±0.006 | 5.408±0.003 | 5.377±0.006 | 5.873 |
| 1031 | Brass | 12.715±0.001 | 1.695±0.011 | 3.312±0.004 | 4.877±0.003 | 5.832 |

$H_1$, $H_2$ and $H_3$ are the thicknesses of three samples in each experiment. Shot 1023 target material is fused $SiO_2$ with initial density 2.203 g/cm$^3$. A 2024 aluminum plate was in front of the target materials of Shot 1023. A 9 mm hemispherical cavity with a depth of 2.5 mm was on the impact surface of the plate.

measurement system including the power supply and the stress gauge, Figure 8.2 provides a comparison among the wave profiles that are aligned with respect to each arrival time. If the long rise time was from the measurement system, it will not depend on the wave propagation distance. However, Figure 8.2 clearly demonstrates that the precursor rise time increases with propagation distance. As a result, we infer that the longitudinal modulus of vitreous $GeO_2$ decreases with increasing stress during precursor wave loading and the precursor in vitreous $GeO_2$ is an elastic ramp wave. Therefore, the whole elastic precursor can not be treated as a single wave with a constant wave velocity.

Because the deformation rate associated with ramp wave loading is lower than that during shock wave loading, ramp wave loading can be approximated as an isentropic process. In addition, since Figure 8.2 demonstrates that the precursor stress does not decay with propagation distance, the phase velocity at constant particle velocity and stress is the same (*Fowles and Williams* [1970]). Therefore, the method of *Fowles and Williams* [1970] is used to determine the precursor parameters. The method basically divides a ramp wave into a series of small stress increments, $\delta\sigma$, and treats each stress increment as a wave with stress jump $\delta\sigma$, particle velocity change $\delta u$, and specific volume change $\delta V$. These parameters for each increment are determined by

$$\delta u = \frac{\delta\sigma}{\rho_0 C_\sigma}, \tag{8.1}$$

$$\delta V = -\frac{\delta u}{\rho_0 C_\sigma}, \tag{8.2}$$

where $\rho_0$ is initial density, and $C_\sigma$ is wave velocity at stress $\sigma$. $C_\sigma$ is given by $(\partial \mathrm{H}/\partial t)_\sigma \approx \mathrm{H}_2/(\mathrm{t}_2\text{-}\mathrm{t}_1)$ in which $\mathrm{H}_2$ is the initial thickness of the sample between the two stress gauges, and $t_2$ and $t_1$ are wave arrival times at the two gauges, respectively. Then the Eulerian wave velocity , $C_e$, is

$$C_e = \rho_0 V C_\sigma, \tag{8.3}$$

where $V$ is specific volume at stress $\sigma$.

Using Eqs. (8.1), (8.2) and (8.3), particle velocity, specific volume and wave velocity along the precursor loading path are determined based on the recoded stress wave profiles from Shots 1024 and 1028 (Gauges 1 and 2 in Shot 1027 and Gauge 1 in Shot 1026 did not response properly during precursor loading). The calculated results are shown in Figures 8.3 and 8.4. The peak stress, wave leading edge velocity and maximum particle velocity of the precursor are summarized in Table 8.2.

2. Ramp plastic wave parameters

From the recorded wave profiles of Shot 1028, uniaxial strain compressibility in the stress range of 4 to 6 GPa increases significantly, and this results in a very dispersive wave. Assuming that the compression in this stress range is isentropic, Eqs. (8.1), (8.2) and (8.3) are used to calculate the parameters related to the ramp wave using the stress wave profiles of Shot 1028. The stress

Table 8.2: Experimental data of elastic precursor in $GeO_2$.

| Shot # | $\sigma_e$ (GPa) | $C_{el}$ (km/s) | $u_e$ (km/s) | $\rho_e$ g/cm$^3$ |
|---|---|---|---|---|
| 1024 | 3.82±0.17 | 3.50±0.09 | 0.315±0.015 | 4.04±0.024 |
| 1026 | 3.95±0.05 | 3.51±0.02 | | |
| 1028 | 4.09±0.11 | 3.51±0.01 | 0.333±0.009 | 4.05±0.01 |

$\sigma_e$ is precursor peak stress. $C_{el}$ is precursor leading edge velocity. $u_e$ is precursor peak particle velocity. $\rho_e$ is the density at $\sigma_e$.

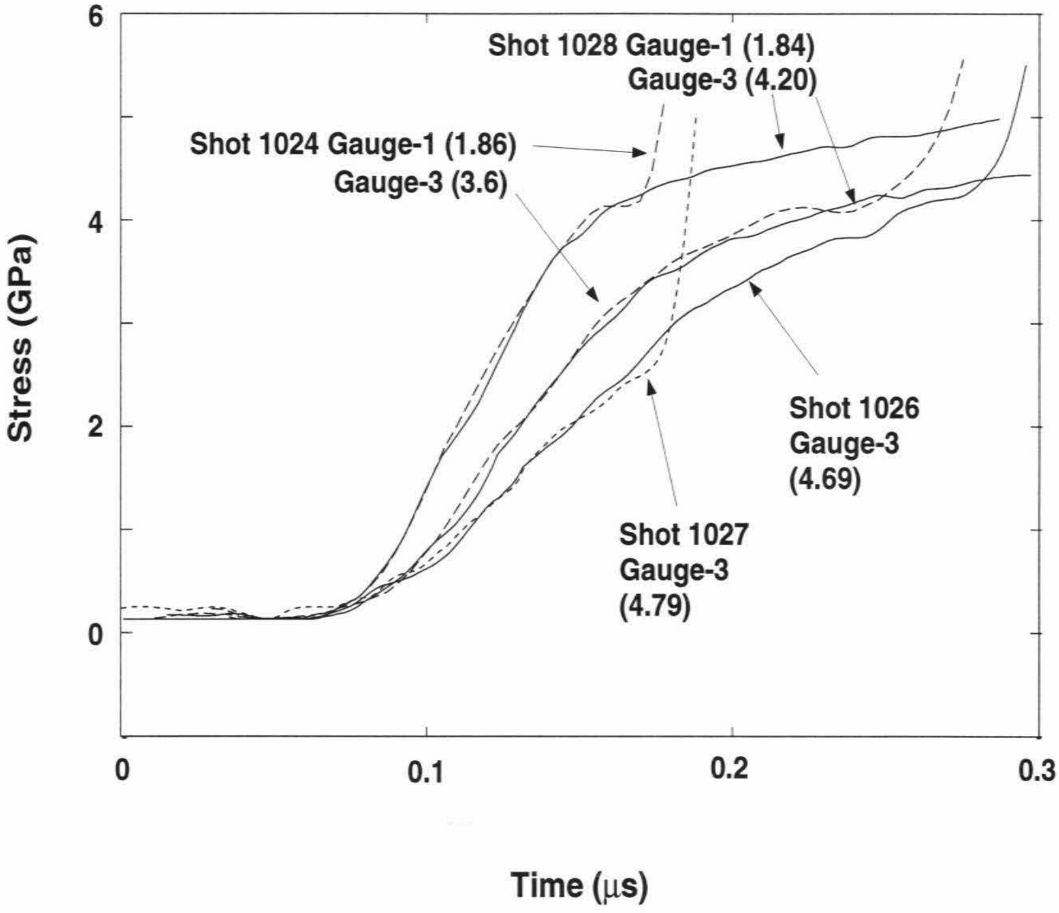

Figure 8.2: Elastic wave front rise time versus propagation distance. The number in brackets is the distance (mm) between gauge and impact surface.

increase cross the ramp wave is 2.1 GPa from the stress profiles. The calculated specific volume decreases from 0.247 to 0.228 $cm^3/g$ (Figure 8.4), and the wave velocity drops to 2.3 from 2.9 km/s and the particle velocity increases from 0.33 to 0.57 km/s (Figure (8.3)).

3. Shock wave parameters

The parameters related to the shock wave that follows the ramp wave are deduced using(*Ahrens* [1992])

$$\begin{aligned} D - u_b &= \frac{H_b}{\Delta t}, \\ u_1 - u_b &= \frac{\sigma_1 - \sigma_b}{\rho_b (D - u_b)}, \\ \frac{\rho_1}{\rho_b} &= \frac{D - u_b}{D - u_1}, \end{aligned} \tag{8.4}$$

where $D$ and $u$ are wave and particle velocity, respectively. $\rho$ is density and $\sigma$ is stress. $H$ is the distance between two gauges. $\Delta t$ is the time between two arrivals of the shock wave front at two gauges. Subscript $b$ and 1 refer to the state before and behind shock wave front, respectively. $(\sigma_1 - \sigma_b)$ is the stress jump cross the shock wave front.

Because release waves from impactor back surface had not taken over shock waves for all the experiments, peak stress in each experiment is assumed to be constant at two stress gauge locations. Therefore, peak stress in each experiment is determined by averaging the peak stress given from all the gauges. The calculated results from the experimental data are listed in Table 8.3 and shown in Figures 8.3 and 8.4. A least square fit was obtained based on present data and the data of *Jackson and Ahrens* [1979]. This fit leads to the Hugoniot relation of vitreous $GeO_2$ in the pressure range of 6 to 40 GPa as

$$D = 0.974 + 1.711u, \qquad \text{for} \;\; u > 0.6 \;\; \text{km/s}, \tag{8.5}$$

Table 8.3: Experimental data of shock wave parameters in $GeO_2$ glass.

| Shot # | $\sigma_1$ (GPa) | $\sigma_1 - \sigma_b$ (GPa) | $D$ (km/s) | $u_1$ (km/s) | $\rho_1$ (gram/cm$^3$) |
|---|---|---|---|---|---|
| 1024 | 13.35±0.28 | 9.24±0.28 | 2.928±0.008 | 1.18±0.029 | 6.089±0.05 |
| 1026 | 13.65±0.39 | 9.24±0.39 | 2.777±0.029 | 1.164±0.048 | 6.386±0.097 |
| 1027 | 17.11±0.76 | 14.49±0.76 | 3.286±0.02 | 1.438±0.072 | 6.401±0.099 |
| 1028 | 8.42±0.25 | 2.27±0.25 | 2.625±0.02 | 0.821±0.027 | 5.088±0.076 |

The errors of $\sigma_1$, $\sigma_1 - \sigma_b$ and $D$ are from the experiments. The errors of $u_1$ and $\rho_1$ are calculated using a formula derived by differentiating Eq. (8.4).

where $D$ and $u$ are both in km/s.

## 8.2 Spherical impact results

Three spherical impact experiments were conducted using 40 mm powder gun at Caltech. Stress wave profiles in fused $SiO_2$ (Shot 1023) and vitreous $GeO_2$ (Shot 1030 and 1031) are shown in Figures 8.5 and 8.6, respectively. Experimental parameters are listed in Table 8.1. The decays of precursor and shock wave amplitude with propagation distance are discussed separately in the following.

1. Precursor decay

   Based on the Hugoniot relations of fused $SiO_2$ and OFHC (*Marsh* [1980]), peak stress at impact surface is calculated to be 11.4 GPa for the experiment on fused $SiO_2$ (Shot 1023). However, the Hugoniot elastic limit (HEL) of fused $SiO_2$ is 9.83 ± 0.24 GPa (*Wackerle* [1962]). Therefore, the wave measured in Shot 1023 is an elastic wave. The elastic wave also is supported because a stress plateau behind wave front appears at both locations (Figure 8.5). Figure 8.7 gives the elastic wave peak stress at each location from the experiment (elastic shock wave peak stress at the impact surface is assumed to be at the HEL). A

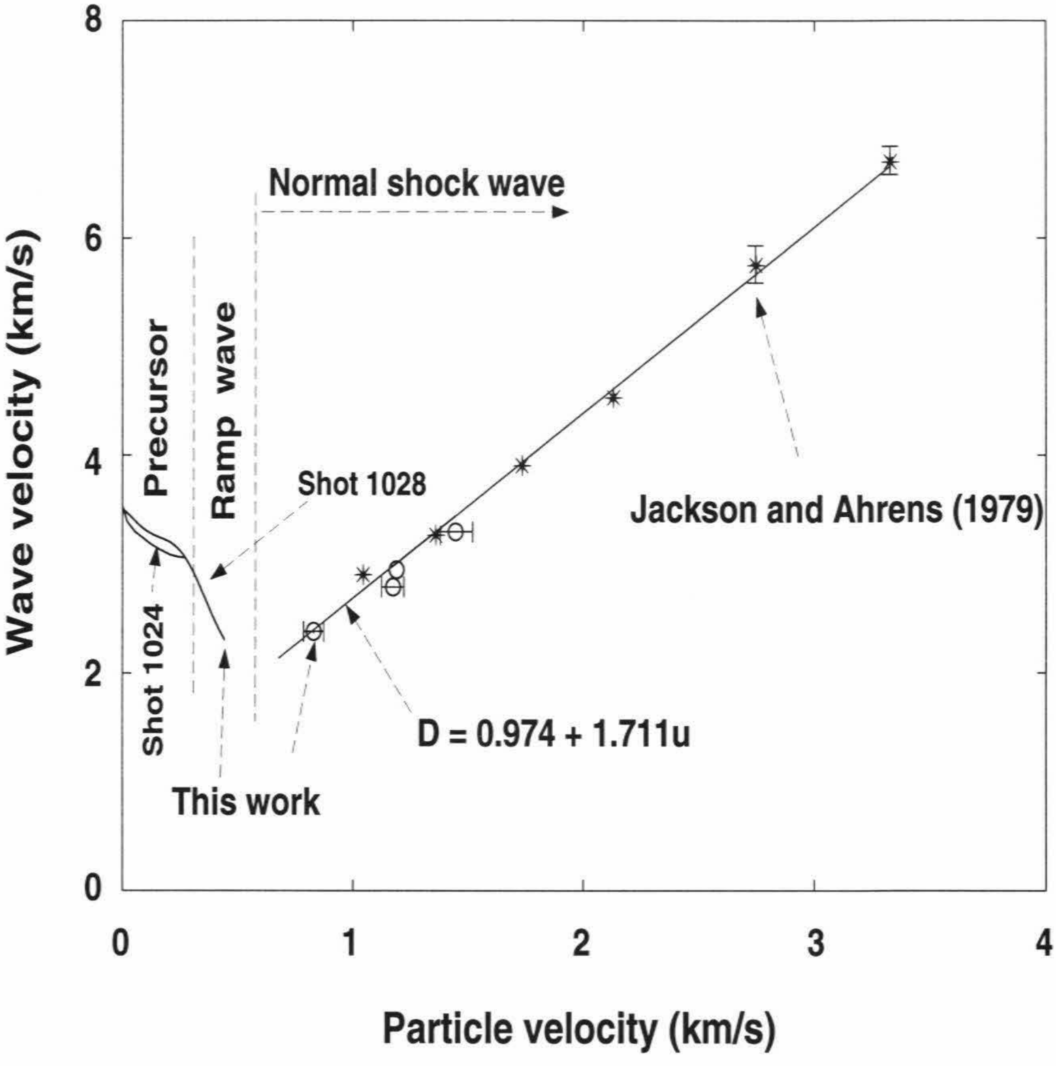

Figure 8.3: Shock wave velocity versus particle velocity.

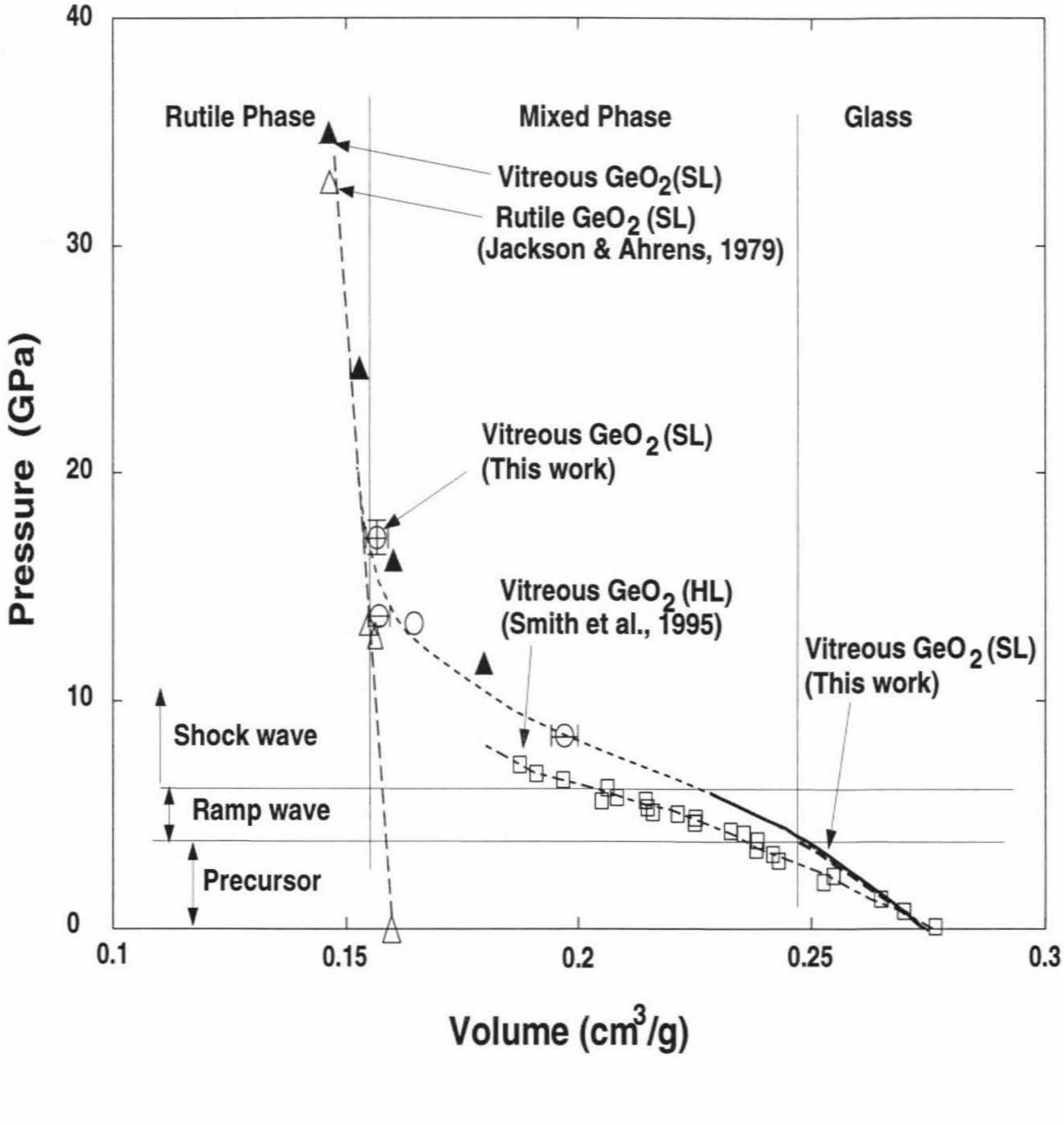

Figure 8.4: Shock pressure versus volume of vitreous $GeO_2$. SL and HL are shock loading and hydrostatic loading, respectively. Light dashed line is schematic.

best fit to the data of $SiO_2$ yields

$$\sigma_x^S = 9.95(\frac{x}{X})^{-0.54}, \tag{8.6}$$

where $\sigma_x^S$ in GPa is elastic wave peak stress at distance $x$ in mm from the center of spherical projectile, and $X$ is spherical projectile radius. Eq. (8.6) means that supported elastic wave in fused $SiO_2$ decays much less rapidly than $(x/X)^{-1}$ which is assumed for a linear spherical elastic wave.

In the case of vitreous $GeO_2$, peak pressure at impact surface is calculated to be 14.6 and 14.4 GPa for Shots 1030 and 1031, respectively, based on Eq. (8.5) and the Hugoniot relation of brass (*Marsh* [1980]). The stress wave profiles in vitreous $GeO_2$ also show a kink at just below precursor limit (indicated by the arrows with the number from 1 to 4 in Figure 8.6). This kink is believed to be remnant of the precursor formed at impact surface. This feature forms only when wave velocity decreases with increasing stress. From present data on vitreous $GeO_2$ under planar impact, wave velocity indeed decreases with increasing stress when peak stress is below 6 GPa. Therefore, stress amplitude at the kinks gives presumably the decay of a supported precursor in vitreous $GeO_2$ (Figure 8.7). A best fit to the data yields

$$\sigma_x^G = 4.06(\frac{x}{X})^{-1.24}, \tag{8.7}$$

where $\sigma_x^G$ in GPa is stress at the kinks. Eq. (8.7) suggests that a supported elastic precursor in vitreous $GeO_2$ decays somewhat faster than $(x/X)^{-1}$ expected for a linear elastic wave.

From the experimental data above, supported elastic precursor in fused $SiO_2$ decays much slower than that in vitreous $GeO_2$. A possible explanation for this result will be discussed later.

2. Shock wave decay

Peak stress at each gauge location is indicated by horizontal dash line in Figure 8.6. The peak stress at the first gauge of Shot 1031 can be easily determined because the gauge recorded the stress clearly. The peak stress for the first gauge in Shot 1030 is less certain because it seems that the gauge was broken just when the stress reached its maximum. In order to see if the second gauge in both shots recorded the maximum stress, we estimate the time, $t_n$, after which no shock wave will arrive at the second gauge. If the possible slowest shock wave velocity, $D_s$, is known, $t_n$ is estimated to be $H_s/D_s$ in which $H_s$ is propagation distance of the shock wave. $D_s$ is estimated using Eq. (8.5) when $u = 0.6$ km/s. $H_s$ is approximated to be $(\mathrm{H}_1+\mathrm{H}_2+u_e t_r/2)$ in which $t_r$ is shown in Figure 8.6, and $u_e$ is the maximum particle velocity of the precursor ($u_e t_r/2$ is due to gauge motion before shock wave arrives at gauge location). The estimated $t_n$ is labeled in Figure 8.6. The above estimation shows that the second gauges recorded the maximum stress.

When peak shock stress is much higher than elastic wave amplitude, peak shock stress decay is described using the form of $(x/X)^\alpha$ in which $x$ is the distance from spherical projectile center and $X$ is spherical projectile radius (*Ahrens and O'Keefe* [1977]). However, when peak shock stress is comparable with elastic wave amplitude, we believe that the form of $A + B(x/X)^\alpha$ is more reasonable because peak precursor stress does not change with propagation distance (shock wave energy is continuously transfered into precursor wave) and only shock wave amplitude decreases with propagation distance. Therefore, the constant $A$ is precursor amplitude and the second term describes the decay of shock wave with propagation distance.

For the present experiment, the form of $A + B(x/X)^\alpha$ is used because the peak stress in the two experiments (Figure 8.8) is very comparable with precursor amplitude. In addition, since the peak shock stress is in the pressure range of phase transition, shock wave decay is more complicated than that arising from geometrical spreading and over taking release wave. Also, $\alpha$ may be a function of propagation distance because the percentage of high density phase after shock wave front depends on peak stress and determines maximum release wave velocity. In order to have an estimate of shock wave decay in the phase transition stress range, $\alpha$ is assumed to be a constant based on the limited experimental data. Then, a best fit to the data of shock wave stress (the difference between the peak stress and the stress just behind the ramp wave) is

$$P = 6.1 + 8.34(\frac{x}{X})^{-3.35}, \tag{8.8}$$

where $P$ in GPa is peak shock stress that is the sum of the precursor, ramp-wave and shock wave amplitudes. The second term in the above expression describes shock wave decay in vitreous $GeO_2$. We should mention here that more experiments are needed to determine $\alpha$ more accurately because Eq. (8.8) is just based on two experimental data points and one calculated point.

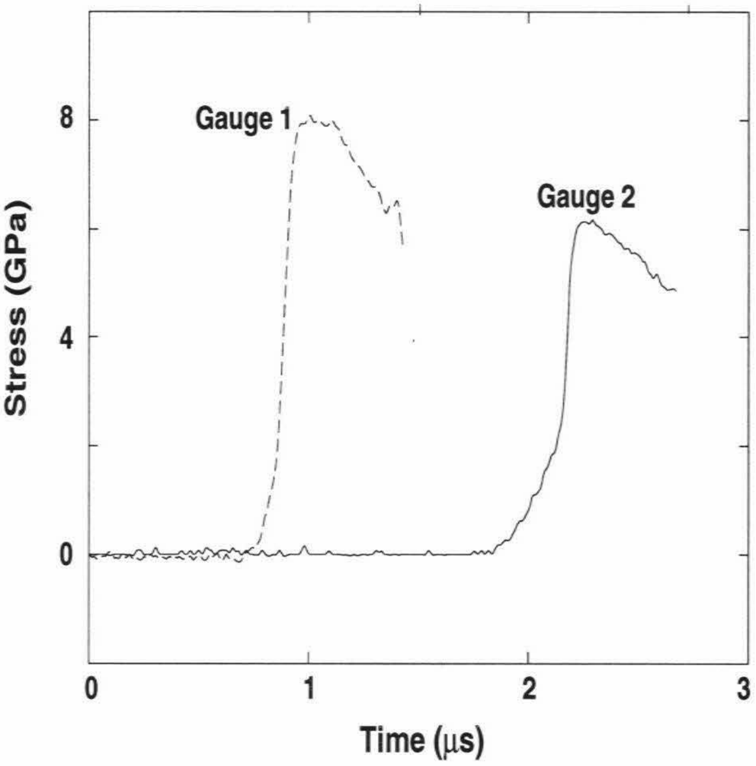

Figure 8.5: Stress-wave profiles in fused $SiO_2$ under spherical impact.

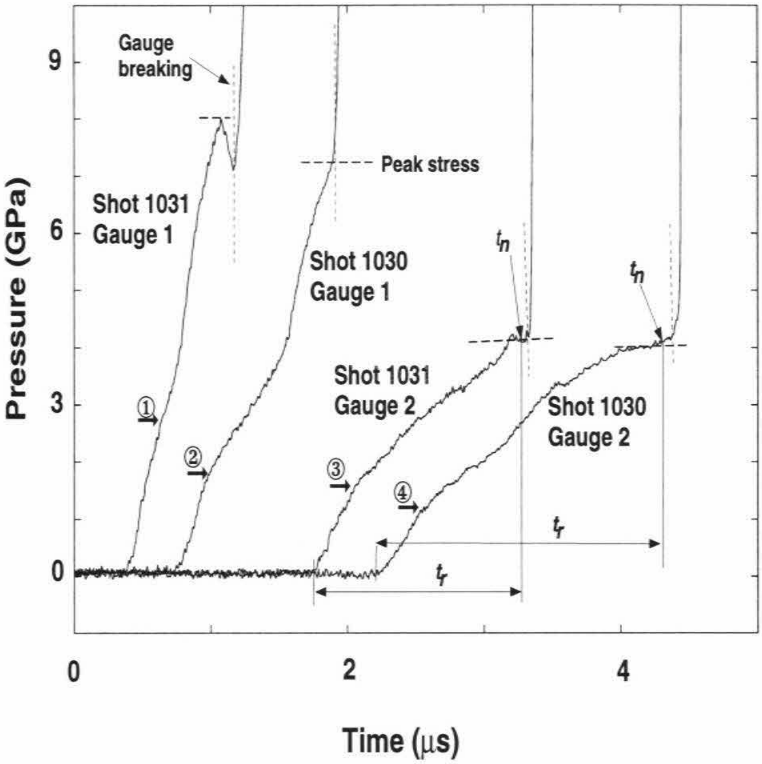

Figure 8.6: Stress-wave profiles in vitreous $GeO_2$ under spherical impact. The four arrows indicate remnant of elastic shock precursor originating from impact surface. $t_r$ is wave rise time used to estimate moving distance of gauge. $t_n$ is the time after which no shock wave will arrive. Horizontal dashed line is peak stress. Vertical dashed line indicates breaking time of gauge.

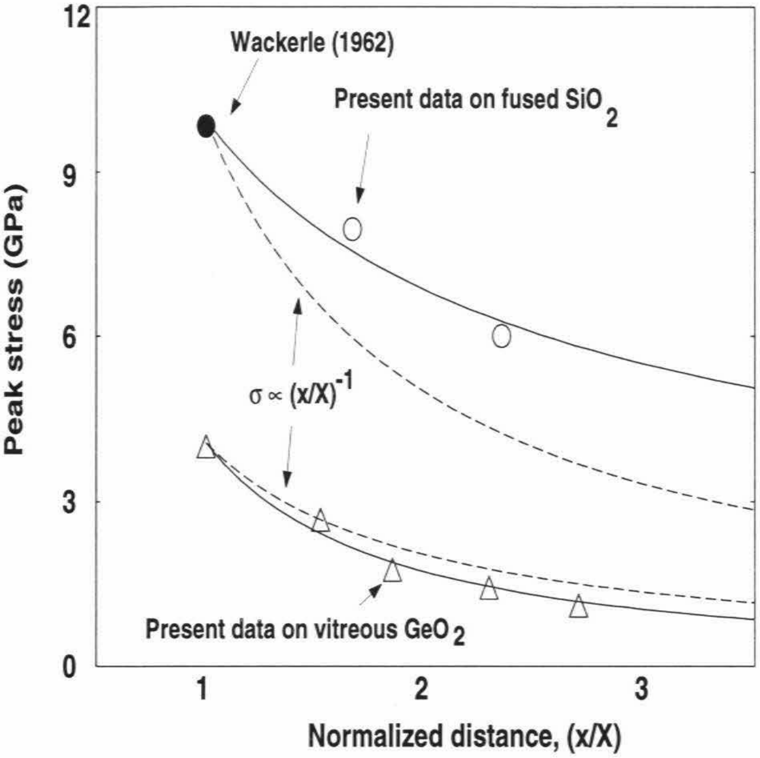

Figure 8.7: Elastic shock wave amplitude versus propagation distance in fused $SiO_2$ and vitreous $GeO_2$ under spherical impact. Solid lines are best fit to the data (Eq. (8.6) for $SiO_2$ and Eq. (8.7) for $GeO_2$). Dashed lines are for linear elastic wave decay.

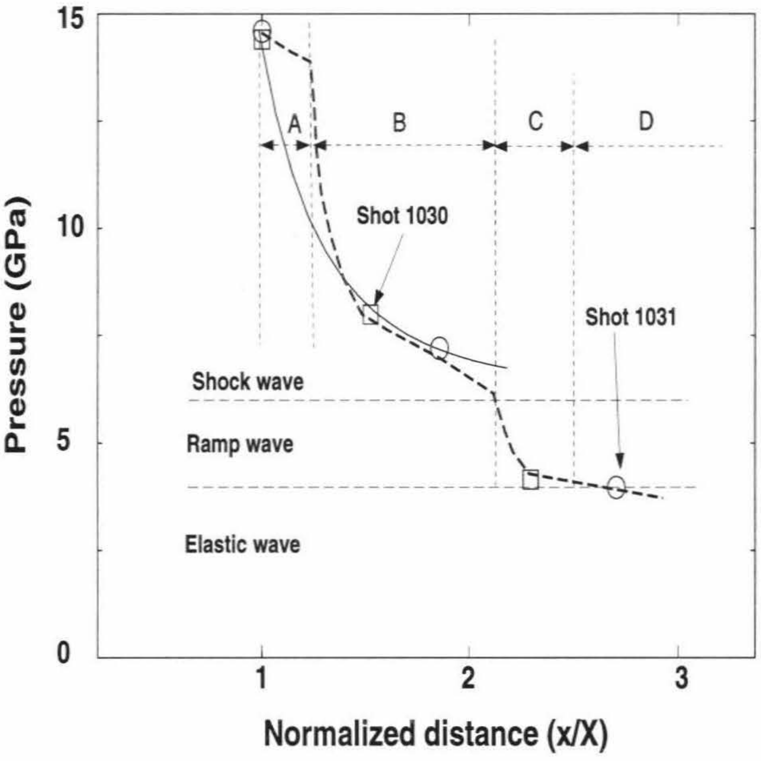

Figure 8.8: Peak shock pressure versus propagation distance in $GeO_2$ under spherical impact. A: near field decay. B: phase transition dominated decay. C: ramp-wave dominated decay. D: elastic wave decay. Solid line is the best fit to the data (Eq. (8.8). Heavy dashed line is schematic.

# Chapter 9 Experimental result analysis

## 9.1 Vitreous $GeO_2$ response to planar impact

Based on the present data as shown in Figure 8.4 in which hydrostatic data (*Smith et al.* [1995]) are also given, the response of vitreous $GeO_2$ under planar shock loading is divided into three stress ranges: 0-4 GPa, 4-6 GPa, and 6 GPa and higher.

When the peak stress is below 4 GPa, the present data show that the wave is a ramp elastic wave because wave velocity decreases with increasing stress. Therefore, the compressibility of vitreous $GeO_2$ increases in this stress range. This is also observed under hydrostatic loading (Figure 9.2) (*Smith et al.* [1995]). The bulk and longitudinal wave velocities of vitreous $GeO_2$ under hydrostatic loading increase slowly with pressure when pressure is below 4 GPa (Figure 9.1). However, the wave velocity under shock loading has a significant drop in this period. When the shock stress is close to 4 GPa, the precursor wave velocity approaches the bulk wave velocity under hydrostatic loading. In general, a ramp wave results from densification processes like cavity collapse, large shear deformation etc. Due to the properties of glass structure (*Scholze* [1991]), it is possible that a large shear stress under shock loading may help glass densification (*Sundaram* [1998]). Therefore, velocity decrease of $GeO_2$ under impact loading may be caused by a densification process induced by shear stress.

When the peak stress is between 4 and 6 GPa, the compressibility increases dramatically under both planar impact and hydrostatic loading as shown in Figure 8.4. *Smith et al.* [1995] found that the deformation is not reversible when pressure is higher than 4 GPa under hydrostatic loading. *Wolf et al.* [1992] noted that heterogeneities with dimensions $< 0.5$ $\mu$m appear in vitreous $GeO_2$ when hydrostatic pressure is $> 4$

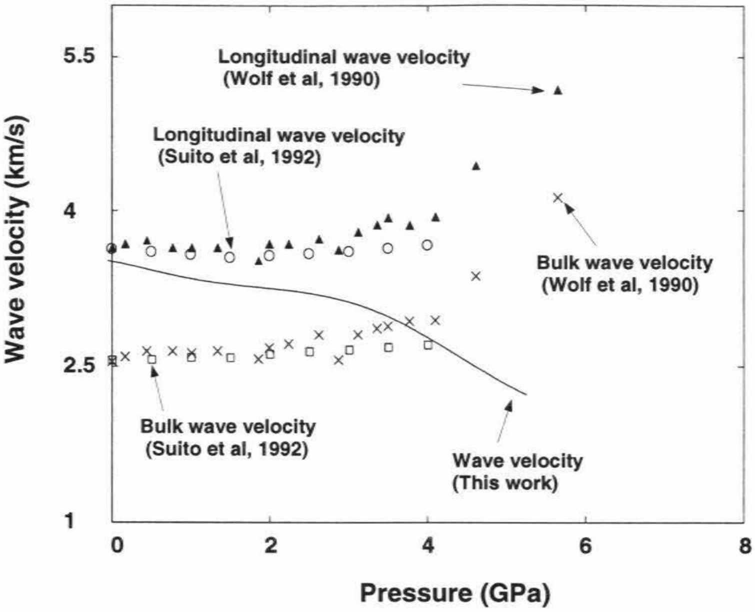

Figure 9.1: Wave velocities versus pressure. The data of *Suito et al.* [1992] and *Wolf et al.* [1992] were obtained ultrasonically and via Brillouin scattering, respectively.

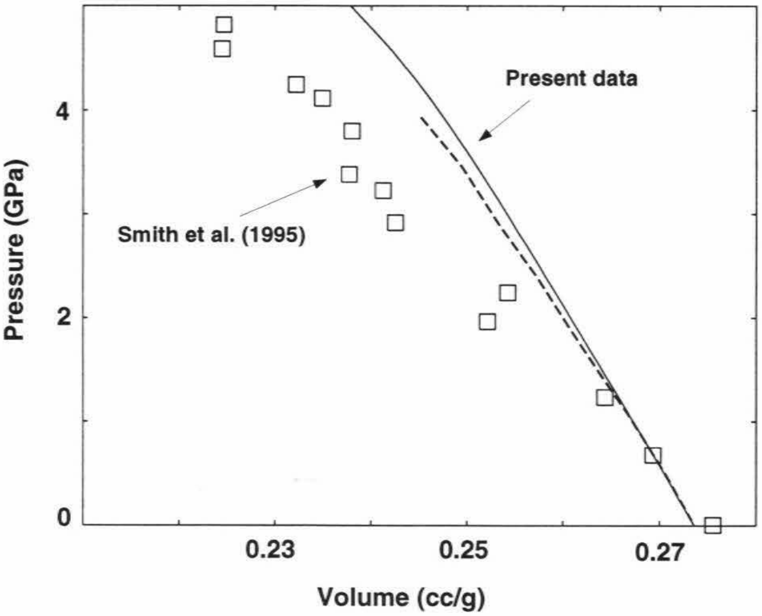

Figure 9.2: Stress versus volume of vitreous $GeO_2$ below 4 GPa.

GPa. He suggested that a new phase (six-fold) starts to nucleate at 4 GPa. *Anan'in et al.* [1974] found that recovered shock fused quartz forms blocks separated by layers of melted quartz when shock pressure is higher than the HEL of quartz. *Grady* [1998] proposed a model to explain the compressibility change in brittle materials when shock stress in brittle materials is higher than the HEL under planar impact loading. The model suggests that the large change of compressibility in brittle materials results from fracture incubation and nucleation, and melting along microfaults under shock loading because of large shear stress. Because phase transition, melting and fracture processes result in compressibility increasing (wave velocity decreasing), it is possible that all the processes may occur in this pressure range.

When peak impact stress is $> 6$ GPa, a normal shock wave forms. Shock wave formation reveals that the compressibility of vitreous $GeO_2$ starts to decrease with stress increasing from 6 GPa. When shock stress is higher than $\sim 15$ GPa, the fact that vitreous $GeO_2$ compression data closely match that of rutile phase $GeO_2$ (*Jackson and Ahrens* [1979]) (Figure 8.4) suggests that the phase transition from 4 fold $GeO_2$ to six fold $GeO_2$ is completed. Therefore, we conclude that the phase transition to rutile phase in vitreous $GeO_2$ starts at about 4 GPa and is completed in the pressure range of 14 to 16 GPa. *Smith et al.* [1995] and *Durben and Wolf* [1991] also inferred that the four-fold to six-fold $GeO_2$ transition occurring between 5.6 and 13 GPa under static loading. Therefore, the data for the phase transition under shock loading is comparable with quasi-static data.

## 9.2 Similarities between $GeO_2$ and $SiO_2$ response under shock loading

Because features in stress wave profiles reveal changes of deformation process during shock loading, it is possible that similarities in wave profile structure and pressure-volume relation appear when several materials have a similar structure. Vitreous

$GeO_2$ has a similar structure to fused $SiO_2$, and approximately also soda-lime glasses (*Scholze* [1991]). Therefore, it is interesting to investigate the shock wave profile and pressure-volume relation similarities among these glasses.

### 9.2.1 Features of stress wave profiles

*Bourne and Rosenberg* [1997] divided soda-lime glass response under planar impact into three stress stages: 0-4 GPa, 4-6 GPa and 6 GPa up based on their experimental data. In addition, their results show that a ramp precursor appears with a maximum stress of 4 GPa and peak particle velocity of 320 m/s in soda-lime glass. *Wackerle* [1962] and *Barker and Hollenbach* [1970] found that shock wave profile in fused $SiO_2$ under shock loading is composed of leading precursor, elastic wave and then shock wave. *Sugiura et al.* [1980] found that stress wave profile in fused $SiO_2$ under shock loading is composed of four waves, i.e., leading precursor, elastic wave, ramp wave and then shock wave. The leading precursor in fused $SiO_2$ is a ramp wave with a amplitude of 4 GPa (*Wackerle* [1962] and *Barker and Hollenbach* [1970]) and peak particle velocity of 340 m/s (*Wackerle* [1962]) and 300 m/s (*Barker and Hollenbach* [1970]). Present results show that the leading ramp precursor in vitreous $GeO_2$ has a amplitude of 4 GPa and particle velocity of 333 m/s. The above experimental data of fused $SiO_2$, vitreous $GeO_2$ and soda-lime glass show that a similarity appears on both stress wave profiles (ramp precursor, ramp wave and shock wave) and on the amplitude and particle velocity of leading precursor ( $\sim$ 4 GPa and $\sim$ 320 m/s in all three glasses). These similarities probably result from very similar deformation process in the materials. The experimental data indicate that the only difference on stress wave profiles is that an elastic wave follows the leading precursor in $SiO_2$ but not in $GeO_2$. This may reflect the effects of the stronger bond in $SiO_2$ (*Itie et al.* [1989]).

### 9.2.2 Similarities of P-V relations

The above wave profile similarity should result in the same features on the relation between pressure and volume. The pressure-volume relation of vitreous $GeO_2$ may be scaled to the relation of fused $SiO_2$ due to the similar structure.

Deformation or phase transition processes in materials are generally finished in shock wave front under planar shock loading because the energy needed for the phase transition or deformation process is only available from the stress gradient or particle velocity gradient in the shock wave front (all particles behind the shock wave front are assumed to propagate at the same velocity along same direction). The energy from the gradients depends on shock wave amplitude, shock wave front width and atomic weight (material density). Here, we simply use the density ratio to scale the pressures in $GeO_2$ and $SiO_2$ as

$$P_G = \frac{P_s \rho_s}{\rho_G}, \tag{9.1}$$

where $\rho_G$ and $\rho_S$ are vitreous $GeO_2$ and fused $SiO_2$ density, respectively. Figure 9.3 shows the comparison between $SiO_2$ and $GeO_2$ pressure-volume relations (P-V) under uniaxial strain impact loading. Both of the P-V plots are aligned at the densities of rutile and vitreous phase horizontally. The pressure axis for $SiO_2$ is scaled down using Eq. (9.1). Figure 9.3 demonstrates a reasonable similarity of P-V relation of fused $SiO_2$ and vitreous $GeO_2$. This similarity means that the response of vitreous $GeO_2$ under relative low shock pressure can be used to analyze the response of fused $SiO_2$ under higher pressure. If the compression similarities of similar structure is a general phenomenon, the present result has useful applications in shock wave studies. It may be that studying of melting and vaporization of a relatively volatile substance could be studied at low pressure and thus could provide a useful analog to a more refractory substance that occupies the same structure at higher shock pressure and temperature.

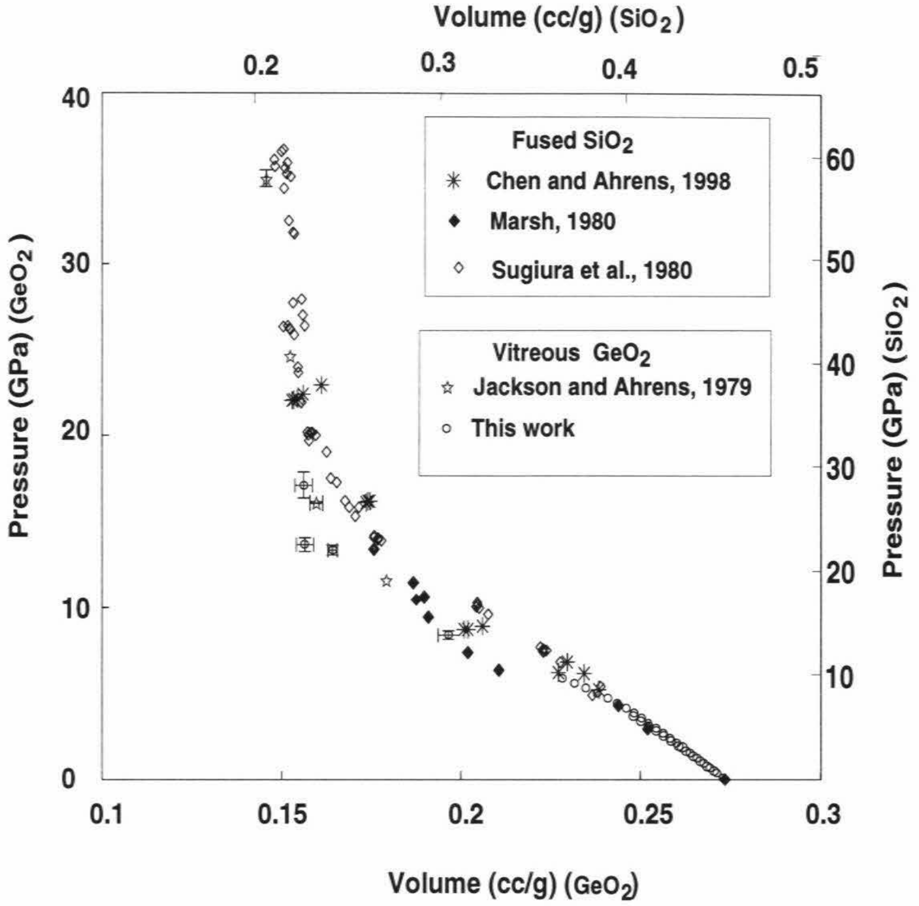

Figure 9.3: Pressure versus volume for vitreous $GeO_2$ and $SiO_2$. The P-V plot for $SiO_2$ is aligned to that the initial volume and the volume for rutile phase with $GeO_2$ along the volume axis. The vertical axis of pressure for $SiO_2$ is scaled down by the ratio of initial $SiO_2$ to $GeO_2$ density.

## 9.3 Shock wave attenuation

### 9.3.1 Elastic wave decay

Two different elastic waves, linear and nonlinear, are defined generally as

$$\frac{\partial C}{\partial \sigma} = 0, \qquad \text{linear elastic wave,} \tag{9.2}$$

$$\frac{\partial C}{\partial \sigma} \neq 0, \qquad \text{nonlinear elastic wave,} \tag{9.3}$$

where $C$ is the longitudinal elastic wave velocity and $\sigma$ is stress.

The elastic wave decay rate depends on both $\partial C/\partial \sigma$ and initial conditions (supported and non-supported). In order to discuss this in detail, we first derive an approximate expression for spherical elastic wave propagation. Assuming that the center of a thin layer spherical wave is at $x$ with stress $\sigma$, the leading and tailing edges of the layer are at $x + \Delta x/2$ and $x - \Delta x/2$ with stress $\sigma + \Delta\sigma/2$ and $\sigma - \Delta\sigma/2$ in which $\Delta\sigma = \sigma(x + \Delta x/2) - \sigma(x - \Delta x/2)$, respectively. When the layer center moves to $x + dx$, the locations of the leading and tailing edges of the layer are at $x_l$ and $x_t$, respectively. Here

$$x_l = x + \Delta x/2 + (C(\sigma) + (\frac{\partial C}{\partial \sigma})_\sigma \frac{\Delta\sigma}{2})\frac{dx}{C}, \tag{9.4}$$

$$x_t = x - \Delta x/2 + (C(\sigma) - (\frac{\partial C}{\partial \sigma})_\sigma \frac{\Delta\sigma}{2})\frac{dx}{C}. \tag{9.5}$$

When the wave is centered at $x + dx$, the thickness of the layer is

$$\Delta x(x + dx) = x_l - x_t = \Delta x(x) + (\frac{\partial C}{\partial \sigma})_\sigma \Delta\sigma \frac{dx}{C}. \tag{9.6}$$

Then,

$$\frac{d\Delta x}{dx} \approx \frac{\Delta x(x + dx) - \Delta x(x)}{dx} = (\frac{\partial C}{\partial \sigma})_\sigma \frac{\Delta\sigma}{C}. \tag{9.7}$$

For a spherical shock wave, energy conservation requires

$$x^2 \Delta x u^2 = \text{constant}, \tag{9.8}$$

where $u$ is particle velocity at the center of the layer. After differentiating Eq. (9.8) with respect to $x$, we have

$$\frac{du}{dx} = -\frac{u}{x}(1 + \frac{x}{2\Delta x}\frac{d\Delta x}{dx}). \tag{9.9}$$

Substituting Eq. (9.7) into Eq. (9.9) yields particle velocity decay rate as:

$$\frac{du}{dx} = -\frac{u}{x}(1 + K_d x), \tag{9.10}$$

where

$$K_d = \frac{1}{2\Delta x}(\frac{\partial C}{\partial \sigma})_\sigma \frac{\Delta \sigma}{C}. \tag{9.11}$$

In general, $K_d$ is a function of $C$, $x$ and $u$. Therefore, particle velocity decay rate depends on wave propagation history.

For a very short propagation distance from $x$ to $x_1$, $K_d$ can be approximated to be a constant. Then, integration of Eq. (9.10) gives

$$\frac{u(x_1)}{u(x)} = \frac{x}{x_1} d_r, \tag{9.12}$$

where

$$d_r = \exp(-K_d(x_1 - x)). \tag{9.13}$$

For a supported nonlinear elastic wave, $\Delta\sigma < 0$. When $\partial C/\partial\sigma > 0$

$$K_d \ < \ 0,$$

$$\frac{d\Delta x}{dx} < 0. \tag{9.14}$$

When $\partial C/\partial\sigma < 0$,

$$\begin{aligned} K_d &> 0, \\ \frac{d\Delta x}{dx} &> 0. \end{aligned} \tag{9.15}$$

Eqs. (9.14) and (9.15) indicate that (1) for a material with $\partial C/\partial\sigma > 0$, a nonlinear elastic wave decays less rapidly than that of a linear elastic wave by a ratio of $d_r$ (Eq. (9.13)) and the wave width decreases with propagation distance, and (2) for a material with $\partial C/\partial\sigma < 0$, elastic wave decays more rapidly than that of a linear elastic wave by a ratio of $d_r$ and the width increases with propagation distance.

For a non-supported nonlinear elastic wave, $\Delta\sigma > 0$ when $\partial C/\partial\sigma > 0$, and $\Delta\sigma < 0$ when $\partial C/\partial\sigma < 0$. When $\partial C/\partial\sigma > 0$,

$$\begin{aligned} K_d &> 0, \\ \frac{d\Delta x}{dx} &> 0. \end{aligned} \tag{9.16}$$

When $\partial C/\partial\sigma < 0$,

$$\begin{aligned} K_d &> 0, \\ \frac{d\Delta x}{dx} &> 0. \end{aligned} \tag{9.17}$$

Eqs. (9.16) and (9.17) show that for a material with $\partial C/\partial\sigma > 0$ or $\partial C/\partial\sigma < 0$ ,

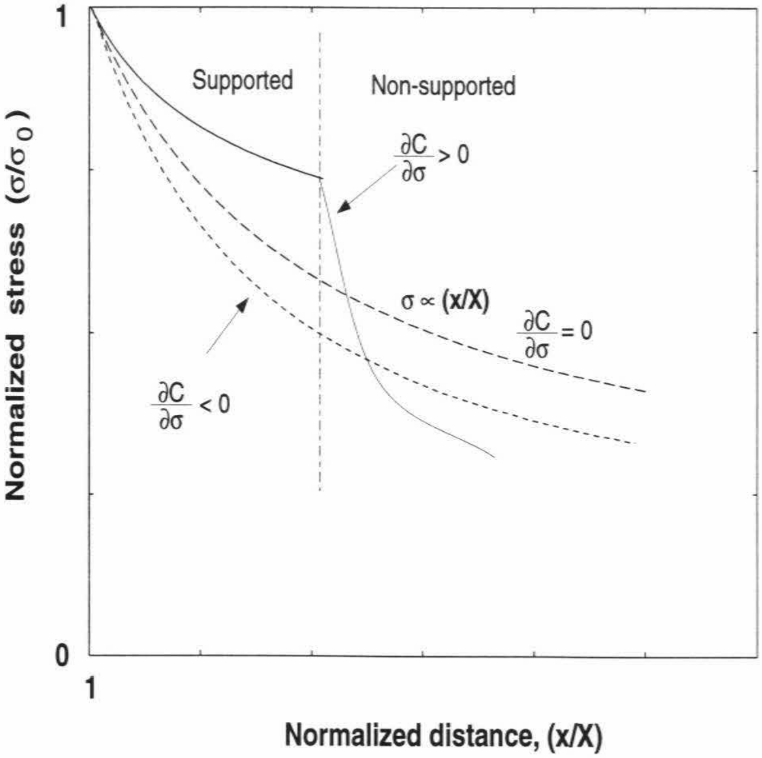

Figure 9.4: Spherical elastic shock amplitude normalized by impact pressure at impact surface versus propagation distance normalized by spherical impactor radius.

elastic wave decay is more rapid than that of a linear elastic wave by a ratio of $d_r$ and the wave width increases with propagation distance. Figure 9.4 schematics relative decay rate of elastic wave stress amplitude under three different conditions.

When peak stress is below elastic limit, the relation between stress and specific volume under impact and hydrostatic loading conditions is shown in Figure 9.2 for vitreous $GeO_2$ (this work and *Smith et al.* [1995]) and Figure 9.5 for fused $SiO_2$ (*Wackerle* [1962]). Figure 9.5 indicates that the compressibility of fused $SiO_2$ in the elastic deformation regime decreases with increasing stress under both uniaxial strain shock loading and hydrostatic loading, i.e., $\partial C/\partial \sigma > 0$ when stress is higher than 4 GPa. Therefore, on the basis of Eq. (9.12), the decay of a supported elastic wave is expected to occur less rapidly than that of a linear elastic wave. The present experimental data (Eq. (8.6)) support this conclusion. For vitreous $GeO_2$, Figure 9.2 indicates that the compressibility increases in elastic regime under both shock and

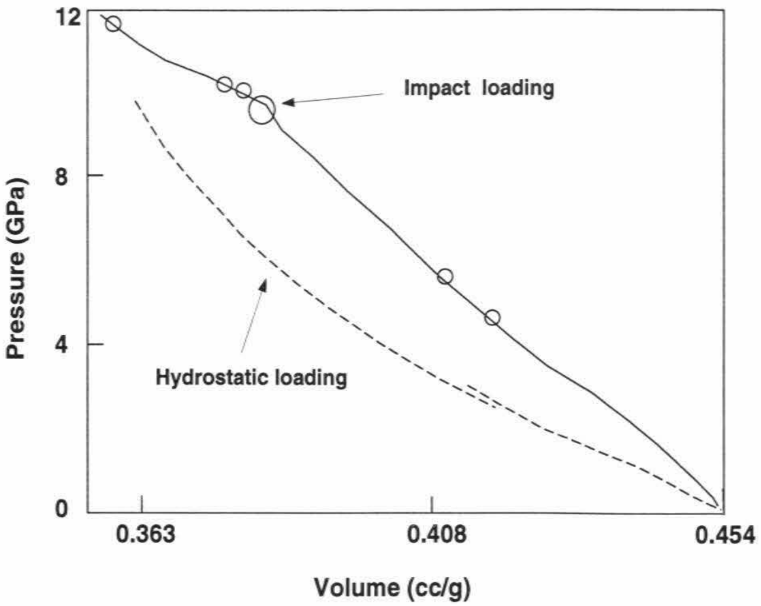

Figure 9.5: Pressure versus volume of fused $SiO_2$ from *Wackerle* [1962].

hydrostatic loading, i.e., $\partial C/\partial \sigma < 0$. Therefore, the supported elastic wave must decay faster than a linear elastic wave based on Eq. (9.12). The present data (Eq. (8.7)) agree with this prediction.

### 9.3.2 Spherical shock wave decay

For a spherical shock wave, the same derivation in the above section can be followed. The particle velocity of a spherical shock wave decays according to

$$\frac{u(x_1)}{u(x)} = \frac{x}{x_1}\exp(-K_p(x_1 - x)), \tag{9.18}$$

where

$$K_p = \frac{1}{2\Delta x}(\frac{\partial D}{\partial p})_p\frac{\Delta p}{D}, \tag{9.19}$$

where $\Delta p$ is the pressure difference at the leading and tailing edges of a shock wave layer. Because $\partial D/\partial p > 0$ is the necessary condition for forming shock waves, $K_d < 0$

for supported shock waves ($\Delta p < 0$) and $K_d > 0$ for non-supported shock waves ($\Delta p > 0$). Therefore, a supported shock wave decays less rapidly than a linear elastic wave, and a non-supported shock wave decays more rapidly than a linear elastic wave. The slow decay rate of the supported shock wave results from the energy transfer between the tailing and leading edges. From both experimental and numerical calculations, it is found that the spherical shock wave decays very slowly near the impact site (*Ahrens and O'Keefe* [1977]). The slow decay is expected to be largely the result of the slow geometric spreading (*Ahrens and O'Keefe* [1977]. However, the above discussion suggests that a contribution to the slow decay results from energy exchange between the wave front and wave tail.

The above discussion only considers the decay due to geometry and supported conditions. In general, shock wave decay is controlled by several processes, such as, geometric effect, release wave, phase transformation, plastic deformation and interaction between shock and elastic waves (*Ahrens and O'Keefe* [1977]). In vitreous $GeO_2$, *Chen et al.* [1998] found that spherical wave decay follows $P \sim x^\alpha$ where $\alpha$ is -1.15 when pressure is below 8 GPa and -2.72 when pressure is higher than 8 GPa using numerical simulation. The larger $\alpha$ is believed to be due to irreversible phase transitions in $GeO_2$ when pressure is over 8 GPa. The shock wave decay shown in Figure 8.8 results from four major processes that are (1) geometrical spreading, (2) release wave taking-over, (3) phase transition and (4) the transformation of shock wave energy to precursor energy. Therefore, the decay rate of a spherical shock wave in vitreous $GeO_2$ under present experimental conditions should change dramatically with peak pressure or propagation distance as labeled by Stages A, B, C, and D in Figure 8.6. During Stage A, because the shock wave is supported, the shock wave decays slowly. During Stage B, the release wave starts to take over shock wave. Because of the phase transition, the release wave velocity depends on both the percentage of the high density phase and the reversibility of the phase transition under release (*Chen et al.* [1998]), shock wave decay rate changes dramatically in the pressure range of 6 to 14 GPa. During Stage C, the shock wave decay rate changes again due to the ramp-wave structure in this pressure range of 4 to 6 GPa. During Stage D, the shock wave disappears.

Based on the discussion above, the shock wave decay rate cannot be explained simply using $P \sim x^{-\alpha}$ when a material is under a phase transition and the shock wave pressure is in the range of the phase transition. The details of shock wave decay should be based on phase transition dynamics under loading and releasing. Whenever how $\alpha$ changes, the experimental data show that phase transition has a significant effect on spherical shock wave decay in vitreous $GeO_2$ based on the limit data as given in Eq. (8.8).

# Chapter 10 Conclusions

Based on the stress wave profile measurement in vitreous $GeO_2$, we conclude

1. An elastic precursor has an amplitude of 4 GPa and a particle velocity of 333 m/s. The wave velocity decreases from the initial longitudinal velocity of 3.5 km/s at atmospheric pressure to the bulk wave velocity of $\sim$ 2.9 km at $\sim$ 4 GPa.

2. A ramp wave follows the elastic precursor with an amplitude $\sim$ 2 GPa. Within this pressure interval, compressibility increases significantly. The wave velocity drops to $\sim$ 2.3 km/s at $\sim$ 6 GPa. It is possible that partial melting and/or fracture and/or new phase formation may be occurring in this period.

3. A normal shock wave forms when the peak shock stress is higher than 6 GPa. Based on present data and the data of *Jackson and Ahrens* [1979], the Hugoniot relation of vitreous $GeO_2$ is

   $$D = 0.917 + 1.711u, \quad \text{for } u > 0.6 \text{ km/s}, \tag{10.1}$$

   where $D$ and $u$ are in km/s.

4. When shock stress is higher than $\sim$ 15 GPa, vitreous $GeO_2$ compression data closely match that of rutile $GeO_2$ (*Jackson and Ahrens* [1979]). Therefore, the phase change from 4-fold to 6-fold $GeO_2$ starts at about $\sim$ 4 GPa and completes at $\sim$ 15 GPa.

5. A similarity between the pressure-volume relations for fused $SiO_2$ and $GeO_2$ appears when the ratio of $SiO_2$ to $GeO_2$ density is used to scale down shock stress in $SiO_2$.

6. Comparison of wave profiles of fused $SiO_2$, vitreous $GeO_2$ and soda-lime glass shows that ramp precursor in the three materials has approximately same amplitude ($\sim$ 4 GPa) and particle velocity ($\sim$ 330 m/s). The only difference in the response to shock loading between fused $SiO_2$ and $GeO_2$ is that a well-defined elastic wave exists in $SiO_2$ but not in vitreous $GeO_2$.

7. Spherical impact results show that a supported spherical elastic wave in fused $SiO_2$ decays less rapidly than that of a linear elastic wave when the elastic wave amplitude is higher than 4 GPa, and a supported spherical elastic wave in vitreous $GeO_2$ decays more rapidly than that of a linear elastic wave.

8. Based on a simple analysis of elastic wave propagation, it is found that the different decay rate of a spherical elastic wave in fused $SiO_2$ and vitreous $GeO_2$ results from the compressibility variation with stress in these materials.

9. The energy exchange among supported shock waves may contribute to the very slow decay near the impact site as observed and calculated (*Ahrens and O'Keefe* [1977]). The experimental data indicate that the phase transition in $GeO_2$ has a major effect on spherical shock wave decays as predicted by *Chen et al.* [1998].

# Bibliography

Ahrens, T. J., Equation of State, *High-Pressure Shock Compression of Solids,* edited by J. R. Asay and M. Shahinpoor, published by Springer-Verlag, New York, 75-110, 1992.

Ahrens, T. J. and J. D. O'Keefe, Equation of state and impact-induced shock wave attenuation on the moon, *Impact and Explosion Cratering,* edited by D. J. Roddy, R. O. Pepin and R. B. Merrill, Pergamon Press, New York, 639-656, 1977.

Anan'in, A. V., O. N. Breusov, A. N. Dremin, S. V. Pershin, and V. F. Tatsii, The effect of shock waves on silicon dioxide, I. Quartz, *Combust. Explos. Shock Waves,* 10, 372-379, 1974

Barker, L. M. and R. E. Hollenbach, Shock-wave studies of PMMA, fused silica and sapphire, *J. Appl. Phys.*, 41, 4208-4226, 1970.

Boslough M. B. and J. R. Asay, Basic principles of shock compression , *High Pressure Shock Compression of Solids*, edited by J. R. Asay and M. Shahinpoor, published by Springer-Verlag, New York, 7-39, 1992.

Bourne, N. K. and Z. Rosenberg, The dynamic response of soda-lime glass, *Shock Compression of Condensed Matter-1995,* edited by S. C. Schmidt and D. Tao, published by AIP Press, New York, 567-573, 1996.

Bourne, N. K., Z. Rosenberg and A. Ginsberg, The ramping of shock waves in three glasses, (unpublished).

Bourne, N. K. and Z. Rosenberg, On the ringing observed in shock-loading piezoresistance stress gauges, *Meas. Sci. Technol.*, 8, 570-573, 1997.

Chen, G. Q., T. J. Ahrens, W. Yang and J. K. Knowles, Effect of irreversible phase change on shock-wave propagation, (unpublished).

Durben, D. J. and G. H. Wolf, High pressure Raman spectroscopic study of vitreous $GeO_2$, *Phys. Rev. B.*, 43, 2355-2363, 1991.

Fowles, R. and R. F. Williams, Plane stress wave propagation in solids, *J. Appl. Phys.*, 37, 360-363, 1970.

Grady, D. E, Shock deformation of brittle solids, *J. Geophys. Res.,* 85, 913-924, 1980.

Grady, D. E, Dynamic properties of ceramic materials, SAND94-3266, 1995.

Grady, D. E, Shock wave compression of brittle solids, *Mechanics of Materials*, 29, 181-203, 1998.

Itie, J. P., A. Polian, G. Calas, J. Petiau, A. Fontaine and H. Tolentino, Pressure-induced coordinate changes in crystalline and vitreous $GeO_2$, *Phys. Rev. Lett.,* 63, 398-402, 1989.

Itie, J. P., A. Polian, G. Calas, J. Petiau, A. Fontaine and H. Tolentino, Coordinate changes in crystalline and vitreous $GeO_2$, *High Pres. Res.* 5, 717-719, 1990.

Jackson, I. and T. J. Ahrens, Shock-wave compression of vitreous and rutile-type $GeO_2$: a comparative study, *Physics of the Earth and Planetary Interiors,* 20, 60-70, 1979.

Kondo K., A. Lio and A. Sawaoka, Nonlinear pressure dependence of the elastic moduli of fused quartz up to 3.5 GPa, *J. Appl. Phys.*, 52, 2826-2831, 1981.

Madon, M., P. Gillet, C. Julien and G. D. Price, A vibrational study of phase transitions among the $GeO_2$ polymorph, *Phys. and Chem. of Minerals,* 18, 7-18, 1991.

Mackenzie, J. D., High pressure effects on oxide glasses: Densification in rigid states, *Journal of the American Ceramic Society,* 46, 461-468, 1963.

Marsh, S. P., *LASL Shock Hugoniot Data*, published by University of California Press, Berkeley, 321-324, 1980.

McQueen, R. G., Shock waves in condensed media: their properties and the equation of state of materials derived from them, *High-Pressure Equation of State: Theory and Applications,* edited by S. Eliezer and R. A. Ricci, published by North-Holland, New York, 101-213, 1989.

Meyers, M. A., *Dynamic Behavior of Materials*, John Wiley and Sons, Inc., New York, 126-130, 1994.

Robertson, P. B. and R. A. F. Grieve, Shock attenuation at terrestrial impact structures, *Impact and Explosion Cratering*, edited by D. J. Roddy, R. O. Pepin and R. B. Merrill, published by Pergamon Press, New York, 687-702, 1977.

Rosenberg, Z., D. Yaziv and Y. Partom, Calibration of foil-like manganin gauges in planar shock wave experiments, *J. Appl. Phys.*, 51, 3702-3705, 1980.

Scholze, H. *Glass*, published by Speringer-Verlag, New York, 1991.

Smith, K., E. Shero, A. Chizmeshya,G. Wolf, The equation of state of polymorphic Germania glass: A two-domain description of the viscoelastic response, *J. Chem. Phys.*, 102, 6851-6857,1995.

Stolper, E. M. and T. J. Ahrens, On the nature of pressure-induced coordination changes in silicate melts and glasses, *Geophys. Res. Lett.,* 14, 1231-1233, 1987.

Sugiura, H., K. Kondon and A. Sawaoka, Dynamic response of fused quartz in the permanent densification region, *J. Appl. Phys.*, 52, 3375-3382, 1980.

Sundaram, S., Pressure-shear plate impact studies of alumina ceramics and the influence of an intergranular glassy phase, PH.D. Thesis, Brown University, 1998.

Suito, K., M. Miyoshi, T. Sasakura, and H. Fujisawa, Elastic properties of obsidian, vitreous $SiO_2$, and vitreous $GeO_2$ under high pressure up to 6 GPa, *High-Pressure*

*Research: Application to Earth and Planetary Sciences*, edited by Y. Syono and M. Manghnani, Terra Scientific Publishing Company, Tokyo, 219-225, 1992.

Tsuchiya, T., T. Yamanaka, and M. Matsui, Molecular dynamics study of the crystal structure and phase relation of the $GeO_2$ polymorph, *Phys. Chem. Minerals*, 25, 94-100, 1998.

Wackerle, J., Shock-wave compression of quartz, *J. Appl, Phys.,* 33, 922-937, 1962.

Wolf, G. H., S. Wang, C. Herbest, D. Durben, W. Oliver, Z. Kang and K. Halvorson, Pressure induced collapse of the tetrahedral framework in crystalline and amorphous $GeO_2$, *High-Pressure Research: Application to Earth and Planetary Science,* edited by Y. Syono and M. H. Manghnani, published by Terra Scientific Publishing Company, Tokyo, 503-517, 1992.

## Publications

1. Liu, C. and T. J. Ahrens, Stress wave attenuation in shock-damaged rock, *J. Geophys. Res.*, 1997:

   The velocity and attenuation of ultrasonic stress waves in gabbroic rock samples (San Marcos, California) subjected to shock loading in the 2 GPa range were studied. From $P$ wave velocity measurements we determined the damage parameter $D_p$ and crack density $\varepsilon$ of the samples and related these to the attenuation coefficient (quality factor) under dynamic strains of $2 \times 10^{-7}$ and at a frequency of 2 MHz using the ultrasonic pulse-echo method. A fit to the data yields the $P$ wave spatial attenuation coefficient at a frequency of 2 MHz, $\alpha_p(D_p) = 1.1 + 28.2D_p$ (decibels per centimeter). From the relation between the attenuation coefficient and quality factor, the quality factor $Q$ is given by $Q^{-1} = 0.011(1 + 25.6D_p)(1 - D_p)^{1/2}$. Using O'Connell-Budiansky theory relating crack density to velocity, the parameter in Walsh's theory was determined based on experimental data. An approximate method is also proposed to estimate the average half-length of cracks based on the attenuation measurements.

2. Anderson, W., C. Liu and T. J. Ahrens, Shock wave equation of state and shock wave decay in shale, submitted to *J. Geophys. Res.*, 1997.

3. Liu, C. and T. J. Ahrens, Wave generation from confined explosions in rocks, submitted to *Pure and Applied Geophysics*, 1999.

4. Zhuang, S., C. Liu, C. Wang and C. Sun, Dynamic fracture of aluminum at ultra-high strain-rate $10^7$/s, *J. Materials Science Letter,* 13, 1740-1741, 1994.

5. Chenwei Sun, Shiming Zhang, Yanping Wang and Cangli Liu, Dynamic fracture in metals at high strain rate, *High Pressure Physics of Materials*, edited by Lee Davison, G.E. Grady and M. Shahinpoor, published by Springer, New York, 72-89, 1996.